Chemical Science

ROYAL SOCIETY OF CHEMISTRY

REVIEW

View Article Online
View Journal | View Issue

Cite this: *Chem. Sci.*, 2024, **15**, 7441

Insights into the cycling stability of manganese-based zinc-ion batteries: from energy storage mechanisms to capacity fluctuation and optimization strategies

Yanxin Liao,[a] Chun Yang,[bc] Jie Bai,[a] Qingqing He,[a] Huayu Wang,[a] Haichao Chen, *[b] Qichun Zhang *[d] and Lingyun Chen *[a]

Manganese-based materials are considered as one of the most promising cathodes in zinc-ion batteries (ZIBs) for large-scale energy storage applications owing to their cost-effectiveness, natural availability, low toxicity, multivalent states, high operation voltage, and satisfactory capacity. However, their intricate energy storage mechanisms coupled with unsatisfactory cycling stability hinder their commercial applications. Previous reviews have primarily focused on optimization strategies for achieving high capacity and fast reaction kinetics, while overlooking capacity fluctuation and lacking a systematic discussion on strategies to enhance the cycling stability of these materials. Thus, in this review, the energy storage mechanisms of manganese-based ZIBs with different structures are systematically elucidated and summarized. Next, the capacity fluctuation in manganese-based ZIBs, including capacity activation, degradation, and dynamic evolution in the whole cycle calendar are comprehensively analyzed. Finally, the constructive optimization strategies based on the reaction chemistry of one-electron and two-electron transfers for achieving durable cycling performance in manganese-based ZIBs are proposed.

Received 22nd January 2024
Accepted 18th March 2024

DOI: 10.1039/d4sc00510d

rsc.li/chemical-science

1 Introduction

The rapidly increasing energy consumption and environmental issues make it urgent to utilize large-scale electrical energy storage (EES) systems to store intermittent but renewable energy, such as solar energy, wind, and tidal energy.[1–3] Among the various EES systems, lithium-ion batteries (LIBs) have been widely used for dozens of years owing to their high gravimetric energy density and excellent cycling performance.[4,5] However, the high price of lithium and its limited resources coupled with safety and environmental concerns for the use of flammable organic electrolytes hinder the application of LIBs as large-scale EES systems.[6,7]

Fortunately, the emerging aqueous rechargeable batteries, particularly aqueous zinc-ion batteries (ZIBs) hold great promise for large-scale EES because of the low cost, natural abundance, high stability, low electrochemical potential (−0.763 V *vs.* the NHE) and high theoretical capacity (5855 mA h cm^{-3} and 820 mA h g^{-1}) of Zn metal coupled with the high safety and high ionic conductivity of aqueous electrolytes.[8–12] In general, the energy storage performance of ZIBs is mainly related to the cathode material, Zn anode, electrolyte, and separator.[13] Recently, although studies in the literature have focused on the issues associated with the Zn anode,[14–17] the nature of cathode materials essentially dominates the electrochemical performance of ZIBs, such as capacity, working potential, cycling stability, and rate performance. However, owing to the much larger radius of hydrated Zn^{2+} (4.3 Å) than Li^{+} (0.76 Å), many cathode materials with excellent electrochemical performance in LIBs are not suitable for ZIBs.[18] Consequently, the limited performance of cathode materials for ZIBs greatly impede the development of high-performance EES systems. Thus far, manganese-based materials,[19,20] vanadium-based materials,[21–23] Prussian blue and its analogues,[24–26] Chevrel phase compounds,[27,28] and organic compounds have been exploited as cathode materials for ZIBs.[29,30] Amongst them, manganese-based materials are considered the most attractive cathodes for ZIBs and have been widely and intensively investigated owing to their low cost, natural abundance, low toxicity,

[a]*Department of Applied Chemistry, School of Chemistry and Chemical Engineering, Chongqing University, Chongqing 401331, China. E-mail: lychen@cqu.edu.cn*
[b]*Institute of Materials for Energy and Environment, School of Materials Science and Engineering, Qingdao University, Qingdao 266071, China. E-mail: chenhc@qdu.edu.cn*
[c]*Department of Applied Biology and Chemical Technology, The Hong Kong Polytechnic University, Hong Kong SAR 999077, China*
[d]*Department Materials Science and Engineering, Department of Chemistry, Center of Super-Diamond and Advanced Films (COSDAF), City University of Hong Kong, Kowloon, Hong Kong SAR 999077, China. E-mail: qiczhang@cityu.edu.hk*

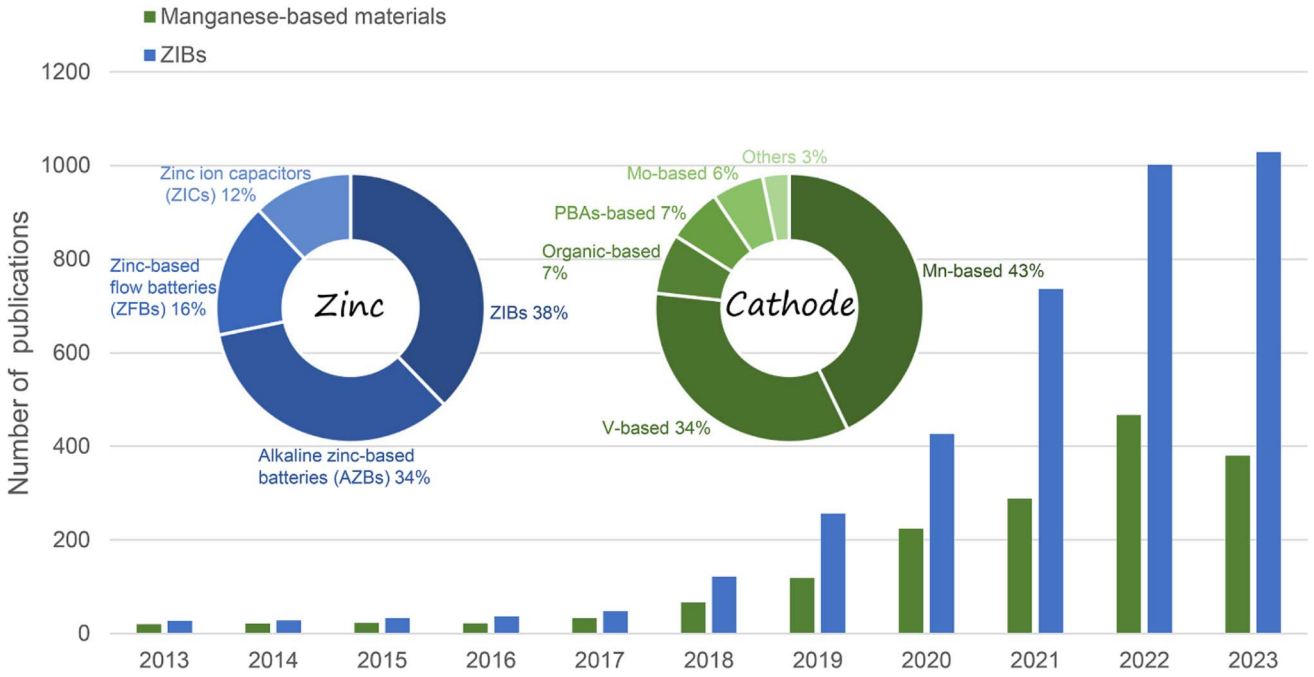

Fig. 1 Number of publications in recent years on manganese-based ZIBs and ZIBs (data from Web of Science, December 2023).

multivalent states, high operation voltage, and satisfactory capacity (Fig. 1).[31–33]

Significant progress has been made in manganese-based ZIBs over the past decade, as depicted in Fig. 2. Nevertheless, manganese-based cathodes in ZIBs involve various and controversial energy storage mechanisms, and six major energy storage mechanisms have been successively discovered in the past ten years: (1) Zn^{2+} insertion/extraction, (2) H^+ insertion/extraction, (3) H^+ and Zn^{2+} co-insertion/extraction, (4) chemical conversion, (5) dissolution–deposition, and (6) hybrid storage mechanisms (Fig. 3). These complex mechanisms invariably confuse readers, particularly for recent students in this field, and thus need to be comprehensively and clearly summarized. Moreover, the unsatisfactory long-term cycling stability (particularly at a low current) of manganese-based ZIBs has severely hampered their practical application. Meanwhile, a fluctuating capacity has been common observed (including capacity activation process and capacity degradation process) during long-term cycling and its mechanism has not been clearly understood, leading to a lack of robust methods to improve their cycling stability. Although some good reviews have been published on manganese-based ZIBs to guide

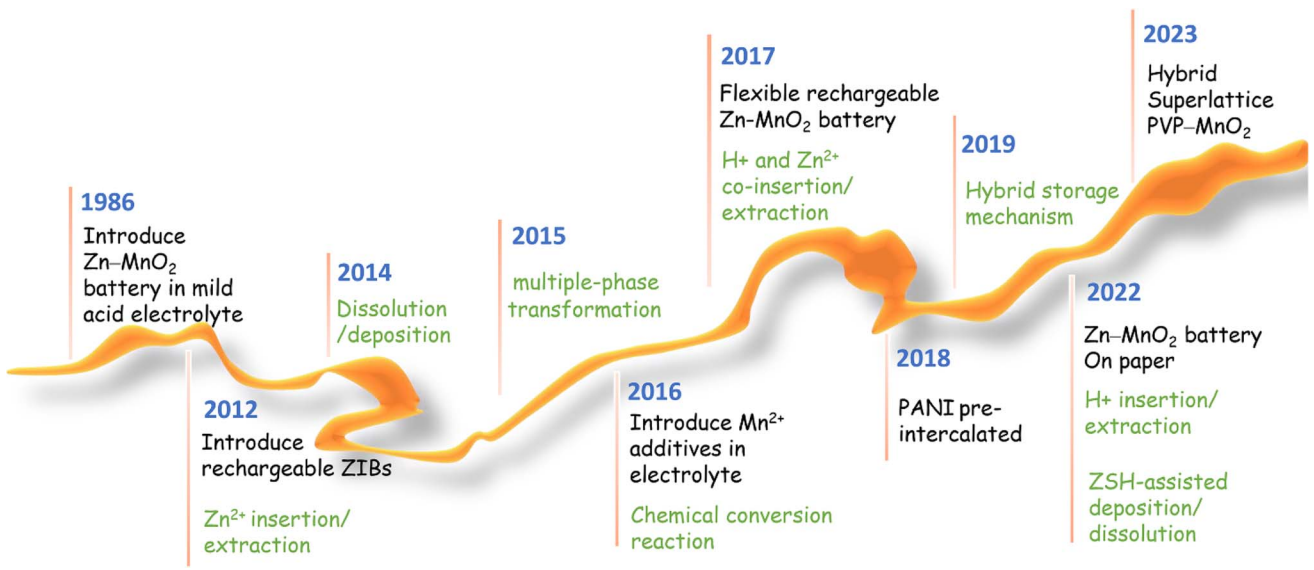

Fig. 2 Progress on manganese-based ZIBs.

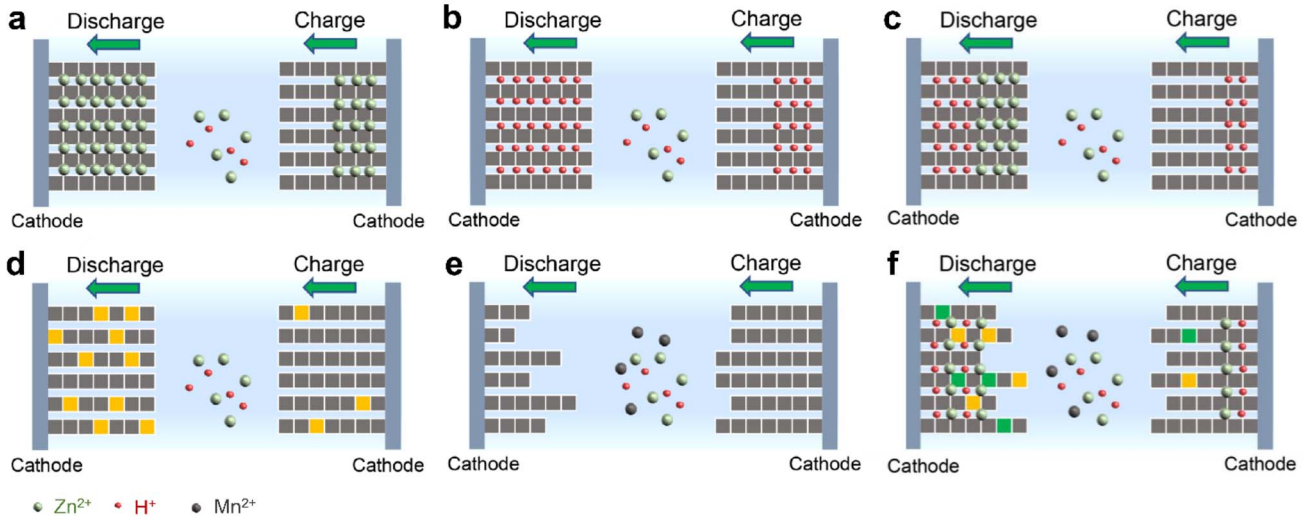

Fig. 3 Illustration of energy storage mechanisms for manganese-based ZIBs. (a) Zn^{2+} insertion/extraction, (b) H^+ insertion/extraction, (c) H^+ and Zn^{2+} co-insertion/extraction, (d) chemical conversion reaction, (e) dissolution–deposition, and (f) hybrid storage mechanism.

researchers,[34–43] these reviews mainly focused on optimization strategies for high capacity and fast reaction kinetics, seldomly mentioning the dynamic fluctuation of capacity and lacking a deep comprehension of essential reasons for capacity activation and degradation. Consequently, a comprehensive understanding of the capacity fluctuation is urgently needed to guide researchers to design manganese-based ZIBs with stable cycling performances.

In this review, the energy storage mechanisms of manganese-based ZIBs with different structures are systematically clarified and summarized. More importantly, the capacity fluctuation of manganese-based ZIBs is comprehensively analyzed for the first time. We not only summarize the immediate causes of capacity activation and degradation, but also analyze the inherent dynamic evolutions (such as pH, reaction mechanisms, and active materials) that result in capacity fluctuations. Furthermore, the constructive optimization strategies based on the reaction chemistry of one-electron and two-electron transfer for achieving durable cycling performance manganese-based ZIBs are proposed, respectively. Finally, the conclusions and outlooks on the present reaction mechanisms and optimization strategies for achieving durable cycling performances based on our personal perspectives are also provided. This review provides a comprehensive overview and the research directions focusing on the recent reaction chemistry and cycling stability, which will provide a guide for future studies on manganese-based ZIBs.

2 Crystal structure of manganese-based materials

In this review, we divide manganese-based materials into four categories, including MnO_2 polymorphs, low-valence manganese oxides, metal manganate (AMn_xO_y, A = Li, Na, Zn, Mg, Ca, *etc.*) and other manganese-based compounds. Various atomic structures and chemical constituents result in a variety of multivalent phases (+2, +3, +4, +5, and +7) and crystal structures for manganese-based materials (Fig. 4). The crystal structures of manganese-based materials are closely related to the energy storage performance of the corresponding ZIBs and dominate the reaction chemistry of cathodes. Therefore, it is essential to first comprehend the crystal structures of manganese-based materials.

2.1 MnO_2 polymorphs

MnO_2 is one of the most popular cathodes for ZIBs, which possesses a high theoretical capacity of 308 mA h g^{-1} or 616 mA h g^{-1} based on one-electron or two-electron transfer, respectively. Impressively, MnO_2 has diverse polymorphs with distinct tunneled or layered structures composed of basic octahedral units (MnO_6) connected in different ways. These diverse polymorphs can be summarized based on their tunnel size, as shown in Fig. 4. ε-MnO_2 (akhtenskite) is a special polymorph, which is densely packed without any tunnel structure. Its dense packing structure is not conducive to rapid cation insertion/extraction, resulting in low electrochemical activity for ZIBs.[44] Regulating structures such as introducing defects is an efficient strategy to increase the number of active sites to improve the electrochemical performance of ε-MnO_2.[45] λ-MnO_2 (spinel) possesses a three-dimensional (3D) spinel structure with [1 × 1] tunnels, which is a metastable form of MnO_2 and can be easily obtained through acid treatment of $LiMn_2O_4$ at ambient temperature.[46] It has been reported that λ-MnO_2 only can deliver a poor capacity of 33.8 mA h g^{-1},[47] showing the lowest electrochemical activity among the MnO_2 polymorphs. Its unsatisfactory capacity may result from its limited number of 3D tunnels, restricting the migration of Zn^{2+}.[48] β-MnO_2 (pyrolusite) is one of the most thermodynamically stable structure, which also has narrow [1 × 1] tunnels. However, the numerous open channels of β-MnO_2 can

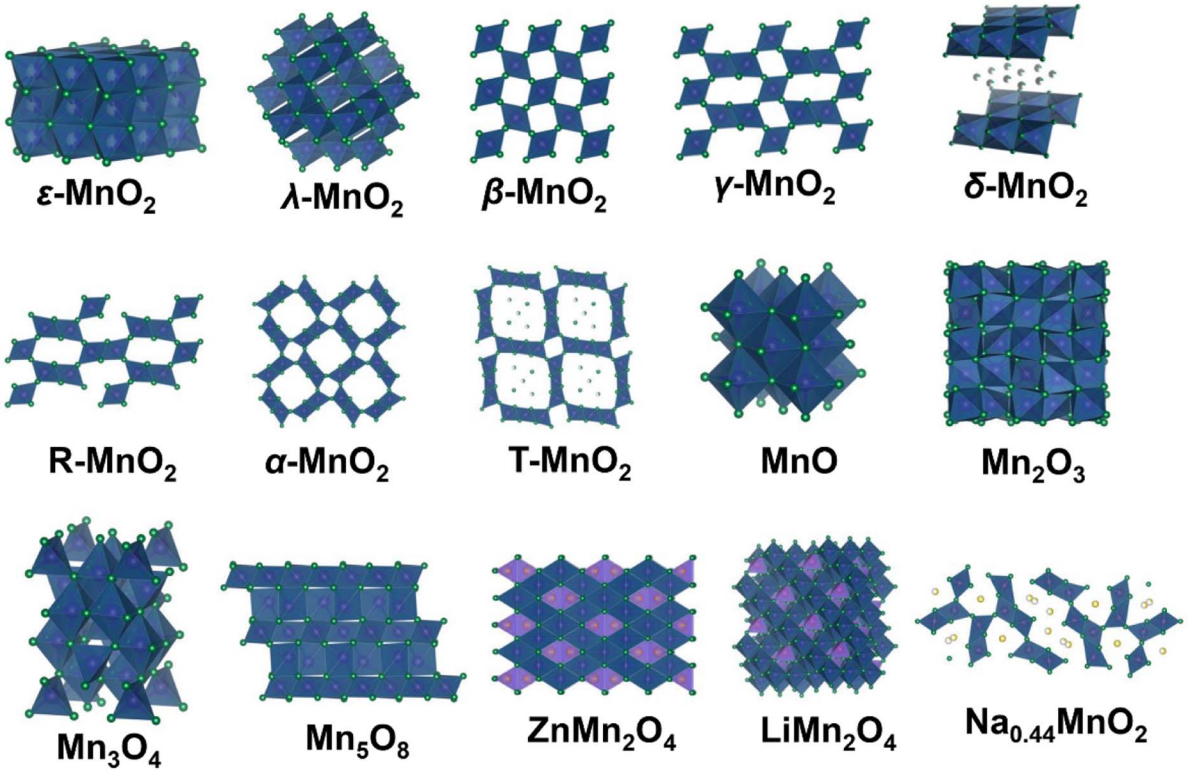

Fig. 4 Structural drawings of various manganese-based materials.

accommodate more cation insertion/extraction than λ-MnO_2. Recent studies have demonstrated the excellent electrochemical performance of β-MnO_2,[49–52] for example, Chen *et al.*[53] reported that β-MnO_2 can deliver a remarkable reversible capacity of 225 mA h g^{-1} and outstanding long-term cycling stability with 94% capacity retention over 2000 cycles. γ-MnO_2 (nsutite) possesses a hybrid tunnel structure with [1 × 1] and [1 × 2] tunnels, which has been successfully applied in alkaline Zn–MnO_2 batteries and is also promising in ZIBs.[54,55] δ-MnO_2 (birnessite) features a typical two-dimensional (2D) layered structure with a wide interlayer spacing of 7.0 Å, which is favorable for cation intercalation/extraction. In addition, the layered structure of δ-MnO_2 originating from its source avoids a phase transition from tunneled MnO_2 to a layered phase, which greatly reduces severe volume changes. Notably, the interlayer space of δ-MnO_2 usually contains many cations (such as K^+ and Na^+) and structural water, which are beneficial to stabilize the MnO_6 layers. R-MnO_2 (ramsdellite) has a moderate tunnel size of [1 × 2] and is larger than β-MnO_2 but narrower than α-MnO_2, which can be regarded as a part of γ-MnO_2. Chen *et al.*[56] found that R-MnO_2 uniquely shows a low manganese dissolution property compared to other MnO_2 polymorphs due to the thermodynamic feasibility and moderate volume changes of its [1 × 2] tunnels. α-MnO_2 (hollandite) possesses large [2 × 2] tunnels, which is considered an ideal material for cation intercalation/extraction. To date, α-MnO_2 exhibits one of the most comprehensive electrochemical performances among manganese-based materials and has been extensively studied by researchers.[38,44] T-MnO_2 (todorokite) has large [3 × 3] tunnels with many intercalated metal cations and water molecules, and these guest species can effectively stabilize the tunnel framework and prevent structural collapse. However, although T-MnO_2 possesses a much larger tunnel structure than α-MnO_2, its practical capacity is much lower than α-MnO_2, which can be ascribed to the pre-intercalation of too many metal cations and water molecules, reducing the number of potential Zn^{2+} insertion sites.[57]

2.2 Low-valence manganese oxides

Low-valence manganese oxides, including MnO, Mn_2O_3, Mn_3O_4 and Mn_5O_8, are also important cathode materials for ZIBs. In the case of MnO, with Mn^{2+} ions possessing a coordination number of six, it displays tetrahedral or octahedral coordination, together with specific magnetic anisotropy.[58] MnO is intrinsically inactive without any tunnels for Zn^{2+} and H^+ insertion/extraction. However, it exhibits an excellent electrochemical performance comparable to MnO_2 after the initial activation cycles,[59,60] and its activation mechanisms will be discussed in detail in Section **4.2.** In the structure of Mn_2O_3, the Mn^{3+} ions are arranged in an octahedral coordination with each O ion surrounded by four Mn ions. Similar to MnO, it lacks migration channels, and thus it has been found that pristine Mn_2O_3 can only deliver a limited capacity of 78 mA h g^{-1} in the first discharge.[61] In the case of spinel Mn_3O_4 (chemical formula of $Mn^{2+}Mn_2{}^{3+}O_4$), Mn^{2+} and Mn^{3+} occupy the tetrahedral (4a) and octahedral (8d) sites in the intermediate distorted cubic close-pack array of oxygen anions (16h), respectively. Mn_3O_4

demonstrates thermodynamic stability, making it typically irreversible as the final discharge product.[43] Mn_5O_8 (chemical formula of $Mn_2^{2+}Mn_3^{4+}O_8$) is another layered structure manganese oxide composed of 2D octahedral sheets of $[Mn_3^{4+}O_8]$ with Mn^{2+} located above and below the vacant Mn^{4+} sites.[62] The large interlayer space of Mn_5O_8 offers abundant active sites and allows facile ion diffusion, and it has been reported that Mn_5O_8/rGO can deliver a high reversible capacity of 260 mA h g^{-1} at 100 mA g^{-1} with a stable cycling performance over 1000 cycles.[63] However, there are few reports on the application of Mn_5O_8 as a cathode material for ZIBs, and thus more efforts should be devoted to the study of Mn_5O_8.

2.3 Metal manganate AMn_xO_y

Metal manganate AMn_xO_y (A refers to Zn, Li, Na, Mg, *etc.*) can also be utilized as a cathode material for ZIBs, including $ZnMn_2O_4$, $LiMn_2O_4$, $MgMn_2O_4$, $Na_{0.44}MnO_2$, and $CoMn_2O_4$. In the structure of spinel-type $ZnMn_2O_4$, oxygen atoms are arranged in a hexagonal close-packed configuration, forming an octahedral site. In a perfect spinel lacking cation deficiency, the Zn^{2+} ions migrate from one tetrahedral site (4a) to another by passing through an unoccupied octahedral site (8c), encountering significant electrostatic repulsion from the Mn cations in the neighboring octahedral site (8d), thereby strongly impeding Zn^{2+} diffusion.[64] Meanwhile, due to the thermodynamic stability of $ZnMn_2O_4$, which is commonly the final product of manganese-based ZIBs in the capacity attenuation period, the capacity degradation caused by $ZnMn_2O_4$ will be discussed in detail in Section **4.1.3.** Defect engineering is an effective strategy to reduce the electrostatic barrier, leading to easier Zn^{2+} diffusion.[39] The spinel $MgMn_2O_4$ possesses an analogous tetragonal symmetry structure to $ZnMn_2O_4$. Soundharrajan *et al.*[65] fabricated $MgMn_2O_4$ as a cathode with $ZnSO_4$, $MgSO_4$, and $MnSO_4$ as the electrolyte, showing the reversible insertion/extraction of both Mg^{2+} and Zn^{2+}. In the structure of spinel-type $LiMn_2O_4$, the Mn^{3+}/Mn^{4+} ions occupy the octahedral sites (16d) within a cubic close-packed array of oxygen atoms, while the Li^+ ions occupy the tetrahedral sites (8a) and migrate through a three-dimensional channel.[66] $LiMn_2O_4$ has been widely investigated in LIBs due to the inherent advantages of the manganese element and its high specific power.[67] Interestingly, $LiMn_2O_4$ also shows an excellent performance in ZIBs. For instance, Zhang *et al.*[68] reported the fabrication of a Zn/$LiMn_2O_4$ battery containing $ZnSO_4$, Li_2SO_4, and $MnSO_4$ electrolyte, which exhibited a high capacity of more than 300 mA h g^{-1} with long-term cycling stability over 2000 cycles. In addition, tunnel-type $Na_{0.44}MnO_2$ with interconnected 3D S-shaped channels allows facile cation diffusion. Similar to $LiMn_2O_4$ and $MgMn_2O_4$, $Na_{0.44}MnO_2$ demonstrates highly reversible insertion/extraction of Na^+ and Zn^{2+} in hybrid electrolytes composed of $ZnSO_4$ and Na_2SO_4.[69,70]

2.4 Other manganese-based compounds

Compared with crystalline manganese oxides, amorphous manganese oxides with short-range ordered atomic arrangements are ignored in ZIBs due to their lack of a high manganese valency and cation host structure. However, it was demonstrated that amorphous manganese oxides with unique superiority of structural plasticity are beneficial to accommodate the volume changes caused by Zn^{2+}/H^+ intercalation/extraction. In addition, the abundant defects in amorphous manganese oxides can serve as reversible cation storage sites, giving rise to fast ion diffusion kinetics and high specific capacity.[71,72] Besides, MnS,[73] Mn_2SiO_4,[74,75] $LaMnO_3$,[76] MnSe,[77] *etc.* have been developed as available cathode materials for ZIBs. However, most of these cathode materials exhibit unsatisfactory electrochemical performances compared to manganese oxides owing to their intrinsically poor electrochemical activity and structural stability. Therefore, more efforts are needed to improve the inherent shortcomings of these newly developed manganese-based compounds.

In summary, the crystal structure of MnO_2 polymorphs, low-valence manganese oxides, metal manganate, and other manganese-based compounds was discussed. It has been found that the electrochemical performance of these materials in ZIBs is predominantly influenced by their crystal structure. Materials with large tunnel or layered structures generally exhibit superior insertion/extraction capabilities for Zn^{2+}/H^+, whereas those with dense and spinel-type structures, which offer fewer reaction sites for Zn^{2+}/H^+ ions, typically demonstrate inferior electrochemical performances. Table 1 provides a compilation of the previously reported electrochemical performances of manganese-based materials in ZIBs.

3 Energy storage mechanisms

The energy storage mechanisms of manganese-based ZIBs are very complicated and controversial due to the various crystal structures of manganese-based materials and the intricate environment of the aqueous electrolyte in comparison to LIBs with insertion–alloying–conversion reactions.[88] In addition, the reaction of Zn^{2+} deposition to generate large flake-like $Zn_4SO_4(OH)_6\cdot xH_2O$ (ZHS) on the cathode surface during discharge makes the determination of the real reactions more difficult. Undoubtedly, numerous researchers have devoted significant efforts to studying the real reaction mechanisms for a long time. Accordingly, to date, the storage mechanisms of manganese-based ZIBs can be divided into six categories, as presented here.

3.1 Zn^{2+} insertion/extraction mechanism

The Zn^{2+} insertion/extraction mechanism is the earliest accepted mechanism, which was first systematically proven by Kang *et al.*[89] They concluded that the Zn^{2+} from the $ZnSO_4$ or $Zn(NO_3)_2$ aqueous electrolyte can be reversibly intercalated into the tunnels of α-MnO_2, and the anodic zinc can reversibly undergo dissolution/deposition upon discharging and charging (Fig. 5a). The reactions are summarized as below:

$$\text{Cathode: } Zn^{2+} + 2e^- + 2\alpha\text{-}MnO_2 \leftrightarrow ZnMn_2O_4 \quad (1)$$

$$\text{Anode: } Zn \leftrightarrow Zn^{2+} + 2e^- \quad (2)$$

Table 1 Summary of the electrochemical performance of manganese-based materials in ZIBs

Cathodes	Electrolyte	Voltage window	Specific capacity (current density)	Cycling performance	Ref.
α-MnO_2	2 M $ZnSO_4$ + 0.1 M $MnSO_4$	1–1.8 V	285 mA h g^{-1} (1/3C)	92% capacity retention over 5000 cycles at 5C	78
β-MnO_2	3 M $Zn(CF_3SO_3)_2$ + 0.1 M $Mn(CF_3SO_3)_2$	0.8–1.9 V	225 mA h g^{-1} (0.65C)	94% capacity retention over 2000 cycles at 6.5C	53
γ-MnO_2	1 M $ZnSO_4$	1–1.8 V	285 mA h g^{-1} (0.05 mA cm^{-2})	63% capacity retention over 40 cycles at 0.5 mA cm^{-2}	54
δ-MnO_2	1 M $Zn(TFSI)_2$ + 0.1 M $Mn(TFSI)_2$	1–1.8 V	238.8 mA h g^{-1} (0.2C)	93% capacity retention over 4000 cycles at 20C	79
ε-MnO_2	3 M $ZnSO_4$ + 0.1 M $MnSO_4$	0.8–1.8 V	312 mA h g^{-1} (0.1 A g^{-1})	80.1% capacity retention over 1000 cycles at 1 A g^{-1}	45
λ-MnO_2	0.2 M $ZnSO_4$ + 0.1 M $MnSO_4$	0.8–1.9 V	250 mA h g^{-1} (0.02 A g^{-1})	115 mA h g^{-1} over 500 cycles at 1 A g^{-1}	80
R-MnO_2	2 M $ZnSO_4$ + 0.1 M $MnSO_4$	0.8–1.85 V	168 mA h g^{-1} (0.1 A g^{-1})	118.3 mA h g^{-1} over 500 cycles at 0.3 A g^{-1}	56
T-MnO_2	1 M $ZnSO_4$	0.7–2.0 V	108 mA h g^{-1} (1/2C)	83% capacity retention over 50 cycles at 50 mA g^{-1}	57
MnO	2 M $ZnSO_4$	1–1.9 V	330 mA h g^{-1} (0.1 A g^{-1})	80.7% capacity retention over 300 cycles at 0.3 A g^{-1}	81
Mn_2O_3	2 M $ZnSO_4$ + 0.2 M $MnSO_4$	1.0–1.8 V	292 mA h g^{-1} (0.2C)	89% capacity retention over 3000 cycles at 3.08 A g^{-1}	82
Mn_3O_4	2 M $ZnSO_4$	0.8–1.9 V	85.6 mA h g^{-1} (0.2 A g^{-1})	106.1 mA h g^{-1} over 300 cycles at 0.5 A g^{-1}	83
Mn_8O_5/rGO	2 M $ZnSO_4$ + 0.1 M $MnSO_4$	0.8–1.9 V	260 mA h g^{-1} (0.1 A g^{-1})	98.8% capacity retention over 1000 cycles at 0.5 A g^{-1}	63
$ZnMn_2O_4$	1 M $ZnSO_4$ + 0.05 M $MnSO_4$	0.8–1.9 V	70.2 mA h g^{-1} (3.2 A g^{-1})	106.5 mA h g^{-1} over 300 cycles at 0.1 A g^{-1}	84
$MgMn_2O_4$	1 M $ZnSO_4$ + 1 M $MgSO_4$ + 0.1 M $MnSO_4$	0.5–1.9 V	247 mA h g^{-1} (0.05 A g^{-1})	80% capacity retention over 500 cycles at 0.5 A g^{-1}	65
$LiMn_2O_4$	1 M $ZnSO_4$ + 1 M Li_2SO_4 + 0.1 M $MnSO_4$	0.8–1.85 V	300 mA h g^{-1} (0.1 A g^{-1})	93.5% capacity retention over 500 cycles at 1 A g^{-1}	68
$CoMn_2O_4$	2 M $ZnSO_4$ + 0.2 M $MnSO_4$	0.8–1.9 V	232.3 mA h g^{-1} (0.1 A g^{-1})	—	85
$MnCo_2O_4$	2 M $ZnSO_4$ + 0.5 M $MnSO_4$	0.8–1.8 V	595.3 mA h g^{-1} (0.05 A g^{-1})	85% capacity retention over 250 cycles at 0.2 A g^{-1}	86
$Na_{0.44}MnO_2$	3 M $ZnSO_4$ + 0.1 M $MnSO_4$	1.0–1.8 V	301.3 mA h g^{-1} (0.1 A g^{-1})	69.3% capacity retention over 800 cycles at 1 A g^{-1}	87
MnS	2 M $ZnSO_4$ + 0.1 M $MnSO_4$	0.8–2 V	335.7 mA h g^{-1} (0.3 A g^{-1})	104 mA h g^{-1} over 4000 cycles at 3 A g^{-1}	73
Mn_2SiO_4	1 M $ZnSO_4$ + 0.1 M $MnSO_4$	1.0–1.8 V	154 mA h g^{-1} (0.1 A g^{-1})	55% capacity retention over 40 cycles at 0.1 A g^{-1}	74
$LaMnO_3$	2 M $ZnSO_4$ + 0.2 M $MnSO_4$	1.0–1.8 V	226 mA h g^{-1} (0.1 A g^{-1})	113 mA h g^{-1} over 1000 cycles at 0.5 A g^{-1}	76

Oh *et al.*[90] demonstrated the intercalation mechanism of Zn^{2+} in α-MnO_2 during discharge, involving an electrochemical-induced reversible phase transition of α-MnO_2 from a tunneled to layered structure. This transition is induced by the dissolution of manganese from α-MnO_2 during the discharge process, resulting in the formation of layered Zn-birnessite (11 Å). The original tunneled structure is restored through the incorporation of Mn^{2+} ions back into the layers of Zn-birnessite during charging (Fig. 5b). The reaction can be depicted as follows:

$$Mn^{4+}(s) + e^- \rightarrow Mn^{3+}(s) \quad (3)$$

$$2Mn^{3+}(s) \rightarrow Mn^{4+}(s) + Mn^{2+}(aq) \quad (4)$$

$$Mn^{2+}(aq) \rightarrow Mn^{4+}(s) + 2e^- \quad (5)$$

Later, the intercalation of Zn^{2+} ions into α-MnO_2 was rectified, resulting in the formation of buserite (11 Å) and the previously observed Zn-birnessite is attributed to the dehydration of the original buserite structure.[91] Owing to the narrow [1 × 1] tunnels in β-MnO_2, it has been suggested to be unfavorable for Zn intercalation. Interestingly, Chen *et al.*[53] revealed that tunnel-type β-MnO_2 undergoes a phase transition to layer-type Zn-buserite during the initial discharge process, followed by the reversible insertion/extraction of Zn^{2+} ions in the layered structure. The phase transition of MnO_2 during charge/discharge was deeply investigated by Alfaruqi *et al.*,[54] revealing a complex multiple-phase transformation process for γ-MnO_2. It was proposed that the original tunnel-type γ-MnO_2 undergoes a structural transformation to form a spinel-type Mn(III) phase ($ZnMn_2O_4$), as well as two new intermediary Mn(II) phases, namely tunnel-type γ-Zn_xMnO_2 and layered L-Zn_yMnO_2. These phases with multi-oxidation states coexist after complete electrochemical Zn-insertion (Fig. 5c). In addition, the presence of cation-defects in $ZnMn_2O_4$ spinel permits reversible Zn^{2+} insertion/extraction reactions, and the Mn deficiency in

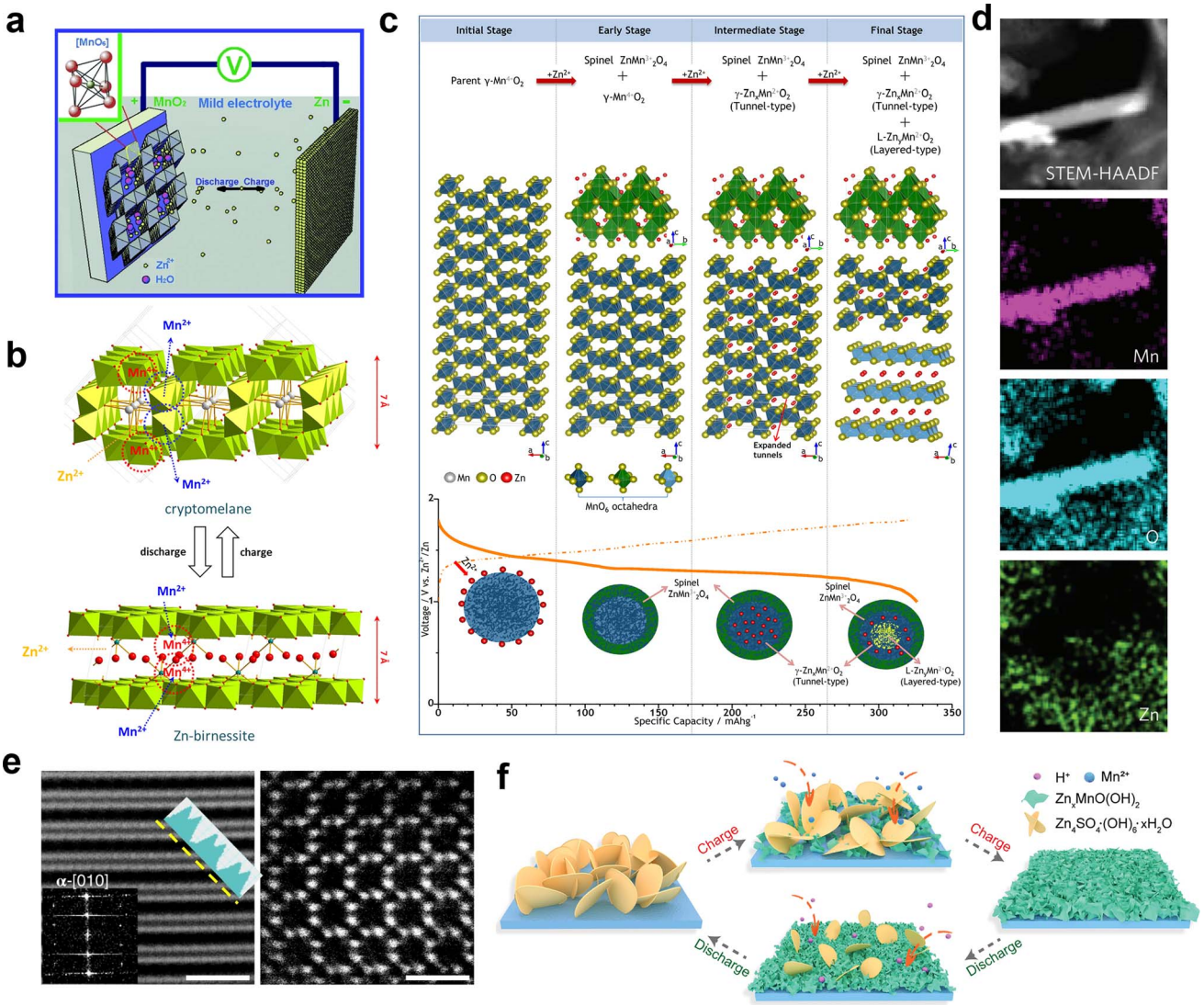

Fig. 5 Various energy storage mechanisms of manganese-based ZIBs. (a) Schematic of the chemistry of a zinc-ion battery. Reproduced with permission.[89] Copyright 2012, Wiley-VCH. (b) Schematic illustrating the mechanism of zinc intercalation in α-MnO_2. Reproduced with permission.[90] Copyright 2014, Springer Nature. (c) Schematic illustration of the reaction pathway of Zn-insertion in a γ-MnO_2 cathode. Reproduced with permission.[54] Copyright 2015, the American Chemical Society. (d) STEM-EDS mappings of the elemental distributions of Mn, O and Zn in the MnO_2 electrode in the discharged state during the first cycle. Reproduced with permission.[78] Copyright 2016, Springer Nature. (e) Atomic scale [001] and projections of MnO_2 demonstrating essentially 'empty' tunnels without presence of heavy cations. Reproduced with permission.[94] Copyright 2022, Springer Nature. (f) Schematic of the ZSH-assisted deposition–dissolution reaction model. Reproduced with permission.[95] Copyright 2022, Wiley-VCH.

$ZnMn_2O_4$ can effectively reduce the electrostatic barrier for Zn^{2+} diffusion, resulting in the enhanced mobility of Zn^{2+} ions, and consequently faster electrode reaction kinetics.[64] However, it is worth noting that while the mechanism of Zn^{2+} insertion/extraction was initially demonstrated by researchers, some of the early analyses may have been misleading due to the absence of advanced characterization techniques and limited understanding of ZIBs.

3.2 Chemical conversion reaction mechanism

Different from Zn^{2+} insertion in the MnO_2 host, which is responsible for energy storage, the chemical conversion reaction mechanism is a new discovery, which was first proposed by Pan *et al.*[78] During the discharge process, MnO_2 undergoes a reaction with H^+ derived from H_2O to form MnOOH. To achieve charge neutrality in the system, the remaining OH^- ions react with $ZnSO_4$ and H_2O in the aqueous electrolyte, resulting in the formation of large flake-like $ZnSO_4[Zn(OH)_2]_3 \cdot xH_2O$. The XRD pattern of the MnOOH phase and STEM-EDS mappings of the elemental distributions of Mn, O, and Zn in the discharged state strongly demonstrate the reaction chemistry between H^+ and MnO_2 in the cathode (Fig. 5d). In the absence of H^+, organic Zn^{2+}-based electrolytes exhibit limited capacity; however, upon the addition of H_2O, the Zn/α-MnO_2 battery demonstrates electrochemical behavior similar to that observed in aqueous electrolyte, thereby providing further evidence for the

occurrence of a chemical conversion reaction. The reaction chemistry can be formulated as follows:

$$\text{Cathode: } H_2O \leftrightarrow H^+ + OH^- \quad (6)$$

$$MnO_2 + H^+ + e^- \leftrightarrow MnOOH \quad (7)$$

$$\frac{1}{2}Zn^{2+} + OH^- + \frac{1}{6}ZnSO_4 + \frac{x}{6}H_2O \leftrightarrow \frac{1}{6}ZnSO_4\left[Zn(OH)_2\right]_3 \cdot xH_2O \quad (8)$$

$$\text{Anode: } \frac{1}{2}Zn \leftrightarrow \frac{1}{2}Zn^{2+} + e^- \quad (9)$$

$$\text{Overall: } MnO_2 + \frac{1}{2}Zn + \frac{x}{6}H_2O + \frac{1}{6}ZnSO_4 \leftrightarrow MnOOH + \frac{1}{6}ZnSO_4\left[Zn(OH)_2\right]_3 \cdot xH_2O \quad (10)$$

Although ample evidence has indicated the occurrence of chemical conversion reactions leading to the transformation of MnO_2 into MnOOH, the operando XRD study unequivocally confirmed the absence of a crystalline MnOOH phase. It is worth noting that *ex situ* analysis methods, such as highly crystalline ZHS, may introduce external interferences and occasionally mistake the formation of MnOOH.[92,93] Therefore, more advanced *in situ* characterization methods are required to further validate the mechanism of the chemical conversion reaction.

3.3 H^+ insertion/extraction mechanism

Different from the chemical conversion between MnO_2 and MnOOH revealed by Pan *et al.*, a view of H^+ intercalation in α-MnO_2 tunnels was proved by combining atomic-scale electron microscopy, electrochemistry and atomistic simulations.[94] The *in situ* XRD analysis revealed the absence of new phases except for the reversible generation and disappearance of ZHS. However, during discharge, the slight shifts in the peaks of α-MnO_2 towards lower angles indicate cation insertion. Down-tunnel STEM imaging demonstrated severe distortion of the tunnels near the surface region of MnO_2 nanowires, strongly supporting cation intercalation. Nevertheless, EDS mapping showed the absence of Zn element in MnO_2 nanowires, suggesting that Zn^{2+} insertion in the tunnels is unlikely. Furthermore, atomic-scale imaging clearly indicated the presence of unoccupied tunnels without any heavy cations, providing crucial evidence against Zn^{2+} insertion in the MnO_2 lattice (Fig. 5e). The computational results further support the favorability of H^+ insertion over Zn^{2+}. The reaction chemistry can be denoted as follows:

$$\alpha\text{-}MnO_2 + H^+ + e^- \leftrightarrow \alpha\text{-}H_1MnO_2 \quad (11)$$

3.4 H^+ and Zn^{2+} co-insertion/extraction mechanism

The H^+ and Zn^{2+} insertion/extraction mechanism is widely accepted and has been reported in numerous studies. Considering the existence of both H^+ and Zn^{2+} cations in the electrolyte, Wang *et al.*[96] were the first to demonstrate that MnO_2 undergoes successive H^+ and Zn^{2+} insertion processes. The reaction kinetics at different depths of discharge, as observed through GITT and EIS, indicated that the reaction on the first plateau occurs much faster than on the second plateau due to the smaller size of H^+ compared to Zn^{2+}. Furthermore, even without $ZnSO_4$ in the electrolyte, there was still evidence of H^+ insertion reactions occurring, with the first sloping plateau being attributed solely to H^+ insertion. Additionally, discharge down to 1.3 V and 1.0 V resulted in the formation of MnOOH and $ZnMn_2O_4$ respectively, further confirming the subsequent insertion of H^+ and Zn^{2+}. Subsequently, the study conducted by Jin *et al.*[79] also provided compelling evidence to substantiate the co-insertion mechanism. However, this investigation revealed that the intercalation of Zn^{2+} in MnO_2 is governed by a non-diffusion-controlled process, followed by H^+ conversion reaction, rather than the consequent insertion of H^+ and Zn^{2+}. These two distinct conclusions confuse researchers in terms of which cation reacts with MnO_2 firstly and should be disclosed by further evidence.

3.5 Dissolution/deposition mechanism

The dissolution of Mn^{2+} caused by Jahn–Teller distortion is commonly considered the reason for capacity attenuation.[42,44,97] Thus, to alleviate the issue of Mn dissolution, Mn^{2+} additives have been introduced to shift the disproportionation reaction $2Mn^{3+} \leftrightarrow Mn^{2+} + Mn^{4+}$.[78] However, Oh *et al.*[98] discovered that Mn^{2+} dissolved in the discharge state can be electro-oxidized back to MnO_2 through a reversible dissolution/deposition process of ZHS on the electrode surface, which is triggered by pH changes in the electrolyte. This phenomenon has been observed in MnO_2-based flow batteries with acidic electrolytes.[99]

$$\text{Cathode: } 3MnO_2 + 8Zn^{2+} + 2SO_4^{2-} + 16H_2O + 6e^- \rightarrow 3Mn^{2+} + 2Zn_4(OH)_6(SO_4)\cdot 5H_2O\downarrow \quad (12)$$

$$\text{Anode: } 3Zn \rightarrow 3Zn^{2+} + 6e^- \quad (13)$$

$$\text{Overall: } 3MnO_2 + 3Zn + 5Zn^{2+} + 2SO_4^{2-} + 16H_2O \leftrightarrow 3Mn^{2+} + 2Zn_4(OH)_6(SO_4)\cdot 5H_2O\downarrow \quad (14)$$

The dissolution/deposition mechanism was also confirmed by Liang and coworkers.[100] They concluded that the dissolution and deposition of MnO_2 contribute major capacity in the energy storage process. During the initial discharge, the dissolution of the original MnO_2 turns it to Mn^{2+} in the electrolyte, and in the subsequent charging process, Mn^{2+} is deposited on the electrode surface as birnessite-MnO_2 rather than the original MnO_2. In the subsequent cycles, birnessite-MnO_2 and Mn^{2+} are reversibly dissolved/deposited during charge/discharge.

$$\text{First cycle: } 3MnO_2 + 6H_2O + 6e^- \xrightarrow{\text{Discharge process}} 3Mn^{2+} + 12OH^- \quad (15)$$

$$3Mn^{2+} + 12OH^- - 6e^- \xrightarrow{\text{Charge process}} 3\ \text{birnessite-}MnO_2 + 6H_2O \quad (16)$$

Subsequent cycles: 3 birnessite-MnO_2 + $6H_2O$ + $6e^- \leftrightarrow 3Mn^{2+}$ + $12OH^-$ (17)

Side reaction: $12OH^- + 2SO_4^{2-} + 8Zn^{2+} + 8H_2O \leftrightarrow 2Zn_4(OH)_6SO_4 \cdot 4H_2O$ (18)

Wu *et al.*[101] further verified the Mn dissolution/deposition faradaic mechanism that governs the electrochemistry by providing direct evidence through operando, spatiotemporal-resolved synchrotron X-ray fluorescence mapping measurements on a custom aqueous Zn/α-MnO_2 battery. By simultaneously visualizing and quantifying the distribution of Mn species in the electrolyte, they observed the formation of aqueous Mn species during discharge and depletion upon charge.

Different from the MnO_2/Mn^{2+} dissolution/deposition reaction, Chen *et al.*[95] reported a zinc sulfate hydroxide-assisted dissolution/deposition reaction for aqueous Zn–Mn batteries. They found that the role of the α-MnO_2 cathode is to consume H^+ driving the generation of ZHS and the release of Mn^{2+} in the electrolyte provides an Mn source for the next charge deposition, with α-MnO_2 contributing little capacity in the subsequent cycles. The energy conversion occurs by the reversible dissolution/deposition between the layered $Zn_xMnO(OH)_2$ and ZHS (Fig. 5f). According to this energy storage mechanism, it is suggested that ZSH plays an essential role as an active material rather than being solely a byproduct affecting the cycling performance, contrary to previous literature reports.[43,100,102] Based on this understanding of ZSH-assisted deposition/dissolution reactions, successful designs of Zn–ZnO, Zn–MgO, and Zn–CaO batteries have been achieved. The energy storage mechanism is summarized as follows:

Charge: $Zn_4(OH)_6SO_4 \cdot 4H_2O + Mn^{2+} \rightarrow Zn_xMnO(OH)_2 + 4H^+ + SO_4^{2-} + 2e^-$ (19)

Discharge: $Zn_xMnO(OH)_2 + 4H^+ + 2e^- \rightarrow Zn^{2+} + Mn^{2+} + 3H_2O$ (20)

$6OH^- + SO_4^{2-} + 4Zn^{2+} + 4H_2O \rightarrow Zn_4(OH)_6SO_4 \cdot 4H_2O$ (21)

3.6 Hybrid storage mechanism

In recent years, an increasing number of reports has demonstrated that the energy storage mechanisms in Zn–Mn cells exhibit a hybrid storage mechanism rather than a singular mechanism. For example, in contrast to the previous simple phase transition, Xu *et al.*[103] revealed a complex phase evolution involving both intercalation and conversion reactions. During the initial discharge process, α-MnO_2 undergoes Zn^{2+} intercalation at around 1.4 V, resulting in the formation of α-Zn_xMnO_2. Subsequently, an H^+ conversion reaction occurs between 1.0 and 1.3 V, leading to the generation of MnOOH and Mn_2O_3 in the cathode, thereby increasing the electrolyte pH value and producing a byproduct known as $ZnSO_4 \cdot 3Zn(OH)_2 \cdot 5H_2O$ (BZSP) (Fig. 6a). The reaction can be described as follows:

$MnO_2 + xZn^{2+} + 2xe^- \rightarrow Zn_xMnO_2$ (22)

$4Zn^{2+} + SO_4^{2-} + 5H_2O + 6OH^- \rightarrow ZnSO_4 \cdot 3Zn(OH)_2 \cdot 5H_2O$ (23)

$MnO_2 + H^+ + e^- \rightarrow MnOOH$ (24)

$2MnO_2 + 2H^+ + 2e^- \rightarrow Mn_2O_3$ (25)

During the initial charging process, α-Zn_xMnO_2, MnOOH, and Mn_2O_3 revert to α-MnO_2 by the release of Zn^{2+} and H^+, while BZSP reacts with Mn^{2+} to form $ZnMn_3O_7 \cdot 3H_2O$ (Fig. 6b). This reaction can be described as follows:

$3(ZnSO_4 \cdot 3Zn(OH)_2 \cdot 5H_2O) + 3Mn^{2+} + 8e^- \rightarrow ZnMn_3O_7 + 3ZnSO_4 + 18OH^- + 8Zn^{2+} + 12H_2O$ (26)

In the subsequent cycles, Zn^{2+} undergoes reversible insertion/extraction in/from the α-MnO_2, α-Zn_xMnO_2, and $ZnMn_3O_7 \cdot 3H_2O$ hosts. The participation of Mn^{2+} leads to the formation of new phases including $Zn_2Mn_3O_8$ and $ZnMn_2O_4$ through reversible conversion (Fig. 6c). The reaction can be described as follows:

$Zn_xMnO_2 + (0.5 - x)Zn^{2+} + (1 - 2x)e^- \rightarrow 0.5ZnMn_2O_4$ (27)

$Zn_2Mn_3O_8 + Mn^{2+} \rightarrow 2ZnMn_2O_4$ (28)

Qiao *et al.*[104] reported the occurrence of multi-redox reactions during the discharge process, with three distinct discharge regions corresponding to three different reaction mechanisms. The region between 2–1.7 V results from the dissolution of MnO_2, while the region between 1.7–1.4 V is responsible for H^+ insertion into the residual MnO_2, and the region between 1.4–0.8 V is dominated by Zn^{2+} insertion in the residual MnO_2 (Fig. 6d), as confirmed by *ex situ* XRD and XPS measurements. Furthermore, the optimized addition 0.1 M H_2SO_4 significantly enhanced the energy density and maximized the electrolysis efficiency for two-electron reactions. The reaction can be written as follows:

Cathode: $MnO_2 + 4H^+ + 2e^- \leftrightarrow Mn^{2+} + 2H_2O$ (29)

$MnO_2 + H^+ + e^- \leftrightarrow MnOOH$ (30)

$MnO_2 + 0.5Zn^{2+} + e^- \leftrightarrow Zn_{0.5}MnO_2$ (31)

Anode: $Zn^{2+} + 2e^- \leftrightarrow Zn$ (32)

The H^+ conversion and Mn^{2+} dissolution/deposition mechanism of β-MnO_2 was demonstrated by Liu *et al.*[50] In the initial discharge cycle, β-MnO_2 undergoes a transformation to MnOOH and Mn^{2+}, while during charge, Mn^{2+} deposition and MnOOH conversion lead to the formation of ε-MnO_2. In subsequent cycles, the deposited ε-MnO_2 reacts with H^+ to generate MnOOH, which partially dissolves to form Mn^{2+}, accompanied by the formation of ZHS during the discharge process. Upon charging, Mn^{2+} is redeposited into the previously deposited ε-MnO_2, resulting in the disappearance of ZHS. The chemical equation can be written as follows:

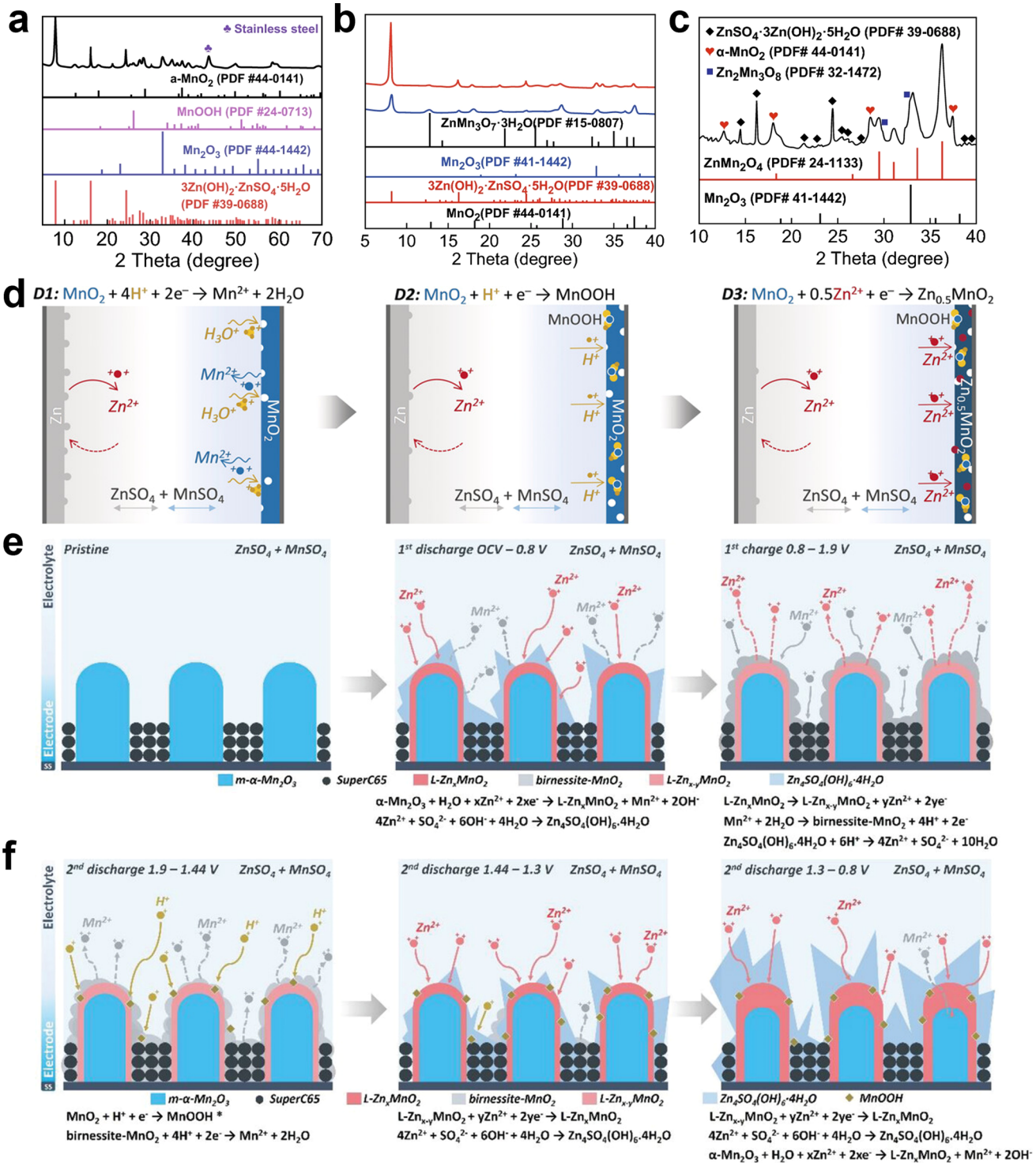

Fig. 6 Hybrid storage mechanism. XRD patterns of the α-MnO_2 cathode at different states: (a) discharged to 1.4 V in the first cycle, (b) fully charged state in the first cycle, and (c) after 100 cycles. (a)–(c) Reproduced with permission.[103] Copyright 2019, Springer Nature. (d) Schematic representation and charge storage mechanism of an MnO_2–Zn ion battery in 1 M $ZnSO_4$ and 1 M $MnSO_4$ electrolyte. Reproduced with permission.[104] Copyright 2019, Wiley-VCH. Schematic illustration of the different contributions to the charge storage mechanism of m-α-Mn_2O_3 during (e) first discharge and charge process and (f) second discharge process. (e) and (f) Reproduced with permission.[105] Copyright 2021, Wiley-VCH.

$$\text{Cathode: } MnO_2 + H^+ + e^- \leftrightarrow MnOOH \quad (33)$$

$$MnOOH + 3H^+ + 3e^- \leftrightarrow Mn^{2+} + H_2O \quad (34)$$

$$4Zn^{2+} + SO_4^{2-} + 8H_2O \leftrightarrow Zn_4(OH)_6SO_4\cdot 5H_2O + 6H^+ \quad (35)$$

$$\text{Anode: } Zn \leftrightarrow Zn^{2+} + 2e^- \quad (36)$$

The energy storage mechanism of α-Mn_2O_3 was systematically and comprehensively investigated by Ma *et al.*[105] They demonstrated that α-Mn_2O_3 is unsuitable for H^+ insertion. In fact, α-Mn_2O_3 undergoes an irreversible phase transition to layer-type L-Zn_xMnO_2 by electrochemical reaction with H_2O and Zn^{2+}, accompanied by the dissolution of Mn^{2+} in the electrolyte. This process leads to the formation of OH^-, ultimately generating ZHS in the first discharge process. During the first charge process, Zn^{2+} extraction from L-Zn_xMnO_2 forms L-$Zn_{x-y}MnO_2$, while Mn^{2+} is oxidized to Mn(IV), resulting in the deposition of birnessite-MnO_2 on the outer surface of the electrode (Fig. 6e). The ZHS fades due to the formation of H^+ by deposition of Mn^{2+}. In the second discharge process between 1.9–1.44 V, H^+ insertion in MnO_2 (formed from L-Zn_xMnO_2 and Mn^{2+}) leads to the generation of MnOOH. In the range of 1.44–0.8 V, Zn^{2+} inserts in L-$Zn_{x-y}MnO_2$, together with formation of ZSH, and it should be noted that the residual α-Mn_2O_3 will continue undergoing an irreversible phase transition in the range of 1.3–0.8 V until it completely transforms into L-Zn_xMnO_2 and Mn^{2+}, as shown in Fig. 6f.

In summary, the storage mechanisms of manganese-based ZIBs including Zn^{2+} insertion/extraction, chemical conversion reaction, H^+ insertion/extraction, H^+ and Zn^{2+} co-insertion/extraction, dissolution/deposition and hybrid storage mechanisms have been extensively investigated by researchers. However, although significant advancements have been made in determining the storage mechanisms of manganese-based ZIBs over the past decade, their intricate reaction chemistry is still under debate, hindering a consensus. Moreover, the underlying causes of different storage mechanisms and some abnormal phenomena such as the unusual "turning point" of the GCD curve have not been reasonably explained, resulting in obscure optimization strategies based on the storage mechanism and further impeding their practical application. Therefore, more efforts are urgently needed to determine the real reaction chemistry of manganese-based ZIBs during charge/discharge.

4 The mechanisms of capacity fluctuation

Although numerous studies have demonstrated the long-term cycling performance of manganese-based ZIBs at high C-rates (≥5C),[56,79,102] it should be noted that this excellent performance is primarily attributed to capacitive processes dominating the capacity contribution rather than the typical diffusion-controlled charge storage mechanisms for batteries.[18] Given the ongoing controversy regarding the primary causes of battery failure, there is a lack of robust methods to enhance the cycling stability of manganese-based ZIBs, particularly at a low current. Besides the crucial challenges encountered by Zn anodes such as dendrite growth, passivation, corrosion and hydrogen evolution,[106–108] on the cathode side, issues such as Mn dissolution, dramatic volume changes, and the irreversible consumption of Mn^{2+} lead to the generation of electrochemically inactive materials, which can result in severe performance degradation and even battery failure.[109–111] Furthermore, the phenomenon of capacity activation, which commonly occurs during the initial cycles, has received limited attention from researchers. In general, the long-term cycling behavior of manganese-based ZIBs consists of an activation period, a stabilization period, and ultimately a decay period. However, previous review articles failed to address the underlying reasons for the dynamic capacity fluctuation from capacity activation to capacity attenuation, resulting in inadequate guidance and references for enhancing the cycling stability of manganese-based ZIBs. Thus, the mechanisms of capacity degradation, capacity activation, and dynamic capacity fluctuation are discussed in the following sections.

4.1 Capacity degradation mechanisms

4.1.1 Jahn–Teller distortion. Most manganese-based materials consist of basic octahedral units (MnO_6) interconnected through corner and/or edge sharing, with the Mn cation located at the center of each MnO_6 octahedron adopting a six-oxide coordination. Under the influence of an electric field, the 3d orbitals of the Mn cation in the MnO_6 octahedra split into two degenerate orbitals, namely e_g and t_{2g}. Due to the lower formation energy of the triply degenerate t_{2g} orbitals (d_{xy}, d_{xz} and d_{yz}) compared to the doubly degenerate e_g orbitals (d_{z^2} and $d_{x^2-y^2}$), the three electrons in the 3d orbital in Mn^{4+} will occupy the d_{xy}, d_{xz} and d_{yz} orbitals, respectively, forming a stable structure. However, once Mn^{4+} gains an electron through the reduction process to form Mn^{3+}, in addition to occupying the d_{xy}, d_{xz} and d_{yz} orbitals, the remaining electron in the 3d orbital of Mn^{3+} will occupy the d_{z^2} orbital in e_g. The asymmetry of the electron distribution between the d_{z^2} and $d_{x^2-y^2}$ orbitals in Mn^{3+} leads to the distortion of the MnO_6 geometry from octahedral to tetragonal symmetry by lowering the overall energy.[34,112] Consequently, this distortion induces elongation of two axial Mn–O bonds and contraction of four equatorial Mn–O bonds (Fig. 7a). These changes can be observed through *in situ* Raman spectroscopy as a shift towards higher wavenumbers for the peak corresponding to the Mn–O stretching vibrations during the discharge processes.[112]

It has been widely acknowledged that the Jahn–Teller distortion during discharge leads to the disproportionation of Mn^{3+} ($2Mn^{3+} \rightarrow Mn^{2+} + Mn^{4+}$), resulting in the release of Mn^{2+} and causing severe dissolution issues. A consensus has been reached regarding the detrimental impact of inevitable Mn dissolution on the rapid capacity decay observed in manganese-based ZIBs, which is attributed to the loss of active cathode materials for reactions. Also, it has been unveiled that approximately 1/3 of the total manganese on the electrode dissolves in the electrolyte after the full discharge.[90] Once the outermost manganese atoms dissolve in the electrolyte, the subsequent dissolution of subsurface atoms occurs through a chain reaction, leading to structural collapse (Fig. 7b).[113] Moreover, the irreversible phase transformations, considerable strain, and unstable interface triggered by the Jahn–Teller distortion lead to structural degradation, eventually resulting in capacity

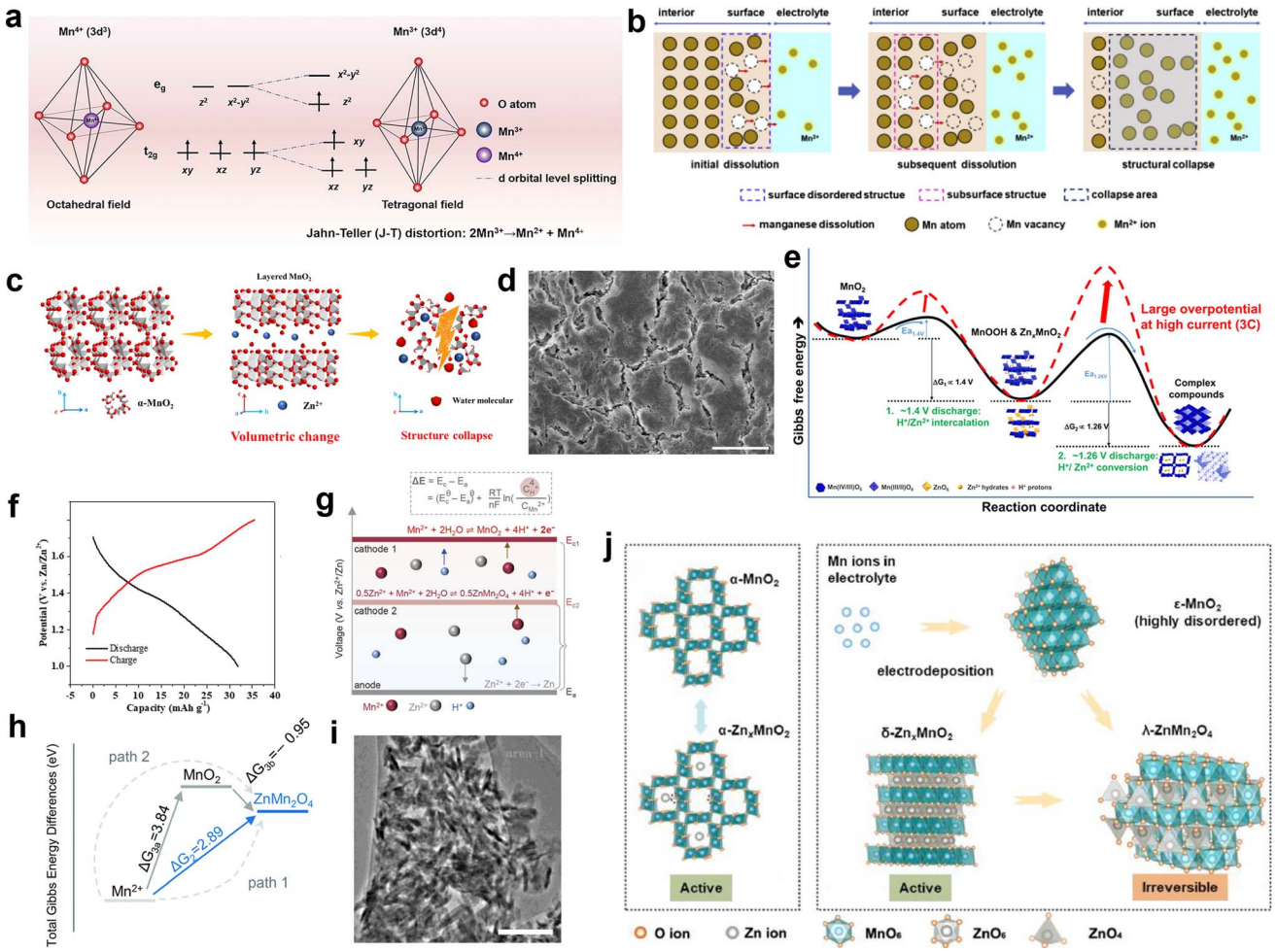

Fig. 7 Mechanisms of capacity degradation. (a) Mechanism of Jahn–Teller distortion. Reproduced with permission.[34] Copyright 2023, the Royal Society of Chemistry. (b) Manganese dissolution caused by the unstable or disordered surface. Reproduced with permission.[113] Copyright 2020, Elsevier. (c) Large volumetric change induced by phase transition. Reproduced with permission.[116] Copyright 2020, Elsevier. (d) Electrode pulverization induced by large volumetric change. Reproduced with permission.[53] Copyright 2017, Springer Nature. (e) Kinetic properties of the redox reactions in Zn/MnO_2 cells. Reproduced with permission.[117] Copyright 2019, the American Chemical Society. (f) Galvanostatic charge/discharge curve of $ZnMn_2O_4$. Reproduced with permission.[49] Copyright 2019, Elsevier. (g) Relationship between pH values and the potentials of Mn^{2+} deposition based on the Nernst equation. Reproduced with permission.[119] Copyright 2023, Wiley-VCH. (h) Total Gibbs energy differences for two possible reaction paths. Reproduced with permission.[120] Copyright 2022, the Royal Society of Chemistry. (i) TEM image of the MnO_2 electrode with 100 cycles. Reproduced with permission.[94] Copyright 2022, Springer Nature. (j) Schematic illustration of the crystal structural transformation. Reproduced with permission.[102] Copyright 2021, Elsevier.

degradation. In short, during the cycling process of manganese-based ZIBs, the presence of Jahn–Teller distortion poses a significant challenge given that it leads to crystal structure deterioration and the gradual loss of active materials, resulting in a rapid performance degradation.

4.1.2 Dramatic volume changes. Previous studies have demonstrated that manganese-based LIBs undergo large volume changes due to the shuttle of Li^+ caused by lattice expansion or contraction.[114] Similarly, repetitive insertion/extraction of hydrated H^+/Zn^{2+} ions will cause significant volume changes in manganese-based ZIBs. In comparison with Li^+ ions (0.76 Å), the larger hydrated radius of Zn^{2+} ions (4.3 Å) will destabilize and weaken the crystal framework, resulting in irreversible volumetric alterations and structural damage. In addition, the strong electrostatic force between Zn^{2+} ions and the host materials results in aggravated volume expansion and sluggish Zn^{2+} diffusion.[115] Furthermore, the irreversible phase transformation from a tunnel to layer or spinel structure during the charge/discharge process can lead to drastic volume changes, causing pulverization, cracking, and collapse of the active materials (Fig. 7c and d).[34,53,116] Once structural collapse occurs, some of the active materials will lose electrical contact with the current collector, resulting in the formation of dead Mn. The dramatic volume changes not only compromise the structure stability and lead to the loss of active materials, but also reduce the electrochemical activity of manganese-based cathode materials, resulting in capacity fading and poor rate performance. Yang *et al.*[117] conducted a comprehensive investigation combining experimental and theoretical approaches to elucidate the rapid capacity degradation observed in Zn/MnO_2 batteries, corresponding to the irreversible phase transformations occurring at the discharge plateaus of around

1.26 V, which are considered kinetically limiting reactions (Fig. 7e). The conversion reactions induce a large volume change and lead to the formation of electrochemically inactive ZHS. Thus, by increasing the lower cutoff voltage from 1.0 to 1.3 V, the kinetically limited irreversible reactions can be directly eradicated. As a result, when charged/discharged in the potential range of 1.3–1.8 V at a low current density of 1C, stable capacity retention over 150 cycles was achieved.

4.1.3 Irreversible consumption of Mn^{2+} to generate inactive manganese compounds. The essential reason for the capacity fading of manganese-based cathodes upon cycling is the loss of active materials. During the period of capacity decay, it is commonly observed that the original active cathode materials exhibit reduced crystallinity with the formation of electrochemically inactive manganese compounds on the cathode, such as $ZnMn_2O_4$, Mn_3O_4, and $ZnMn_3O_7$. Consequently, many reports suggested that the formation of an inert manganese compound phase is responsible for the ultimate performance attenuation.[43,49,93]

Taking hetaerolite $ZnMn_2O_4$ as a representative example, Zn^{2+} migration in the perfect spinel $ZnMn_2O_4$ is difficult due to their strong electrostatic repulsion. Additionally, $ZnMn_2O_4$ exhibits high resistivity, which is six orders of magnitude higher than that of MnO_2,[118] resulting in poor electrode conductivity. Consequently, when $ZnMn_2O_4$ was used as a cathode material, only an ultralow discharge capacity of $\sim$32.6 mA h g^{-1} could be delivered at 0.05C (Fig. 7f), manifesting its strong electrochemical inactivity.[49] Moreover, once a few of irreversible $ZnMn_2O_4$ nanoparticles are accumulated on the cathode surface, a mass of nucleation sites will be produced, inducing the formation of more $ZnMn_2O_4$ nanoparticles. The coverage of abundant $ZnMn_2O_4$ nanoparticles on the electrode would impede cation diffusion and the charge transport of the inner active materials. Unfortunately, these $ZnMn_2O_4$ nanoparticles cannot be electrochemically decomposed during the charging process as long as they are formed and attached to the electrode, which can be a crucial reason accounting for the capacity degradation of manganese-based cathodes after long-term cycling.

There are two primary mechanisms responsible for the formation of inactive $ZnMn_2O_4$ nanoparticles, where one is attributed to the conversion of tunnel or layered-$Zn_xMn_2O_4$ due to the higher thermodynamic stability of spinel $ZnMn_2O_4$, as shown in the following process:

$$MnO_2 + xZn^{2+} + 2xe^- \rightarrow Zn_xMnO_2 \quad (37)$$

$$Zn_xMnO_2 \rightarrow \lambda\text{-}ZnMnO_2 + 2(x-1)Zn^{2+} + (4x-2)e^- \quad (38)$$

The other involves an electrodeposition reaction from an Mn^{2+}-containing electrolyte, which can be denoted as:

$$2Mn^{2+} + Zn^{2+} + 8OH^- \rightarrow ZnMn_2O_4 + 4H_2O + 2e^-,\ E = 1.320\ V\ vs.\ Zn/Zn^{2+} \quad (39)$$

The electrodeposition potential of Mn^{2+} to form MnO_2 is known to be 1.869 V (*vs.* Zn/Zn^{2+}),[121] which is higher than that of $ZnMn_2O_4$ (Fig. 7g). In addition, the Gibbs energy of path 1 is lower than that of path 2 (Fig. 7h). Moreover, theoretical calculation indicates a lower formation energy compared to MnO_2.[120] These pieces of evidences indicate that the generation of $ZnMn_2O_4$ is favored by electrodeposition. Based on the aforementioned analyses and equation, it is evident that the concentration of Mn^{2+} will eventually decrease significantly due to the continuous formation of an irreversible $ZnMn_2O_4$ phase, leading to loss of active materials based on the Mn^{2+} electrodeposition reaction.

The capacity decay resulting from H^+ insertion/extraction was elucidated by Yuan *et al.*[94] With an increase in the cycle number, MnO_2 nanowires gradually dissolved, and some tiny needle-like nanograins were discovered after 50 cycles, which were identified as the Zn–Mn–O phase. Notably, the number of Zn–Mn–O nanograins kept increasing with an increase in the number of cycles, and almost all the nanowires were converted to Zn–Mn–O after 100 cycles, as shown in Fig. 7i. Meanwhile, the concentration of Mn^{2+} kept increasing within 50 cycles due to the Mn^{3+} disproportionation reaction, which is consistent with the TEM results. However, the Mn^{3+} disproportionation reaction was largely but not totally reversible, leading to the gradual loss of active MnO_2, and the accumulation of dissolved Mn^{2+} was thermodynamically favored to form the irreversible Zn–Mn–O phase due to the reprecipitation Mn^{2+}, resulting in a rapid decrease in Mn^{2+} concentration and capacity. In addition, by disassembling an *in situ* cell after 5000 cycles, Wei *et al.*[122] found that the capacity fading during long-term cycling was attributed to the irreversible consumption of Mn^{2+} in the electrolyte, where Mn^{2+} is irreversible converted to the woodruffite phase ($ZnMn_3O_7 \cdot 2H_2O$) with poor electrochemical activity, leading to a performance decay based on the capacity contribution from the dissolution/deposition of Zn-birnessite. Liang *et al.*[102] concluded that the *in situ* electrodeposition of MnO_2 from pre-added Mn^{2+} during the charging process should be a side reaction, where Mn^{2+} in the electrolyte is consumed to form ε-MnO_2. However, ε-MnO_2 will irreversibly convert to the inactive λ-$ZnMn_2O_4$, leading to capacity decay (Fig. 7j), which was also confirmed by Xia and coworkers.[123] In addition, the depletion of the Mn^{2+} electrolyte to generate irreversible λ-$ZnMn_2O_4$ will accelerate the disproportionation reaction, thereby triggering the dissolution of more original active MnO_2. Moreover, it was found that pre-adding a large amount of Mn^{2+} did not improve the cycle stability; in contrast, excess Mn^{2+} in the electrolyte promoted the conversion of Mn^{2+} to the $ZnMn_2O_4$ phase, leading to severe capacity fading and even battery failure.[124]

4.2 Capacity activation mechanisms

4.2.1 Electrodeposition of Mn^{2+}. It is recognized that the Mn^{2+} additive in the electrolyte plays an important role in achieving a sustainable cycling performance for manganese-based ZIBs. Early studies have found that the pre-added Mn^{2+} can effectively suppress the dissolution of the cathode by alleviating the disproportionation of Mn^{3+} ($2Mn^{3+} \rightarrow Mn^{2+} + Mn^{4+}$) caused by Jahn–Teller distortion.[78] Nevertheless, according to

the Nernst eqn (40), a high pH value can reduce the oxidation and deposition potential of Mn^{2+}, and recent investigations have concluded that Mn^{2+} in a high pH environment created by ZSH can be oxidized at a low charging potential.[95] It has even been reported that active MnO_2 can be electrodeposited on the substrate from the $MnSO_4$-based electrolyte, with an electrodeposition plateau at around 1.73 V. Also, the *in situ* formed MnO_2 can be directly used for subsequent discharge/charge with the typical GCD curve (Fig. 8a).[117] In electrolyte containing 2 M $ZnSO_4$ and 0.1 M $MnSO_4$, when the charge cut-off voltage was 1.7 V, no new diffraction peaks could be detected in the XRD pattern in the fully charged state; meanwhile, the cycling performance showed fast capacity fading. However, when the charge cut-off voltage increased to 1.8 or 1.9 V, a new set of peaks emerged in the fully charged state, which can be well indexed to ε-MnO_2 (Fig. 8b), accompanied by an increase in capacity with an increase in the number of cycles.[123] These findings suggest that the Mn^{2+} ions in the electrolyte can be electro-oxidized at a high potential, and the increased capacity is attributed to the newly formed MnO_2.

$$E = \frac{RT}{nF}\ln\left(\frac{c_{H^+}{}^4}{c_{Mn^{2+}}}\right) \quad (40)$$

The identification of electro-oxidized compounds with a nanosheet morphology is challenging due to their low crystallinity and complex components in the bulk cathode. In the literature, ε-MnO_2,[102,123] birnessite,[56,122] vernadite,[95,128] and their

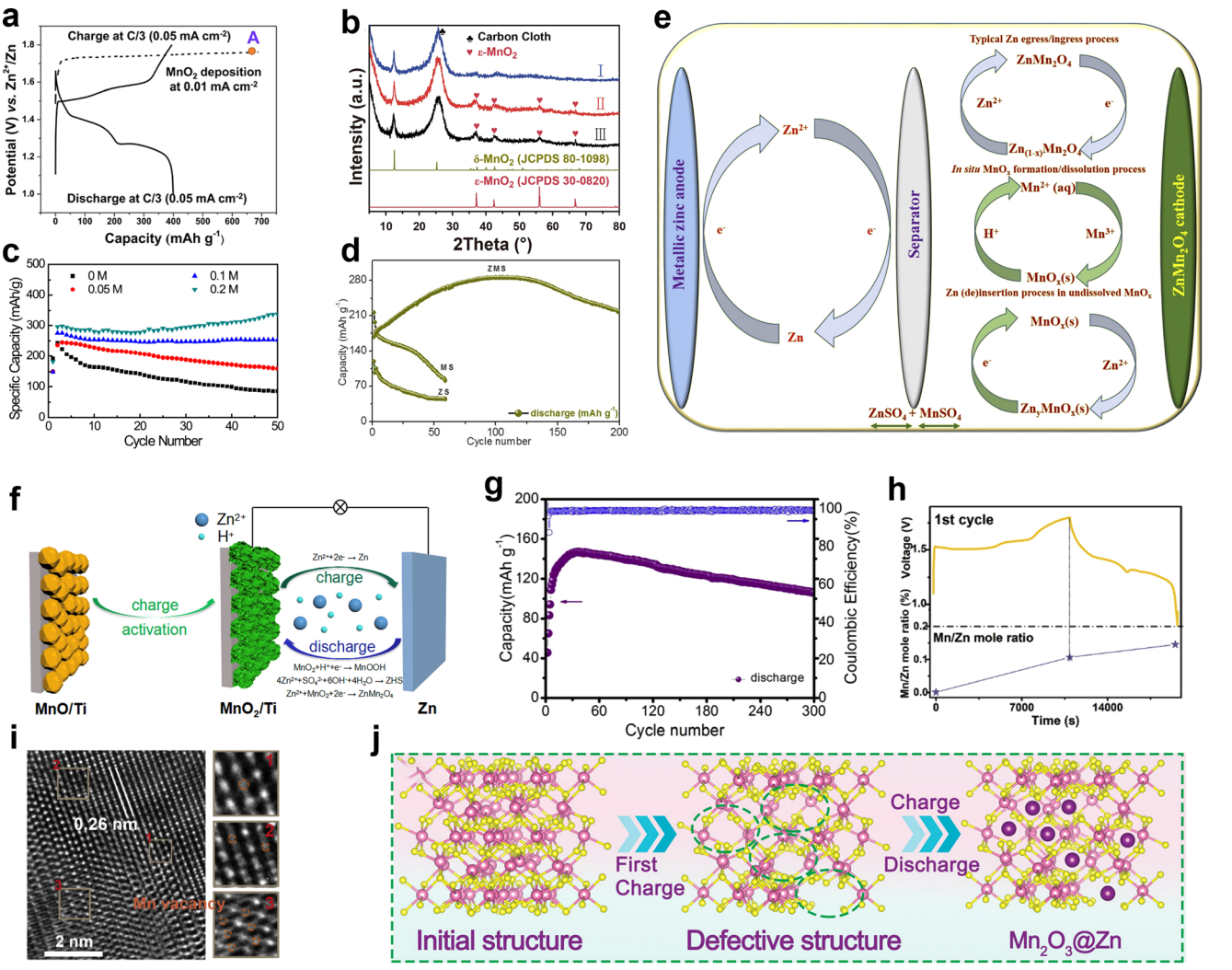

Fig. 8 Mechanisms of capacity activation. (a) Electrodeposition of MnO_2. Reproduced with permission.[117] Copyright 2019, the American Chemical Society. (b) XRD patterns of the MnO_2/CC electrodes in the first charge state with different charge cut-off voltages. Reproduced with permission.[123] Copyright 2020, Elsevier. (c) Effect of the Mn^{2+} additive concentration in the electrolyte on the cycling performance. Reproduced with permission.[125] Copyright 2019, Springer Nature. (d). Capacity activation of the $ZnMn_2O_4$/Zn cell. (e) Electrochemical reactions inside the $ZnMn_2O_4$/Zn cell. (d and e) Reproduced with permission.[126] Copyright 2020, Elsevier. (f) Diagram of energy storage mechanism for the MnO cathode of ZIBs. Reproduced with permission.[81] Copyright 2019, Elsevier. (g) Cycling performance of the Zn/Mn_3O_4 battery. Reproduced with permission.[83] Copyright 2018, Elsevier. (h) Elemental analysis of dissolved Mn^{2+} ions in 2 M $ZnSO_4$ electrolyte during cycling. (i) HRTEM of 1st fully charged state. (h and i) Reproduced with permission.[60] Copyright 2020, Elsevier. (j) Schematic diagram of Zn^{2+} storage mechanism of Mn_2O_3. Reproduced with permission.[127] Copyright 2023, Wiley-VCH.

Zn compounds have been reported for electro-oxidized manganese oxides. But the newly formed MnO_x on the electrode surface caused by re-oxidation of Mn^{2+} compensating the capacity decay has reached a consensus. It has been reported that about 18.9% of the capacity is attributed to the contribution of pre-added Mn^{2+}.[129] However, the concentration of the Mn^{2+} additive has a significant influence on the electrodeposited MnO_x. In an electrolyte with no Mn^{2+} additive, the capacity of MnO_2 decayed rapidly; however, with an increasing concentration of Mn^{2+} additive, the cycling stability gradually improves (Fig. 8c). Nevertheless, when the additive concentration reached 0.2 M, an increase in capacity was observed with cycle number due to the deposition of a large amount of aggregated nanosheets on the electrode surface.[125] These aggregated nanosheets augmented the active mass at the cathode, and consequently enhanced the cycling performance. Furthermore, Kim *et al.*[126] provided a deep comprehension of the role played by pre-added Mn^{2+} in the exceptional performance of a $ZnMn_2O_4$ cathode (Fig. 8d). They proposed that the additional capacity comes from two parts, where one is based on the quasi-reversible *in situ* electro-deposition/dissolution of MnO_x from pre-added Mn^{2+}, and the other is based on the reversible insertion/extraction of Zn^{2+} from undissolved MnO_x (Fig. 8e), which may be generated from the incomplete dissolution process due to the gradual pH changes during the electrochemical cycling process.

Besides the contribution of pre-added Mn^{2+} to the increased capacity, the dissolved Mn^{2+} from the original cathode material also leads to performance activation. For instance, it has been observed that MnO, which was previously considered inactive for Zn^{2+} storage due to its lack of tunnels, exhibits a competitive electrochemical performance comparable to MnO_2 after undergoing an activation process. Chen *et al.*[130] attributed the activation of MnO to its spontaneous dissolution in $ZnSO_4$ electrolyte, which can be denoted as eqn (41). The spontaneous dissolution behavior of MnO provides adequate Mn^{2+} for the ZSH-assisted deposition/dissolution reaction and results in performance activation, where the energy storage mechanism can be described by eqn (19)–(21). Besides, it was found that there is a positive correlation between capacity and rest time of MnO, manifesting that the dissolution of Mn plays a key role in the performance activation.

$$MnO + 2H^+ \rightarrow Mn^{2+} + H_2O \quad (41)$$

4.2.2 Electrochemical oxidation in the charging process. Additionally, it has been reported that the inert MnO can be activated by electrochemical oxidation in the charging process, leading to the formation of active MnO_x ($x > 2$), which serves as the active phase for the reversible insertion/extraction in the following cycles. Kang *et al.*[81] claimed that the electrochemical oxidation of MnO into porous layered-type MnO_2 nanosheets in the initial charging process is responsible for MnO activation. Combined with the phase, morphology evolution and increased Mn valence (3.9), it is evident that the surface of the MnO particles is partially oxidized into layered-type MnO_2 nanosheets, serving as electro-active sites for subsequent energy storage (Fig. 8f). Sun *et al.*[131] further confirmed this activation transition process, wherein MnO undergoes sequential oxidization to form layered-type MnO_2 in the initial few cycles, resulting in performance activation. In addition, Mn_3O_4, which is electrochemically inactive in alkaline Zn–MnO_2 batteries, it has also been reported to exhibit a good electrochemical performance in ZIBs.[83] An *ex situ* XRD analysis revealed the formation of Mn_5O_8 and birnessite after the first charging process. As cycling proceeded, the peak intensity of Mn_3O_4 weakened, while the peaks corresponding to birnessite became much stronger, indicating a transformation from Mn_3O_4 to birnessite. It should be noted that Mn_5O_8 is an intermediate product resulting from the incomplete electrochemical oxidation reaction and will finally transfer to birnessite after further electrochemical oxidation. The gradual generation of both the Mn_5O_8 intermediate and birnessite through the progressive electrochemical oxidation of Mn_3O_4 contributes to a gradual increase in capacity during the initial tens of cycles (Fig. 8g).

4.2.3 Mn-defects. Besides spontaneous dissolution and electrochemical oxidation, which contribute to the performance activation of MnO, *in situ*-generated Mn-defects also play a significant role in comprehending its performance activation. Zhou *et al.*[60] first reported that the induction of Mn defects through an *in situ* electrochemical process can achieve the activation of MnO (Fig. 8h and i). The electrochemical extraction of Mn^{2+} from the MnO host during charging provides more accessible channels for Zn^{2+} insertion/extraction. DFT calculations further confirmed the electrochemical activation of MnO caused by Mn defects, given that the differential charge density implies that electrons easily accumulate around the Mn defects to form a strong electrostatic field, which is highly favorable for Zn^{2+} adsorption. However, the uniform charge distribution of pristine MnO may cause severe destruction to the MnO framework upon Zn^{2+} insertion. The activation of MnO through charge-induced Mn dissolution was also verified by Zhao *et al.*[59] They concluded that the cycling performance of MnO is strongly related to the concentration of pre-added Mn^{2+}, where insufficient amounts of Mn^{2+} in the electrolyte can lead to severe structural deterioration due to the greater dissolution of Mn, while an excess amount may over-suppress its dissolution. In addition, the Mn_2O_3/CoO heterointerface with poor initial discharge capacity was found to be activated by the Mn-defects in the charging process.[127] The distortion of Mn_2O_3 due to Zn^{2+} insertion in the initial cycles will lead to the easy release of Mn atoms from the framework during charging, resulting in the formation of Mn vacancies (Fig. 8j). Furthermore, a strong internal electric field is generated at the interface of the heterostructure due to the homogeneous charge distribution of Mn_2O_3/CoO heterointerface, which will induce strong electrostatic fields at the Mn species for electron rearrangement. Owing to the similar ionic radius of Zn^{2+} and Mn^{2+}, the Mn dissolved from the host structure acts as a sacrificial site, providing more insertion sites and channels for Zn^{2+} insertion, leading to performance activation.

4.3 Dynamic capacity fluctuation for long-term cycling

4.3.1 The evolution of active materials. In conjunction with the analysis of cycling performance, *ex situ* XRD results, and morphology evolutions, Chen and colleges concluded that the evolution of the active materials is responsible for capacity fluctuation.[56] As shown in Fig. 9a, it is noticeable that the cycling performance of MnO_2 shows an obviously capacity fluctuation with an arched trend. The capacity increased rapidly during the initial cycles but subsequently decayed rapidly after reaching the peak value. The *ex situ* XRD patterns show that the diffraction peak intensity of MnO_2 gradually decreased in the initial cycles, manifesting the continuous dissolution of MnO_2 with an increase in the number of cycles. Moreover, numerous newly deposited birnessite nanosheets with low crystallinity were found on the electrode surface, indicating that the dissolved Mn^{2+} from the original MnO_2 was converted to birnessite during charging. Birnessite with specific nanosheet structures is electrochemical active, which can provide more reaction sites than the original MnO_2. Additionally, the deposition of birnessite compensates for the capacity loss caused by MnO_2 dissolution, resulting in performance activation. A similar activation mechanism of MnO was investigated simultaneously by Sun *et al.*[132] However, with a further increase in the number of cycles, the birnessite nanosheets faded and the $ZnMn_2O_4$/Mn_3O_4 phase emerged. Unfortunately, both $ZnMn_2O_4$ and Mn_3O_4 are electrochemically inactive due to their inaccessible pathways for Zn^{2+}/H^+ insertion/extraction, resulting in limited capacity delivery. As the intensity of the signals for the $ZnMn_2O_4$/Mn_3O_4 phase continued to increase, a noticeable capacity degradation was observed during the subsequent cycling. In addition, owing to the competition between activation towards birnessite and degradation towards $ZnMn_2O_4$/Mn_3O_4, a transitional period with a relatively stable capacity existed between the activation and decay processes. However, once most of the original MnO_2 was converted to birnessite, severe capacity attenuation occurred (Fig. 9b). Moreover, it should be noted that the fluctuation tendency is closely associated with the current density, where with an increase in current density, MnO_2 exhibited enhanced cycling stability. This can be attributed to the mild dissolution issue of the original MnO_2, followed by the slow deposition and conversion reaction rate under high currents.

4.3.2 The evolution of capacity contribution ratio from Mn^{2+}. Chao *et al.*[120] proposed a competitive capacity evolution (Mn-CCE) protocol to elucidate the capacity fluctuation behavior of manganese-based ZIBs. Based on the fluctuation characteristics and capacity contribution ratio from Mn^{2+} (CfM), the cycle curve can be divided into four distinct regions, as illustrated in Fig. 10a. Firstly, region I exhibits a rapid capacity increase at the beginning and ends with a slower growth rate; next, region II presents a mild ascending trend of capacity after region I; then, region III displays an evident rising trend of capacity, which ends with the peak value; finally, region IV demonstrates a quick downward trend in capacity. The magnitude of the variation in Zn^{2+} within region I was found to

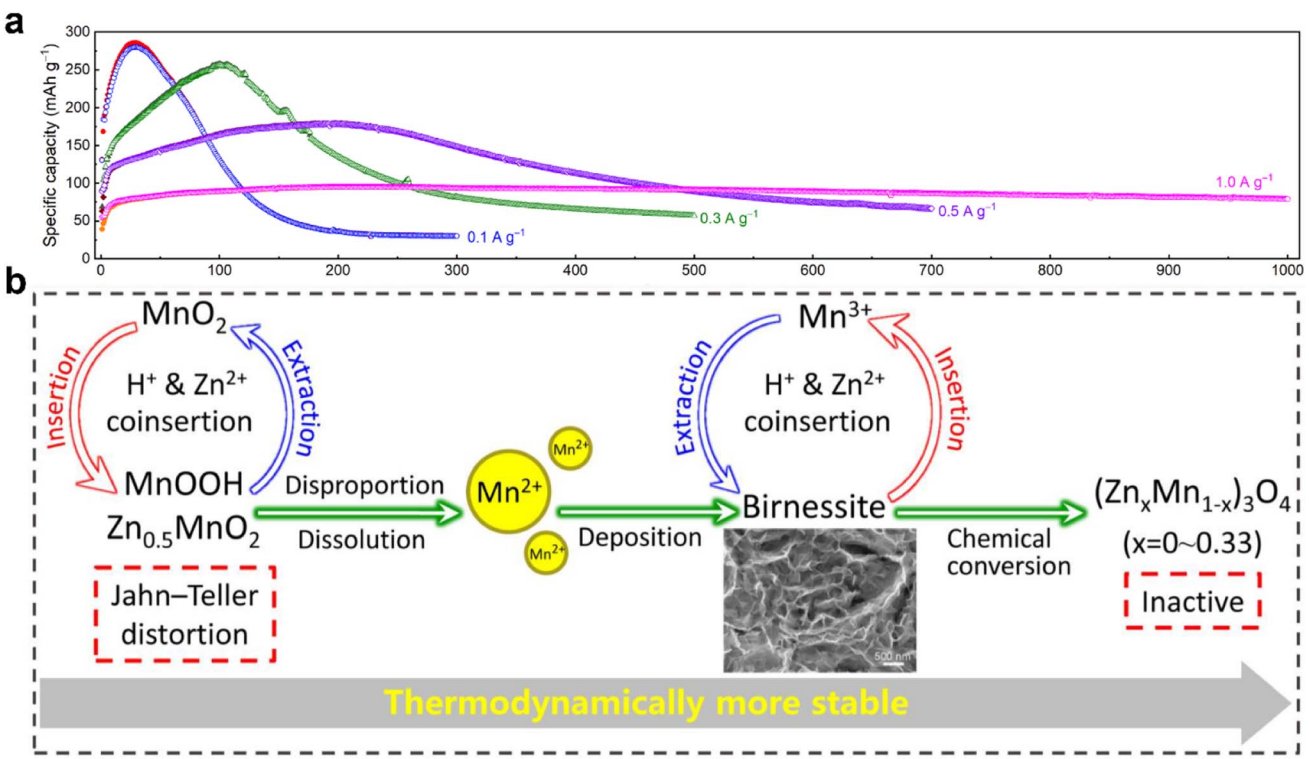

Fig. 9 Evolution of the active materials during long-term cycling. (a) Cycling performance at different specific currents of β-MnO_2 electrode. (b) Schematic illustration of the transformation process and reaction mechanism in each step of MnO_2 during long-term cycling. (a) and (b) Reproduced with permission.[56] Copyright 2022, Elsevier.

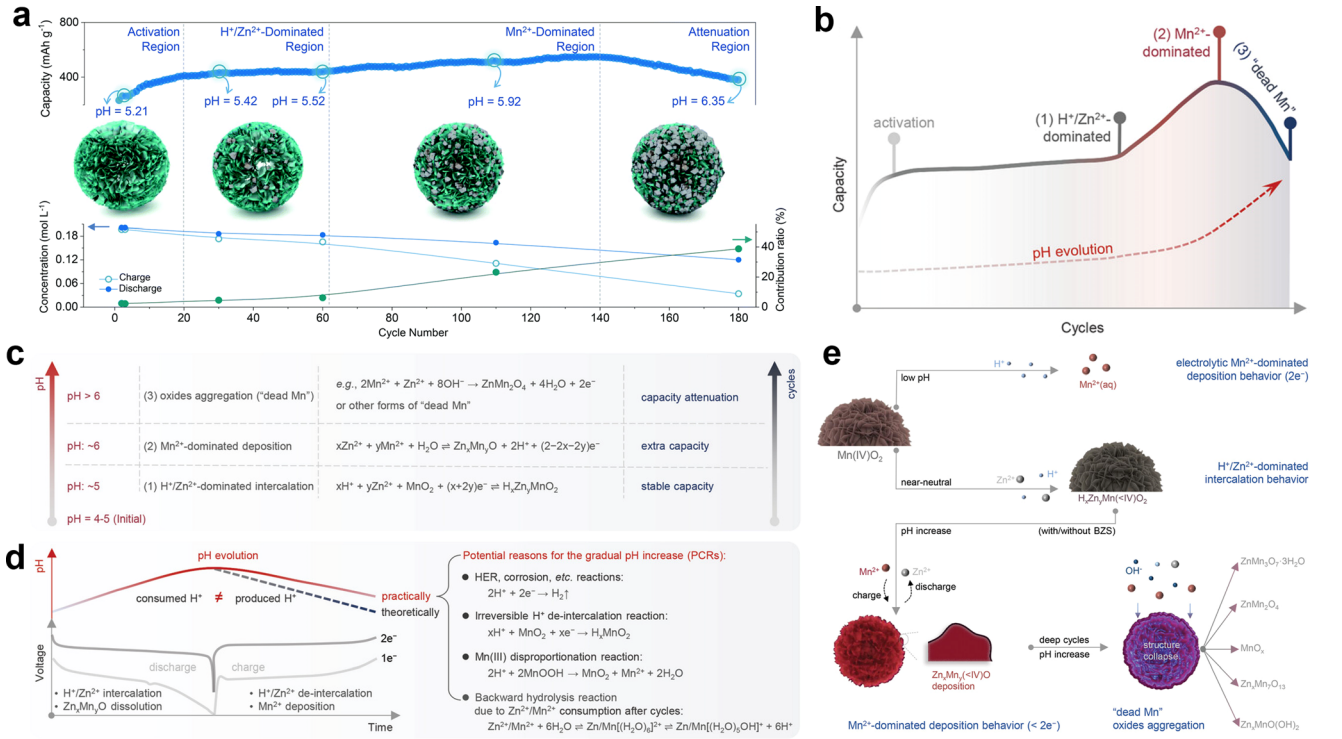

Fig. 10 Evolution of CfM and pH during long-term cycling. (a) Mn-based competitive capacity evolution protocol. Reproduced with permission.[120] Copyright 2022, The Royal Society of Chemistry. (b) Evolution of capacity and charge storage mechanisms during cycles associated with pH change. (c) Dominant reactions determined by the pH environment. (d) Summary of potential reasons for gradual pH increase. (e) Illustration of the $H^+/Zn^{2+}/Mn^{2+}$-dominated electrochemical process at different pH environments. (b)–(e) Reproduced with permission.[119] Copyright 2023, Wiley-VCH.

be significantly higher than that of Mn^{2+} during charge/discharge, with a calculated CfM value of less than 5%. This suggests that Zn^{2+} insertion/extraction plays a dominant role in the capacity contribution within region I. Therefore, the observed increase in capacity in this region can be attributed to electrode wetting. In region II, CfM slightly increases and the deposition of $ZnMn_2O_4$ is quasi-reversible due to the low pH environment. The capacity contribution mainly originates from the reversible intercalation/deintercalation of H^+/Zn^{2+}, resulting in a relatively flat cycle curve. Instead, CfM significantly increases with a rapidly decrease in the concentration of Mn^{2+} in region III, manifesting that Mn^{2+} dominates the reaction chemistry rather than H^+/Zn^{2+} insertion/extraction, leading to an obvious increase in capacity. Besides, Qiu *et al.*[123] found that properly increasing the pre-added Mn^{2+} can expand the trend of capacity increase and achieve a higher maximum capacity value. The irreversible deposition of $ZnMn_2O_4$ nanoparticles provides nucleation sites for subsequent Mn^{2+} deposition, thereby inducing the accumulation of more $ZnMn_2O_4$ nanoparticles on the electrode surface, giving rise to a fast increase in CfM. However, the abundant accumulation of $ZnMn_2O_4$ nanoparticles on the cathode surface significantly increases the resistance and restricts the ion/charge transfer between the electrolyte and inner MnO_2, causing rapid capacity fading in region IV. In brief, the different capacity contributions originating from cation insertion/extraction and Mn^{2+} conversion during long-term cycling result in a dynamic performance evolution.

4.3.3 The evolution of pH. Moreover, new insight into the pH evolution in near-neutral pH electrolytes rationally makes the underlying cause for capacity fluctuation clear (Fig. 10b and c).[119] Owing to the unavoidable occurrence of the hydrogen evolution reaction,[133] irreversible H^+ extraction reaction, Mn^{3+} disproportionation reaction and backward hydrolysis reaction,[134,135] complete restoration of the initial pH state within a single cycle becomes unattainable, giving rise to a continuous increase in pH in the whole cycle calendar (Fig. 10d). The deposition potential of Mn^{2+} is high in the initial cycles due to the relatively low pH, wherein cation intercalation reactions dominate this period and result in a relatively stable evolution curve of capacity. As the pH continues to increase, the formation of deposited manganese oxide becomes more easily triggered with the dominant process changing to Mn deposition, leading to a rapid increase in capacity. As the cycle proceeds, the dissolution of manganese oxide becomes harder due to the high pH value and the formation of abundant irreversible manganese oxide consumes a large amount of H^+, which causes a significant increase in pH, ultimately depleting the Mn^{2+} electrolyte and resulting in capacity attenuation (Fig. 10e). Consequently, the capacity fluctuation of manganese-based ZIBs with rapid increase and decay can be attributed to pH evolution in near-neutral pH electrolytes.

In summary, the mechanisms of capacity attenuation, capacity activation and dynamic capacity fluctuation in manganese-based ZIBs were comprehensively discussed. The inevitable dissolution of Mn, dramatic volume changes, and irreversible consumption of Mn^{2+} lead to capacity attenuation. Capacity activation is attributed to electrolyte Mn^{2+} electrodeposition, electrochemical oxidation and induced Mn-defects of low-valence manganese oxides during the charging process. Also, the evolution of the active materials, capacity contribution ratio from Mn^{2+}, and pH results in dynamic capacity fluctuation.

5 Strategies for improving cycling stability

Undoubtedly, the capacity fluctuation poses a significant challenge for the commercial application of manganese-based ZIBs. Although converting Mn^{2+} to manganese oxides can provide additional capacity, resulting in an increase in capacity, this "fake" high-performance is transitory and the capacity will rapidly decay due to the generation of "dead" Mn. Consequently, enhanced cycling stability can be achieved by mitigating Mn dissolution and Mn^{2+} deposition, thereby enabling the dominant capacity contribution from Zn^{2+}/H^{+} insertion/extraction. Additionally, improving the reversibility of the dissolution/deposition reaction represents an alternative approach to enhance the cycling stability. Thus, strategies aimed at optimizing the cycling stability should focus on either promoting one-electron transfer in the $Mn^{4+} \leftrightarrow Mn^{3+}$ reaction or facilitating two-electron transfer in the $Mn^{4+} \leftrightarrow Mn^{2+}$ reaction.

5.1 Strategies based on one-electron transfer reaction

5.1.1 Rational composite design. Rationally compositing conductive materials or transition metal oxides not only significantly enhances the electronic conductivity and ionic diffusion efficiency of semi-conductive manganese-based materials, but importantly improves their structural stability and mitigates side reactions during cycling. The enhanced structural stability primarily originates from the synergistic effects generated by two stable interfaces (the interface between the outer component and electrolyte, as well as the interface between components) through chemical bonding or physical isolation.

The multilayered rGO coated on MnO_2 nanowires with a thickness of 5 nm, as reported by Mai *et al.*,[136] was found to effectively alleviate direct contact between the internal active MnO_2 and the electrolyte. In pure $ZnSO_4$ electrolyte, it was observed that the concentration of Mn^{2+} significantly decreased during the discharge process after rGO coating, indicating the effective inhibition of the Mn dissolution issue. Additionally, the coating of polypyrrole (PPy) on MnO_2 also proved to suppress Mn dissolution, where PPy not only serves as a protective layer but also forms an Mn–N bond at the interface between MnO_2 and PPy (Fig. 11a), resulting in cycle performance of 500 cycles without capacity fading.[113] Recently, Zhu *et al.* successfully fabricated a hydrophobic and uniform aminopropyl phosphonic acid (AEPA) coating layer with a few nanometer thickness on the surface of MnO_2. It was found that AEPA can form strong chemical bonds with MnO_2, effectively inhibiting the dissolution of Mn by creating a barrier between the electrolyte and cathode.[137] Yolk–shell structured K-birnessite@mesoporous carbon nanospheres (KMOH@C) with abundant void space between the KMOH core and carbon shell were synthesized by Zhai *et al.*[138] The mass of internal voids between the KMOH core and the carbon skeleton could efficiently restrain the volume changes, aggregation, and further pulverization of the KMOH nanosheets during the charging/discharging (Fig. 11b).[116] As a result, KMOH@C showed excellent long-term cycle stability over 6000 cycles at 3 A g^{-1}. Also, graphite nanosheets, which possess superior mechanical properties, were demonstrated to enhance the stress of MnO_2 and suppress the further expansion and extrusion during the phase change process (Fig. 11c).

$ZnMn_2O_4$ quantum dots (ZMO QD@C) were synthesized within a porous carbon framework through *in situ* electrochemically inducing Mn-MIL-100-derived Mn_3O_4 quantum dots and carbon composite, as reported by Niu *et al.*[139] In comparison to ZMO-bulk, the presence of a new peak at 1025 cm^{-1} for ZMO QD@C is attributed to the formation of Mn–O–C bonds. The XPS spectra further confirmed the existence of Mn–O–C bonds, with new peaks observed at 531.9 eV for O 1s and 286.3 eV for C 1s in ZMO QD@C, respectively. Moreover, the analysis of the Mn valence states revealed that Mn predominantly exists as Mn(IV) at the interface between ZMO QDs and the carbon matrix, while being present as Mn(III) within the interior of ZMO QDs (Fig. 11d). The formation of stable Mn–O–C bonds at the interface effectively mitigates the disproportionation reactions and dissolution processes occurring on the surface of ZMO QDs (Fig. 11e). In addition, the establishment of a stable interface can also prevent direct contact between the electrolyte and the interior ZMO, thereby suppressing the dissolution of Mn^{3+} within the interior of ZMO QDs during discharge. Consequently, even in pure $ZnSO_4$ electrolyte, a super stable cycling performance can be realized (Fig. 11f). Additionally, it has been reported that the formation of an Mn–O–Ce bond in the MnO_2@CeO_2 composite can also ameliorate the disproportionation reaction and enhance the cycling stability.[140] Compositing with 2D layered MXenes not only enhances the charge transfer kinetics, but also mitigates issues such as volume expansion/contraction, structure dissolution, and side reactions of MnO_2.[141–145] For example, Yan *et al.*[141] demonstrated that the incorporation of 3D $Ti_3C_2T_x$@MnO_2 microflowers with superior structural integrity resulted in good cycle stability with capacity retention of 90.6% over 2000 cycles at 0.5 A g^{-1}, which is much better than pure MnO_2 with a capacity retention only 21.4%. Hetero-structured Mn_2O_3–$ZnMn_2O_4$ hollow octahedrons with superior structural stability were designed *via* a two-step metal–organic framework template strategy.[146] The synergistic effects of the distinct composition and hollow heterostructure induced very stable Zn^{2+} storage, and the unique hollow octahedral structure could be well maintained even after 2000 cycles (Fig. 11g).

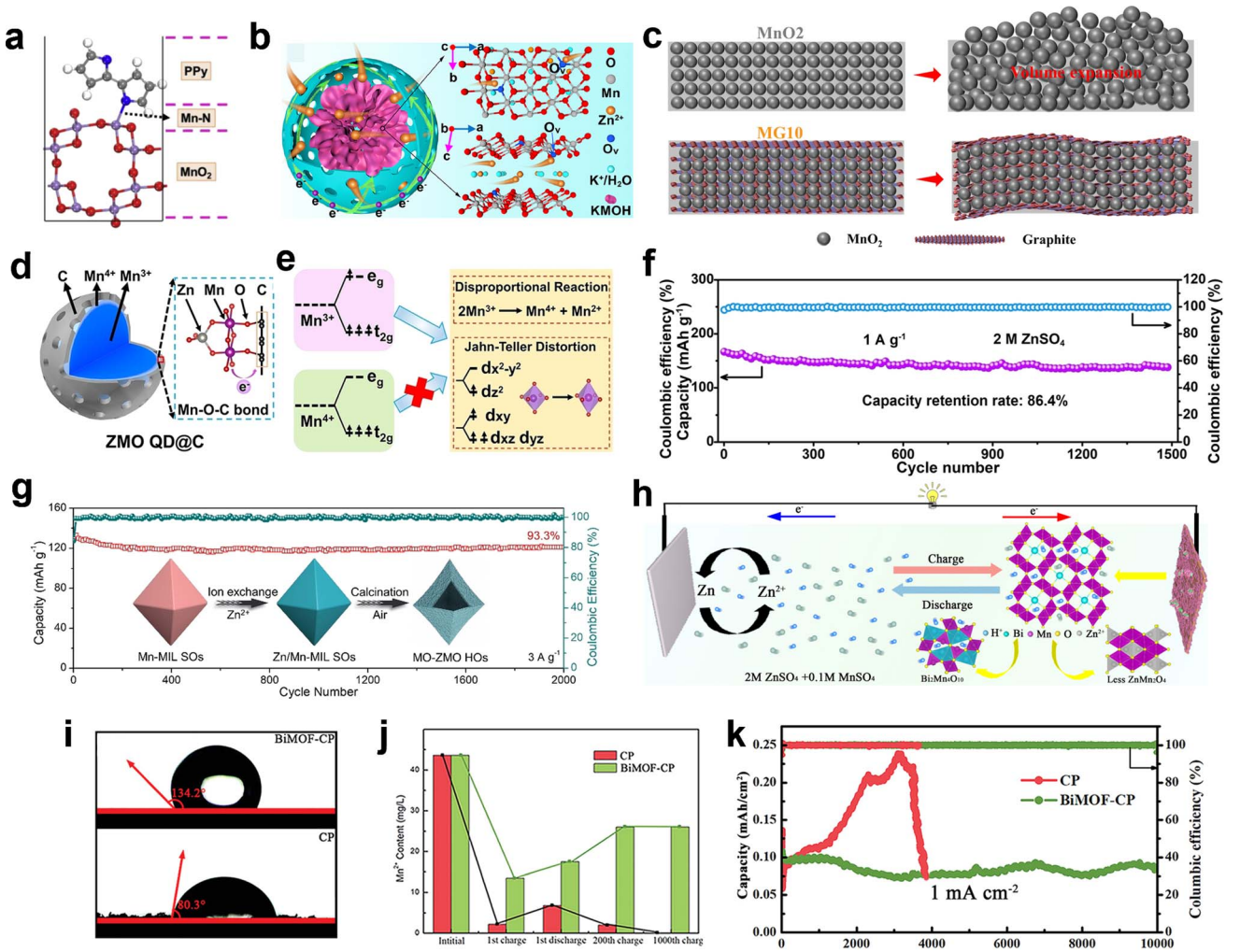

Fig. 11 Strategy for rational composite design based on one-electron transfer reaction. (a) Optimal configuration of the disordered MnO_2 surface covered by PPy. Reproduced with permission.[113] Copyright 2020, Elsevier. (b) Schematic illustration of the Zn-ion/electron transport in KMOH@C with oxygen vacancies. Reproduced with permission.[138] Copyright 2021, Elsevier. (c) Schematic illustration of the volume change in MnO_2 and MnO_2/graphite. Reproduced with permission.[116] Copyright 2020, Elsevier. (d) Illustration of the Mn valence state distribution in ZMO QD@C. (e) Mechanism for the structural stability of ZMO QD@C. (f) Long-term cycle test. (d)–(f) Reproduced with permission.[139] Copyright 2022, Wiley-VCH. (g) Cycling performance of hetero-structured Mn_2O_3–$ZnMn_2O_4$ hollow octahedrons. Reproduced with permission.[146] Copyright 2021, Wiley-VCH. (h) Schematic diagram showing the effects of bismuth in manganese-based ZIBs. Reproduced with permission.[147] Copyright 2021, the American Chemical Society. (i) Contact angle tests of BiMOF-CP and CP samples. (j) Element analysis of deposited Mn^{2+} in 2 M $ZnSO_4$/0.2 M $MnSO_4$ aqueous electrolyte during cycling of BiMOF-CP and CP. (k) Cycling performance of BiMOF-CP and CP. (i)–(k) Reproduced with permission.[148] Copyright 2023, Wiley-VCH.

Gou *et al.*[147] demonstrated that the MnO_2–Bi_2O_3 composite undergoes a competitive reaction during the cycling process, resulting in the formation of $Bi_2Mn_4O_{10}$ instead of electrochemically inactive $ZnMn_2O_4$ due to its lower formation energy, as shown in eqn (42) and (43). This leads to improved cycling performance (Fig. 11h). Thus, to avoid Mn^{2+} electrodeposition and its further transformation to electrochemically inactive λ-$ZnMn_2O_4$, a kinetic inhibition strategy was employed by incorporating graphite nanosheets with limited surface defects in MnO_2 electrodes. The hydrophobicity and smooth surface of the graphite nanosheets effectively suppressed the rate-determining Mn^{2+} adsorption during nucleation, thereby ensuring a long-term cycling performance even at a high depth of discharge.[102]

$$Bi_2O_3 + 6H^+ \rightarrow 2Bi^{3+} + 3H_2O \quad (42)$$

$$2Bi^{3+} + 4MnO_2 + 2H_2O + 2e^- \rightarrow Bi_2Mn_4O_{10} + 4H^+ \quad (43)$$

Instead of blocking Mn^{2+} deposition, pyridine-3,5-dicarboxylate (Bi-PYDC) with a specific poorly hydrophilic and manganophilic nature (Fig. 11i), was reported to regulate the Mn^{2+} deposition reaction in cathode-free ZIBs.[148] As depicted in Fig. 11j, the concentration of Mn^{2+} rapidly decreased after the first cycle in the Zn/CP system. The fast deposition rate of CP induced the rapid generation of MnO_2 and inert phase, resulting in an unstable cycling performance. In contrast, the Zn/Bi-PYDC system maintained a relatively high and steady Mn^{2+} concentration due the fewer nucleation sites for Mn^{2+}

deposition. This indicates a moderate deposition rate of Mn^{2+} for Bi-PYDC, which effectively prevented the excessive depletion of Mn^{2+} in the electrolyte and maintained an equilibrium reaction between dissolution and deposition. Moreover, a certain amount of Mn^{2+} in the electrolyte could effectively suppress the disproportionation reaction of deposited MnO_2. Consequently, the cathode-free ZIBs showed outstanding long-term cycling stability over 10 000 cycles at 1 mA cm^{-2} (Fig. 11k).

5.1.2 Pre-intercalation. The pre-intercalation of crystal water, ions, and organic species in manganese-based materials is an effective strategy for reinforcing the inherent structural stability. These intercalated guest species can form chemical bonds with basic polyhedron or act as pillars to stabilize the host framework. For example, Liang and coworkers claimed that K^+ pre-intercalated in the [2 × 2] tunnels of α-MnO_2 enables the formation of K–O bonds with MnO_6 octahedra,[149] which can stabilize the host framework and suppress the manganese dissolution to a great extent during cycling (Fig. 12a and b). Through atomic imaging, Yuan *et al.*[150] directly observed that Co^{2+} was intercalated in the tunnel space of α-MnO_2 [2 × 2] (Fig. 12c). The low binding energy (−6.62 eV) exhibited by Co^{2+} intercalated in tunnel MnO_2 implies the possibility of the formation a Co–O bond between Co^{2+} and the surrounding O atoms, thereby enhancing the inherent stability of the Mn–O octahedron and effectively inhibiting the dissolution of Mn (Fig. 12d). The formation of metal–O bonds was further confirmed by pre-intercalated Al^{3+} in α-MnO_2.[151] *In situ* Raman spectroscopy revealed a highly reversible phase transformation

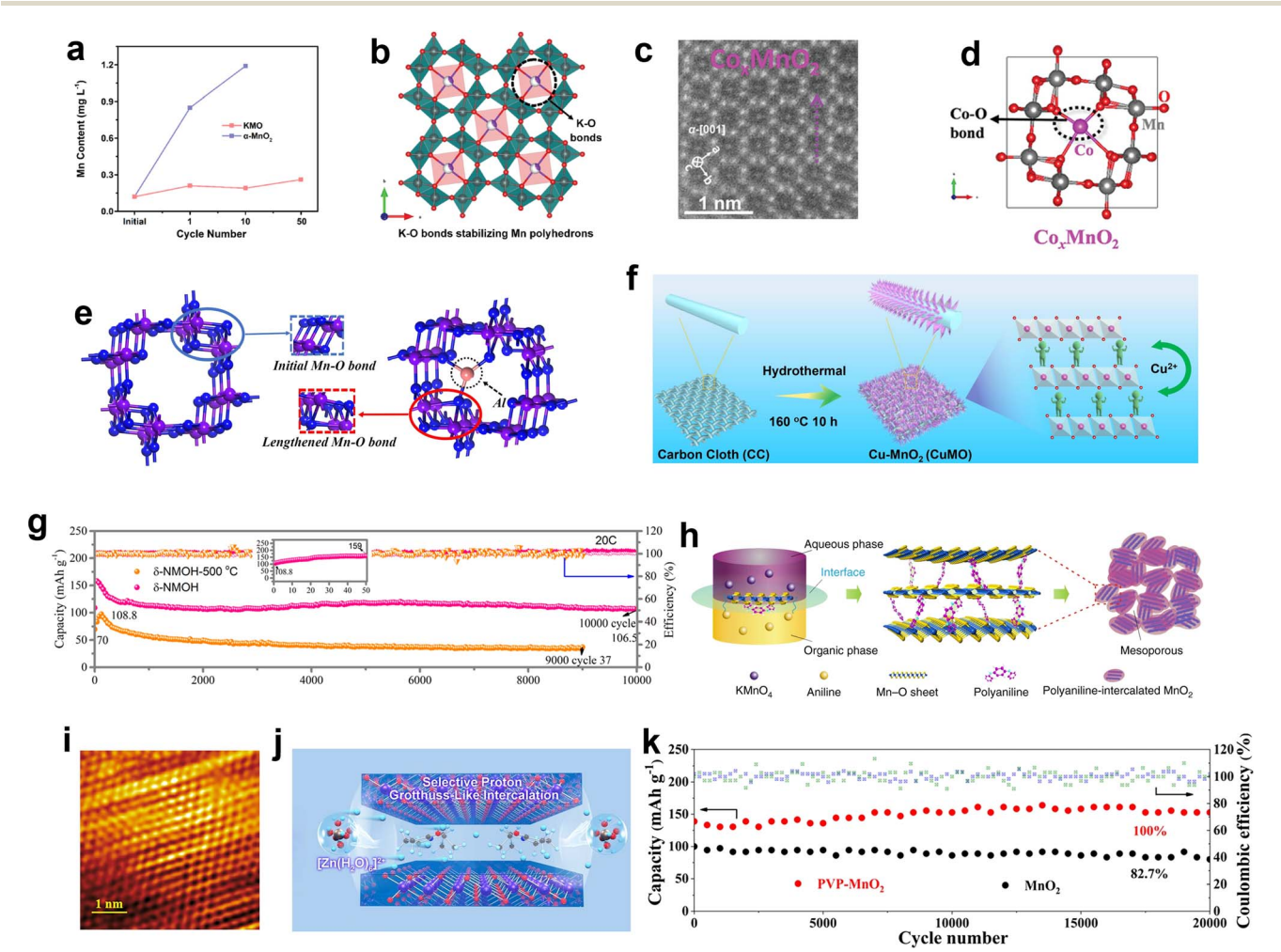

Fig. 12 Strategy for pre-intercalation based on one-electron transfer reaction. (a) Element analysis of dissolved Mn^{2+} in 2 M $ZnSO_4$ aqueous electrolyte during cycling of KMO and α-MnO_2. (b) Schematic of the incorporation of K^+ ions stabilizing the Mn polyhedrons. (a) and (b) Reproduced with permission.[149] Copyright 2019, Wiley-VCH. (c) [001] down-tunnel imaging showing the atomic structure of α-MnO_2 with Co^{2+} and K^+ occupying the tunnel center position. (d) Schematic of the incorporation of Co^{2+} ions stabilizing the Mn polyhedrons. (c) and (d) Reproduced with permission.[150] Copyright 2023, Wiley-VCH. (e) Structure diagrams of pristine MnO_2 and Al-intercalated MnO_2. Reproduced with permission.[151] Copyright 2021, Elsevier. (f) Schematic illustration of the synthetic process of Cu-intercalated MnO_2 electrode. Reproduced with permission.[152] Copyright 2022, Elsevier. (g) Long-term cycling stability of Zn-δ-NMOH battery and Zn-δ-NMOH-500 battery. Reproduced with permission.[154] Copyright 2019, the American Chemical Society. (h) Schematic illustration of PANI-intercalated MnO_2 nanolayers. Reproduced with permission.[155] Copyright 2018, Springer Nature. (i) HAADF-STEM images of and PVP–MnO_2. (j) Selective proton Grotthuss intercalation of interlayer configuration optimization. (k) Cycling stability of PVP–MnO_2. (i)–(k) Reproduced with permission.[156] Copyright 2023, Wiley-VCH.

between α-MnO_2 and layered birnessite, and the peak located at 280 cm^{-1} is attributed to Al–O bonds. Despite the phase transition inducing α-MnO_2 to form layered birnessite during discharge, the signal of Al–O bonds persisted, indicating that the consistent presence of Al–O bonds not only stabilized the tunnel structure of α-MnO_2 but also alleviated the structural deformation and dissolution of the layered birnessite (Fig. 12e).

The application of the pre-intercalation strategy in δ-MnO_2 is considered promising due to its much larger interlamellar spacing (about 0.7 nm) compared to tunnel-type MnO_2. Cu^{2+} intercalation in δ-MnO_2 was reported by Zhang *et al.* (Fig. 12f).[152] DFT calculations indicated that the pre-intercalation of Cu^{2+} can effectively enhance the structural stability of δ-MnO_2, which is attributed to the strong ionic bonds with oxygen atoms. The pre-intercalation of alkali ions play an important role in reinforcing the structural stability of δ-MnO_2, where Na^+ or K^+ acts as pillars stabilizing the layered structures. This led to a minimal loss capacity of 3% between the 20th and 100th cycles at 1/3C, and long cycling stability with 90% retention after 1000 cycles at 10C for the $K_{0.27}MnO_2 \cdot 0.54H_2O$ cathode, as reported by Simon *et al.*[153]

The effect of crystal water on manganese-based materials cannot be neglected, where the critical role of crystal water in layered MnO_2 was explored in SIBs previously.[157,158] It was found that crystal water not only acts as interlayer pillars through hydrogen bonding with the MnO_6 layers to suppresses Mn dissolution, but also exhibits a charge shielding effect that mitigates the strong electrostatic interactions between the cations and the host framework, thereby enhancing the ion diffusion kinetics. As reported by Zhi *et al.*,[154] Na^+ and crystal water pre-intercalated in the δ-MnO_2 interlayer space (δ-NMOH), which acted as pillars to stabilize the layered structures. Benefitting from Na^+ and crystal water pre-intercalation, δ-NMOH showed an ultra-high capacity retention of 98% and well-retained layered structures over 10 000 cycles. However, when δ-NMOH was thermally treated at 500 °C to remove the crystal water, it showed a poor electrochemical performance compared with δ-NMOH due to the loss of a lubricant effect for cation insertion/extraction and the insufficient remaining Na^+ ions to stabilize the host structure (Fig. 12g). Lou *et al.*[159] devised a method to pre-intercalate ammonium ions in layered δ-MnO_2 through an ion–exchange reaction between K^+ ions and ammonium ions. These intercalated ammonium ions act as interlayer pillars, expanding the lattice spacing of δ-MnO_2 and forming stable hydrogen-bond networks, thereby alleviating the Jahn–Teller effect and demonstrating superior cycling stability over 10 000 cycles. Interestingly, anions were also reported to intercalate in MnO_2 for enhanced cycle performance. For example, Zhang *et al.*[160] successfully introduced PO_4^{3-} in the MnO_2 layer with rich oxygen defects *via* a simple phosphorization process.

Besides ions and crystal water, polymers have also been introduced as stabilizers for δ-MnO_2. A one-step inorganic/organic interface reaction was utilized to synthesize polyaniline-intercalated δ-MnO_2 (Fig. 12h), which was proven to be effective in preventing an irreversible phase transformation and structure collapse of δ-MnO_2 during the repeated hydrated Zn^{2+}/H^+ intercalation/de-intercalation process, leading to a stable cycle performance even at a low current of 0.2 A g^{-1}.[155] In addition, it was reported that pre-intercalated poly(3,4-ethylenedioxythiophene) (PEDOT) with an enlarged interlayer spacing acts as a structural pillar, which is beneficial to stabilize the layered structure of MnO_2.[161] Recently, polyvinylpyrrolidone (PVP) pre-intercalation in MnO_2 (PVP–MnO_2) with a hybrid superlattice was reported by Bai *et al.* (Fig. 12i).[156] PVP–MnO_2 exhibited preferential H^+ Grotthuss intercalation behavior and effectively mitigated structural collapse by impeding the transport of $[Zn(H_2O)_6]^{2+}$ ions due to their larger radius and stronger coulombic interaction with the host material (Fig. 12j). Consequently, this resulted in outstanding cycle stability with nearly 100% capacity retention over 20 000 cycles at 10 A g^{-1} (Fig. 12k).

5.1.3 Heteroatom doping. Heteroatom doping is considered an effective strategy for regulating the chemical nature and geometrical configuration of manganese-based materials. On the one hand, the incorporation of heteroatoms not only facilitates ion transfer but also modifies the electronic structure to enhance the conductivity, ultimately improving the reaction kinetics and electrochemical performance. On the other hand, heteroatom doping can modulate the strength of Mn–O bonds or form chemical bonds with Mn atoms to enhance the crystal structure stability.[162,163]

Metal ion doping has been commonly employed to improve the cycling stability of manganese-based ZIBs. Also, various metal ions have been demonstrated as available dopants. For instance, it was reported that the substitution of Ti and the resulting oxygen vacancy can create a charge depletion zone, leading to the formation of a built-in electric field. The presence of oxygen vacancy can modify the internal electric field and improve the electrostatic stability by compensating for the nonzero dipole moment.[170] As a result, this leads to a significantly reduced charge-transfer impedance and diffusion rate for both Zn^{2+} and H^+, facilitating their intercalation within the MnO_2 tunnel structure, and ultimately contributing to an outstanding long-term cycling performance.[171] The incorporation of Ni^{2+} in Mn_2O_3 was demonstrated to reduce the formation energy of the Mn–O bond (Fig. 13a), which could effectively stabilize the Mn–O bond and alleviate the dissolution of manganese.[164] This resulted in a remarkable capacity retention of 85.6% over 2500 cycles at 1 A g^{-1} for Ni-doped Mn_2O_3. Multivalent cobalt-doped Mn_3O_4 was successfully synthesized by Wang *et al.*,[165] wherein the doped Co exhibited various valence states and played multiple roles. Specifically, Co^{2+} acts as a "structural pillar" to stabilize the framework of the phase change product δ-MnO_2, while the Co^{4+} in the layer enhances the conductivity of Mn^{4+} and contributes to its high specific capacity. Importantly, doping with Co^{2+} and Co^{3+} can effectively suppress the Jahn–Teller distortion and facilitate ion diffusion (Fig. 13b). The doping of high-valent Mo^{6+} has been reported to result in an elevated oxidation state of Mn and a reduction in oxygen defects, thereby enhancing the structural stability and inhibiting the Jahn–Teller effect during discharge/charge processes.[172] Analogously, the substitution of Fe^{3+} at the Mn site can alleviate the collapse of the MnO_2 crystal structure

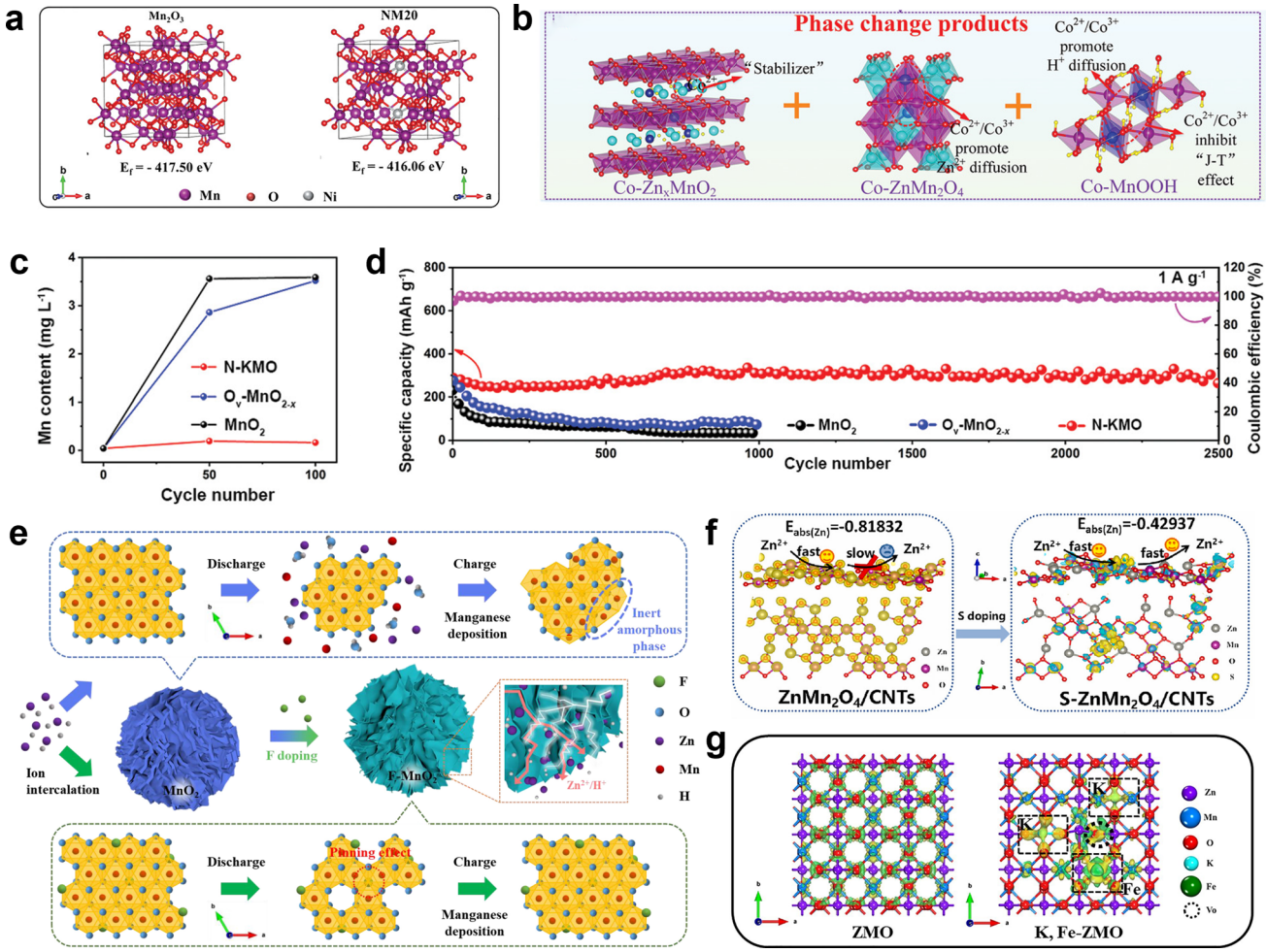

Fig. 13 Strategy for heteroatom doping based on one-electron transfer reaction. (a) Calculated formation energy (in eV) of Mn_2O_3 and Ni-doped Mn_2O_3. Reproduced with permission.[164] Copyright 2021, Wiley-VCH. (b) Effect of various Co ions in phase change product. Reproduced with permission.[165] Copyright 2020, Wiley-VCH. (c) Mass content of dissolved Mn element in 2 M $ZnSO_4$ aqueous electrolyte during cycling. (d) Cycling performance of N-KMO at a current density of 1 A g^{-1}. (c) and (d) Reproduced with permission.[166] Copyright 2022, Wiley-VCH. (e) Schematic diagram of enhanced reaction feasibility of F-MnO_2. Reproduced with permission.[167] Copyright 2021, Elsevier. (f) Charge density difference distribution diagrams of ZMO and S-ZMO. Reproduced with permission.[168] Copyright 2023, Elsevier. (g) Electron density difference of K, Fe-ZMO and ZMO. Reproduced with permission.[169] Copyright 2022, Elsevier.

caused by Jahn–Teller distortion due to the increase in the mean valence of manganese.[173]

Nonmetal element doping is also important for enhancing the cycling stability of manganese-based ZIBs. For example, Lou *et al.*[166] constructed N-doped KMn_8O_{16} (N-KMO) with abundant oxygen vacancies and large specific surface area. It was found that N-doping effectively inhibited the dissolution of Mn^{2+} caused by the Jahn–Teller distortion, as confirmed by the ICP results (Fig. 13c), thereby resulting in an impressive capacity retention of 91% over 2500 cycles (Fig. 13d). Moreover, the introduction of N-doping facilitated the formation of Mn–N bonds, thereby promoting interfacial dynamics in manganese-based materials and effectively mitigating manganese dissolution to ensure structural integrity.[174,175] In addition, N-doped $ZnMn_2O_4$ (N-ZMO) is conductive to the release of electrostatic forces caused by charge changes. The reduced electrostatic forces during Zn^{2+} insertion alleviate the volume expansion and structural collapse of N-ZMO.[176] Owing to the extremely high electronegativity and electron absorption of fluorine, the fluorine doping can promote robust bonding with the surrounding atoms. The dispersed doped fluorine in F-MnO_2 acts as a pin to anchor the lattice framework, preventing the excessive dissolution of the manganese-based framework in the discharge process. Although the partially dissolved manganese leads to Mn vacancy in the lattice, the "pinning effect" of fluorine protects against lattice collapse. During the charging process with manganese deposition, Mn^{2+} preferentially deposits into metastable coordination environments associated with Mn vacancy defects, thus facilitating the restoration of the original crystal structure (Fig. 13e).[167] The sulfur-doping proposed by Zhao *et al.* aimed to enhance the structural stability of MnO_2. This improvement was attributed to the substitution of the S anions, which have lower electronegativity than the O anions in the crystal structure. Consequently, this substitution reduced

the diffusion barrier for Zn^{2+} ions across the cathode and prevented the formation of thermodynamically stable $ZnMn_2O_4$.[177] Additionally, Yang *et al.*[168] demonstrated that S-doping could effectively modulate the electrical structure of $ZnMn_2O_4$ by inducing the non-uniform distribution of charge distribution. The accumulation of electrons near the Mn atom signifies strong interactions between Mn and O (Mn–O) as well as between Mn and S (Mn–S) (Fig. 13f), thereby improving the structural stability of $ZnMn_2O_4$.

Dual heteroatom doping with distinct functionalities represents a novel approach to achieve a stable cycling performance in manganese-based ZIBs.[169,178] For example, Shao *et al.*[169] reported the preparation of K, Fe co-doped $ZnMn_2O_4$ (K, Fe-ZMO) as a cathode for stable ZIBs. In the structure of K, Fe-ZMO, K occupies partial Zn sites, while Fe occupies partial Mn sites. The dual doping strategy promotes strong interactions between the Fe atoms and O atoms as well as the Mn atoms and O atoms (Fig. 13g). Meanwhile, the lower formation energy of K, Fe-ZMO ensures structural stability and low manganese dissolution. However, it is important to note that the performance of batteries is intricately linked to both the doping sites and content of dopants. Not all forms of doping are beneficial; in fact, some can be detrimental. By employing controllable favorable heteroatom doping, significant enhancements in intrinsic reaction kinetics can be achieved, resulting in an increase in capacity and energy power density, as well as improved cycling life.[179]

5.2 Strategies based on two-electron transfer reaction

The two-electron transfer reaction can eliminate the shortcomings associated with the insertion mechanism, such as detrimental Mn dissolution, dramatic volume changes and complex phase transformation. Furthermore, batteries employing the deposition/dissolution mechanism exhibit enhanced capacity compared to those based on the insertion mechanism. However, achieving a stable cycling performance in manganese-based ZIBs using the deposition/dissolution mechanism still faces challenges due to the insufficient Mn^{2+} absorption sites and competing reactions of Mn^{2+}/Mn^{3+} during charging, as well as the incomplete dissolution of MnO_2 caused by its low electrical conductivity. The strategies for improving the reversibility of two-electron transfer reaction are discussed in the following sections.

5.2.1 Rational composite design. A porous carbon matrix-encapsulated MnO (MnO@PC) nanocomposite demonstrated the enhanced dissolution of MnO. The hierarchical meso-microporous carbon matrix possesses a large specific surface area, facilitating electrolyte infiltration and providing a negatively charged surface, which promotes the adsorption of cations. This enables better utilization of Zn^{2+} and Mn^{2+} in the electrolyte for ZSH deposition and the reversible deposition/dissolution process of $Zn_xMnO(OH)_2$.[130] The composite of negatively charged Zn–Mn MOF-derived porous carbon and MnO (MnO/MZ) exhibited strong adsorption of Mn^{2+} owing to the strong electrostatic interactions between the negatively charged MnO/MZ and positively charged Mn^{2+}, which significantly promoted the dissolution/deposition reaction of Mn^{2+}/MnO_2. As depicted in Fig. 14a, compared to MnO_2, Super P, and monometallic Mn-MOF-derived MnO/M, MnO/MZ demonstrated the highest negatively charged zeta potential in the same mild pH environment. Moreover, the similarly lower zeta potentials observed for Super P and MnO/M suggest that Zn plays a crucial role in generating negative charge, which is possibly attributed to the vaporization of positively charged Zn during calcination. The ICP results further confirmed the superior Mn^{2+} absorption ability of MnO/MZ (Fig. 14b), leading to a significant decrease in Mn^{2+} concentration after soaking in $MnSO_4$ solution. Despite the continuous dissolution of MnO during cycling, the dissolved Mn^{2+} can effectively undergo electro-oxidation and back deposition to form MnO_2, resulting in performance activation. Once all the MnO is completely dissolved, the highly reversible reaction between MnO_2 and Mn^{2+} dominates the capacity contribution, thereby ensuring excellent cycling stability over 11 000 cycles.[132]

Liu and colleagues found that both the dissolution of MnO_2 and back-deposition of Mn^{2+} can be facilitated by compositing with MoO_3.[180] After introducing MoO_3, the Mn–O bond strength was weakened, leading to the formation of more oxygen vacancies by reacting with the oxygen atoms in MnO_2. In addition, compared to pure MnO_2, MnO_2/MoO_3 possessed more structural water during the whole discharge process, which resulted from the proton interactions with the lattice oxygen and the lower energy barrier for Mn release, as confirmed by the DFT results (Fig. 14d). Therefore, the inherent structural stability of MnO_2 was weakened and the Mn release and dissolution process were promoted. Moreover, MnO_2/MoO_3 exhibited a negative charge potential, while MnO_2 possessed a very high positive charge potential (Fig. 14c). This indicates that MnO_2/MoO_3 is beneficial to attract Mn^{2+} for deposition. Consequently, due to the high reversibility of the dissolution and deposition reaction, MnO_2/MoO_3 demonstrated a stable cycling performance with 92.6% capacity retention over 300 cycles at 0.1 A g^{-1} and 80.1% capacity retention over 16 000 cycles at 1 A g^{-1} in pure $ZnSO_4$ electrolyte (Fig. 14e). Besides, organic molecules were demonstrated to improve the reversibility of the dissolution/deposition reaction. For instance, poly(1,5-diaminoanthraquinone) (PDAAQ) plays a key role on the regulation of the Mn^{2+} concentration, which induced a long-term cycling life exceeding 2000 cycles.[181]

5.2.2 Electrolyte regulation. A strongly acidic environment undoubtedly promotes the MnO_2/Mn^{2+} reaction according to the Nernst equation; however, it severely corrodes the Zn metal anode. $Zn(CH_3COO)_2$ is a typical near-neutral electrolyte, which can alleviate the corrosion issues and enhance the coulombic efficiency for Zn plating/stripping. During the discharge process, the protonation of the O atoms on the cathode surface leads to the formation of OH* intermediates, and the continuous reactions between OH* and proton induce the formation and desorption of H_2O, resulting in cathode dissolution. Due to the high polarizability and high electronegativity of the CH_3COO^- groups, they strongly adsorb on the surface Mn sites,[182,183] effectively weakening the binding of H_2O on MnO_2 and reducing the barriers for MnO_2 dissolution. The highly

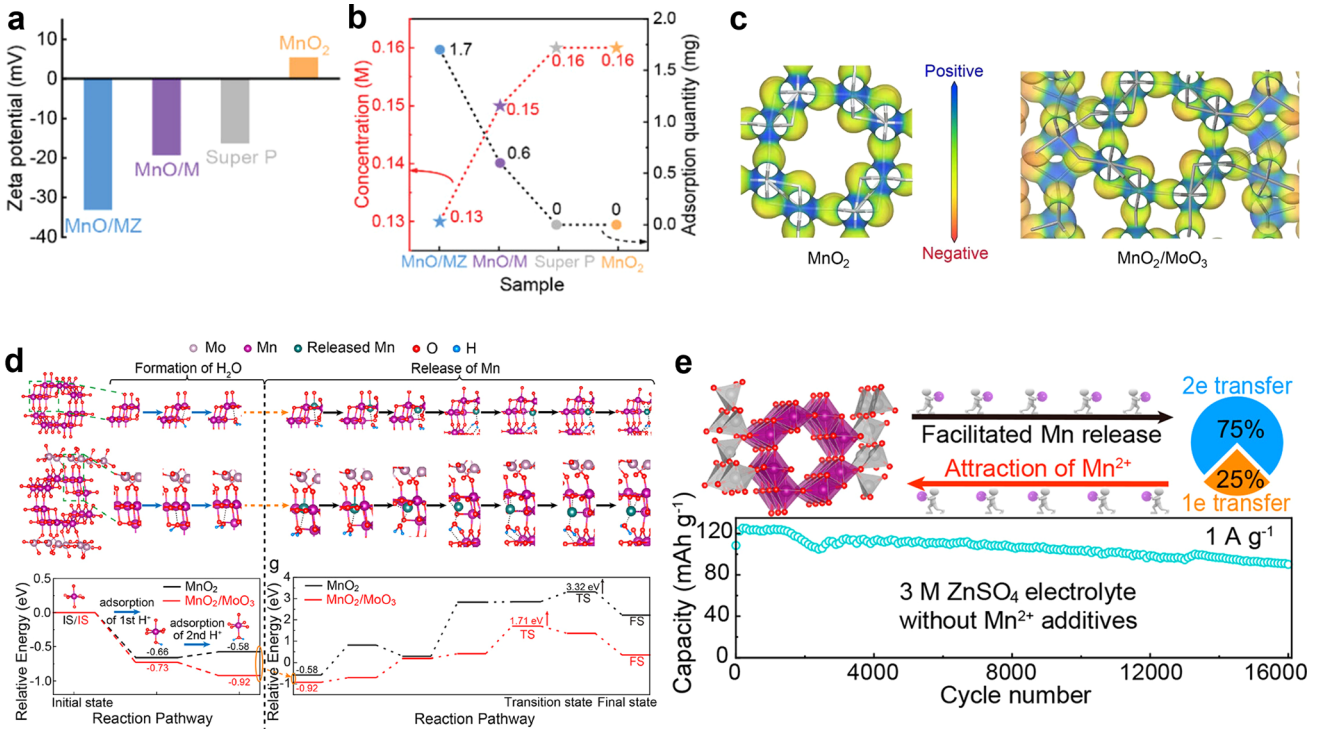

Fig. 14 Strategy for rational composite design based on two-electron transfer reaction. (a) Zeta potentials of MnO/MZ, MnO/M, Super P carbon, and MnO_2. (b) Adsorption of Mn^{2+} by MnO/MZ, MnO/M, Super P carbon, and MnO_2. (a) and (b) Reproduced with permission.[132] Copyright 2022, Wiley-VCH. (c) MESP distributions of MnO_2 and MnO_2/MoO_3. (d) DFT calculations on the formation of structural water (left) and release of Mn (right) and their relative energy diagrams. (e) Schematic illustration and long-term cycling of MnO_2/MoO_3. (c)–(e) Reproduced with permission.[180] Copyright 2023, the American Chemical Society.

reversible Mn^{4+}/Mn^{2+} redox reaction not only increased the working potential (Fig. 15a–c), but also ensured long-term cycling stability over 4000 cycles with a high capacity of 556 mA h g^{-1}.[184] The promotion of the dissolution/deposition reaction chemistry by acetate ions was also confirmed by Zhong *et al.*[185] The co-deposition of $Zn(H_2PO_4)_2$ with MnO_2 at the cathode was demonstrated to function as a local proton reservoir, facilitating the dissolution of MnO_2, as reported by Liu *et al.*[186] During the discharge, $Zn(H_2PO_4)_2$ deprotonates to form $Zn_3(PO_4)_2$ and provides protons to promote the MnO_2/Mn^{2+} dissolution reaction. During the charge process, $Zn_3(PO_4)_2$ is reversibly protonated to $Zn(H_2PO_4)_2$, restoring protons at the cathode (Fig. 15d), as indicated by eqn (44) and (45). Therefore, a high discharge voltage of 1.75 V was achieved with an enhanced reversible two-electron transfer reaction (Fig. 15e), as well as alleviating the corrosion of the Zn anode. In addition, pH buffer is ideal to achieve highly reversible MnO_2/Mn^{2+} reaction in mild aqueous electrolyte, as demonstrated by Balland *et al.*[187]

$$MnO_2 + 4H^+ + 2e^- \rightleftharpoons Mn^{2+} + 2H_2O \quad (44)$$

$$Zn(H_2PO_4)_2 + 2Zn^{2+} + 4H_2O \rightleftharpoons Zn_3(PO_4)_2 \cdot 4H_2O + 4H^+ \quad (45)$$

The inevitable co-deposition of Zn^{2+} and Mn^{2+} to form an irreversible ZMO product will lead to poor cycling stability in manganese-based ZIBs. Through the modulation of the Zn^{2+}-solvation shell to reduce the Zn^{2+} deposition at the interface, the reversibility of the dissolution/deposition reaction can be improved. For example, Hu *et al.*[188] constructed a quasi-eutectic electrolyte composed of 2 M $Zn(OTf)_2$ + 4 M urea + 0.25 M $MnSO_4$. It was found that the binding energy of the Mn^{2+}-solvation shell with urea was very weak, while the binding energy of the Zn^{2+}-solvation shell was strong. The significant difference in the Mn^{2+}/Zn^{2+} ionic solvation structure led to different mass transfer between Zn^{2+} and Mn^{2+} at the cathode interface (Fig. 15f). The high desolvation energy of Zn^{2+} makes Zn^{2+} co-deposition with Mn^{2+} at the cathode interface difficult, thereby restricting the mass transfer of Zn^{2+}. When the electrolyte contains urea, ZMO cannot be discovered at the cathode during charging and discharging. In contrast, without urea additive, the inert $ZnMn_3O_7$ phase is obviously detected during charging and discharging. Moreover, with the addition of urea, the valence states of Mn in the deposition increased obviously, thus giving rise to a higher capacity and better reversibility. In addition, a cationic accelerator strategy (CA) by adding poly(-vinylpyrrolidone) was proposed to regulate the cationic solvation structures, as reported by Chuai *et al.*[189] Theoretical calculations and experimental results demonstrated the effective promotion of the rapid migration of Zn^{2+} and Mn^{2+} in the electrolyte by CA, facilitating sufficient charge transfer at electrode–electrolyte interface. This beneficially contributed to the reversible electrochemical deposition/dissolution chemistry of

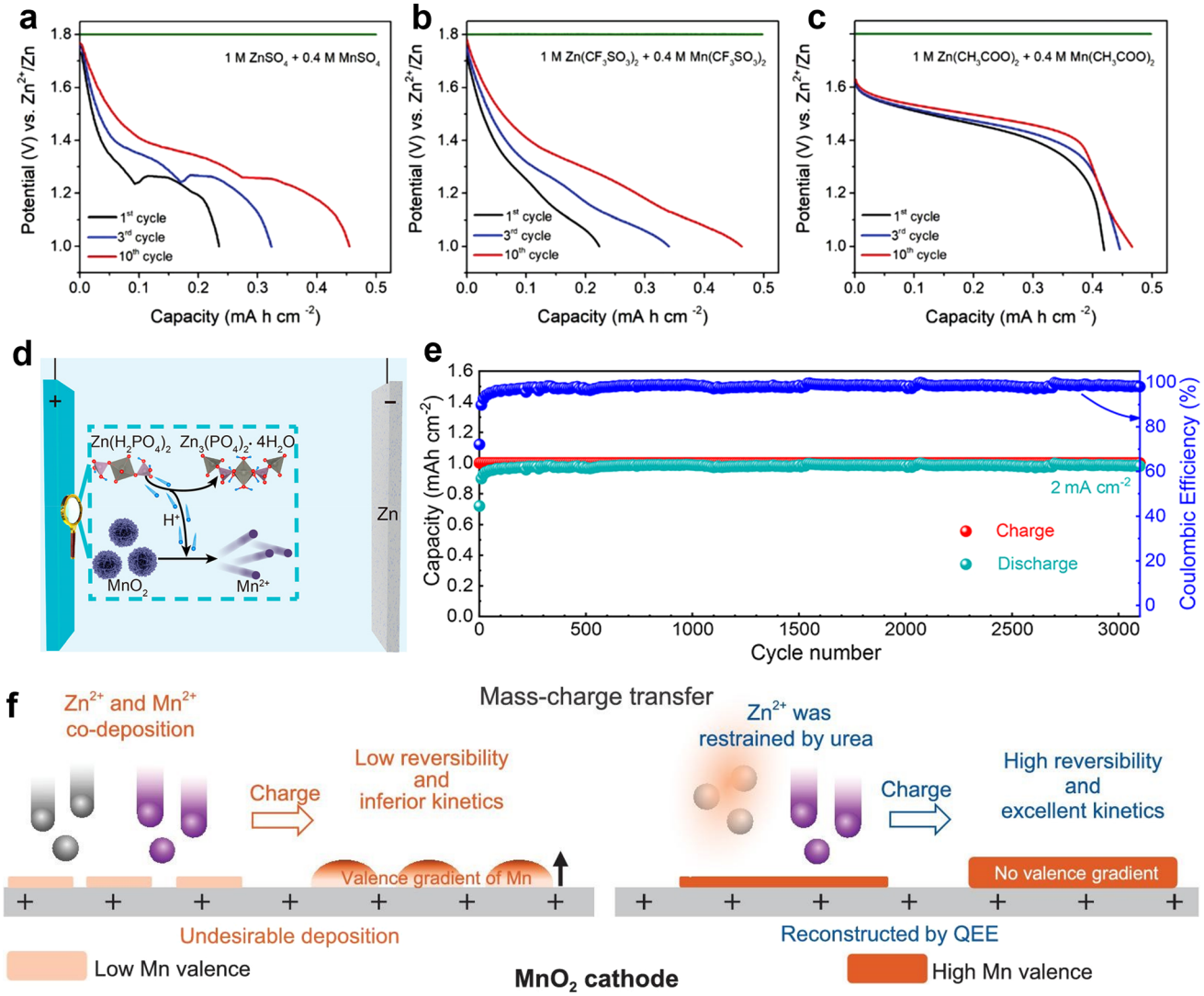

Fig. 15 Strategy for electrolyte regulation based on two-electron transfer reaction. (a) Galvanostatic discharge curves of a Zn/MnO_2 battery in sulfate-based, (b) sulfonate-based, and (c) acetate-based aqueous electrolytes. (a)–(c) Reproduced with permission.[184] Copyright 2020, Wiley-VCH. (d) Schematic illustration of $Zn(H_2PO_4)_2$ for facilitating MnO_2 dissolution. (e) Long-term cycling performance of a Zn–MnO_2 cell with $ZnCl_2$/$Mn(H_2PO_4)_2$ electrolyte. (d) and (e) Reproduced with permission.[186] Copyright 2022, the American Chemical Society. (f) Diagram of the electrochemical behavior of urea-based eutectic electrolyte at the cathode interface. Reproduced with permission.[188] Copyright 2023, Oxford University Press.

cathodic MnO_2/Mn^{2+} and anodic Zn/Zn^{2+}, leading long-term cycling stability for over 2000 cycles. The concentration of pre-added Mn^{2+} significantly influenced the long-term cycling performance. Shen *et al.*[190] demonstrated that adjusting the Mn^{2+} concentration to a critical range can recycle Mn^{2+} from MnOOH disproportionation, enabling the reversible redox conversion between MnO_2 and Mn^{2+}. As a result, an ultra-long lifespan of 16 000 cycles without noticeable capacity degradation was achieved.

In summary, a comprehensive discussion was presented on optimization strategies aimed at improving the cycling stability in manganese-based ZIBs, and the manganese-based materials for superior long-term cycling stability in ZIBs are summarized in Table 2. The formation of stable chemical bonds through compositing, pre-intercalation and heteroatom doping can mitigate the dissolution and structural collapse of manganese-based materials. Moreover, rational composite design can effectively reduce the deposition reaction of Mn^{2+} ions, preventing rapid electrolyte Mn^{2+} consumption and the formation of an inert ZMO phase. Meanwhile, reducing the dissolution barrier of manganese, promoting Mn^{2+} adsorption, and selectively alleviating Zn^{2+} deposition on the cathode by compositing or electrolyte regulation are beneficial for Mn dissolution and Mn^{2+} redeposition. Consequently, a stable cycling performance in manganese-based ZIBs can be achieved based on the reversible $Mn^{3+} \leftrightarrow Mn^{2+}$ reaction or $Mn^{4+} \leftrightarrow Mn^{2+}$ reaction, respectively.

Table 2 Summary of the stable cycling performance of manganese-based materials in ZIBs

Reaction mechanism/ electrodes	Electrolyte	Voltage window	Capacity retention (cycles/current density)	Strategies/causes	Ref.
One-electron transfer reaction				*Rational composite design*	
α-MnO_2@graphite nanosheets	2 M $ZnSO_4$ + 0.1 M $MnSO_4$	1–1.8 V	95% (600/1C) 98% (3000/6C)	Suppress Mn^{2+} electrodeposition	102
MnO_2@CeO_2	2 M $ZnSO_4$ + 0.1 M $MnSO_4$	0.8–1.8 V	89.68% (1000/1 A g^{-1})	Suppress Jahn–Teller distortion	140
$ZnMn_2O_4$@C	2 M $ZnSO_4$	0.8–1.8 V	86.4% (1500/1 A g^{-1})	Suppress Jahn–Teller distortion	139
δ-MnO_2-C NA	2 M $ZnSO_4$ + 0.1 M $MnSO_4$	0.8–1.8 V	90.4% (50 000/4 A g^{-1})	Buffer volume changes	191
N-doped carbon@δ-MnO_2	2 M $ZnSO_4$ + 0.3 M $MnSO_4$	1–1.8 V	87% (3500/2 A g^{-1})	Buffer volume changes	192
α-MnO_2/graphene scrolls	2 M $ZnSO_4$ + 0.2 M $MnSO_4$	1–1.85 V	94% (3000/3 A g^{-1})	Suppress cathode dissolution	136
Mn_2O_3–$ZnMn_2O_4$	$Zn(CF_3SO_3)_2$ + 0.1 M $MnSO_4$	0.8–1.8 V	93.3% (2000/3 A g^{-1})	Superior structural stability	146
$Ti_3C_2T_x$@MnO_2	2 M $ZnSO_4$ + 0.2 M $MnSO_4$	0.8–1.8 V	90.6% (2000/0.5 A g^{-1})	Suppress cathode dissolution	141
N-Mn_3O_4/MnO	2 M $ZnSO_4$ + 0.2 M $MnSO_4$	0.8–1.8 V	77.2% (2500/10 A g^{-1})	Alleviate stress	193
				Pre-intercalation	
$K_{0.27}MnO_2 \cdot 0.54H_2O$	2 M $ZnSO_4$ + 0.3 M $MnSO_4$	0.7–1.8 V	91% (1000/10C)	Suppress cathode dissolution	153
Al-intercalated MnO_2	2 M $ZnSO_4$	0.8–1.8 V	94.5% (2000/2 A g^{-1})	Suppress cathode dissolution	151
$Na_{0.55}Mn_2O_4 \cdot 1.5H_2O$	2 M $ZnSO_4$ + 0.1 M $MnSO_4$ + 0.5M Na_2SO_4	0.8–1.9 V	70% (10 000/6.5C)	Suppress cathode dissolution	194
$Na_{0.46}Mn_2O_4 \cdot 1.4H_2O$	2 M $ZnSO_4$ + 0.2 M $MnSO_4$	0.95–1.85 V	98% (10 000/20C)	Suppress cathode dissolution	154
Na^+-intercalated MnO_2	2 M $ZnSO_4$ + 0.2 M $MnSO_4$	0.9–1.8 V	93% (1000/4 A g^{-1})	Suppress cathode dissolution	195
Cu-MnO_2	2 M $ZnSO_4$ + 0.2 M $MnSO_4$	0.8–1.9 V	90.1% (700/5 A g^{-1})	Suppress cathode dissolution	152
$Co_x$$MnO_2$	2 M $ZnSO_4$ + 0.2 M $MnSO_4$	0.8–1.8 V	84.6 (500/0.5 A g^{-1})	Suppress cathode dissolution	150
NH_4^+-intercalated MnO_2	2 M $ZnSO_4$ + 0.1 M $MnSO_4$	0.8–1.8 V	69% (10 000/4 A g^{-1})	Suppress cathode dissolution	159
PANI-intercalated MnO_2	2 M $ZnSO_4$ + 0.1 M $MnSO_4$	1–1.8 V	~84% (5000/2 A g^{-1})	Suppress cathode dissolution	155
PVP–MnO_2	2 M $ZnSO_4$ + 0.2 M $MnSO_4$	0.8–1.8 V	~100% (20 000/10 A g^{-1})	Suppress cathode dissolution	156
				Heteroatom doping	
Al-doped MnO_2	2 M $ZnSO_4$ + 0.1 M $MnSO_4$	0.8–1.8 V	79% (15 000/4 A g^{-1})	Suppress cathode dissolution	196
Bi-doped MnO_2	2 M $ZnSO_4$ + 0.2 M $MnSO_4$	0.8–1.8 V	93% (10 000/1 A g^{-1})	Suppress cathode dissolution	197
Ni-doped MnO	2 M $ZnSO_4$ + 0.2 M $MnSO_4$	0.8–1.8 V	91% (6000/3 A g^{-1})	Enhance structure stability	198
Co-doped Mn_3O_4	2 M $ZnSO_4$ + 0.2 M $MnSO_4$	0.2–2.2 V	80% (1100/2 A g^{-1})	Suppress Jahn–Teller distortion	165
N-doped KMn_8O_{16}	2 M $ZnSO_4$ + 0.1 M $MnSO_4$	0.8–1.8 V	91% (2500/1 A g^{-1})	Suppress Jahn–Teller distortion	166
N-doped $Na_2Mn_3O_7$	2 M $ZnSO_4$ + 0.2 M $MnSO_4$	0.8–1.8 V	78.9% (550/2 A g^{-1})	Suppress cathode dissolution	174
K, Fe-doped $ZnMn_2O_4$	2 M $ZnSO_4$ + 0.2 M $MnSO_4$	0.8–1.8 V	88.1% (500/1 A g^{-1})	Suppress cathode dissolution	169
Two-electron transfer reaction				*Rational composite design*	
MnO_2/MoO_3	3 M $ZnSO_4$	0.2–2.2 V	92.6% (300/0.1 A g^{-1}) 80.1% (16 000/1 A g^{-1})	Facilitating dissolution/ deposition	180
MnO/MN	3 M $ZnSO_4$	0.6–1.9 V	80.3% (200/0.1 A g^{-1}) −(11 000/2 A g^{-1})	Facilitating deposition	132
MnO/PC	3 M $ZnSO_4$	0.8–1.9 V	93% (120/0.1 A g^{-1}) −(2000/2 A g^{-1})	Facilitating deposition/ dissolution	130
MnO_2@PDAAQ	2 M $ZnSO_4$ + 0.2 M $MnSO_4$	0.2–1.85 V	−(2000/2 A g^{-1})	Facilitating deposition/ dissolution	181
				Electrolyte regulation	
MnO_2/$Zn(H_2PO_4)_2$	2 M $ZnCl_2$ + 0.07 M $Mn(H_2PO_4)_2$	0.5–2.1 V	~100% (3000/2 mA cm^{-2})	Facilitating dissolution	186
MnO_2	1 M $ZnSO_4$ + 1 M $MnSO_4$ + 0.1 M H_2SO_4 + 0.07 mM PVP	1–2.2 V	90% (2000/20C)	Facilitating deposition/ dissolution	189
MnO_2	2 M $Zn(OTf)_2$ + 4 M urea + 0.25 M $MnSO_4$	0.8–1.8 V	76.8% (350/0.5 A g^{-1})	Restricting Zn^{2+} deposition	188
MnO_2	2 M $ZnSO_4$ + 0.4 M $MnSO_4$ + 0.8 NaAc	1–1.8 V	−(350/0.5 A g^{-1})	Facilitating deposition/ dissolution	185
MnO_2	1 M $Zn(Ac)_2$ + 0.4 M $Mn(Ac)_2$	1–1.8 V	~100% (4000/5 mA cm^{-2})	Facilitating deposition/ dissolution	184
MnO_2@CNT	2 M $ZnSO_4$ + 0.005 M $MnSO_4$	1–2.4 V	~100% (16 000/10 mA cm^{-2})	Facilitating deposition	190

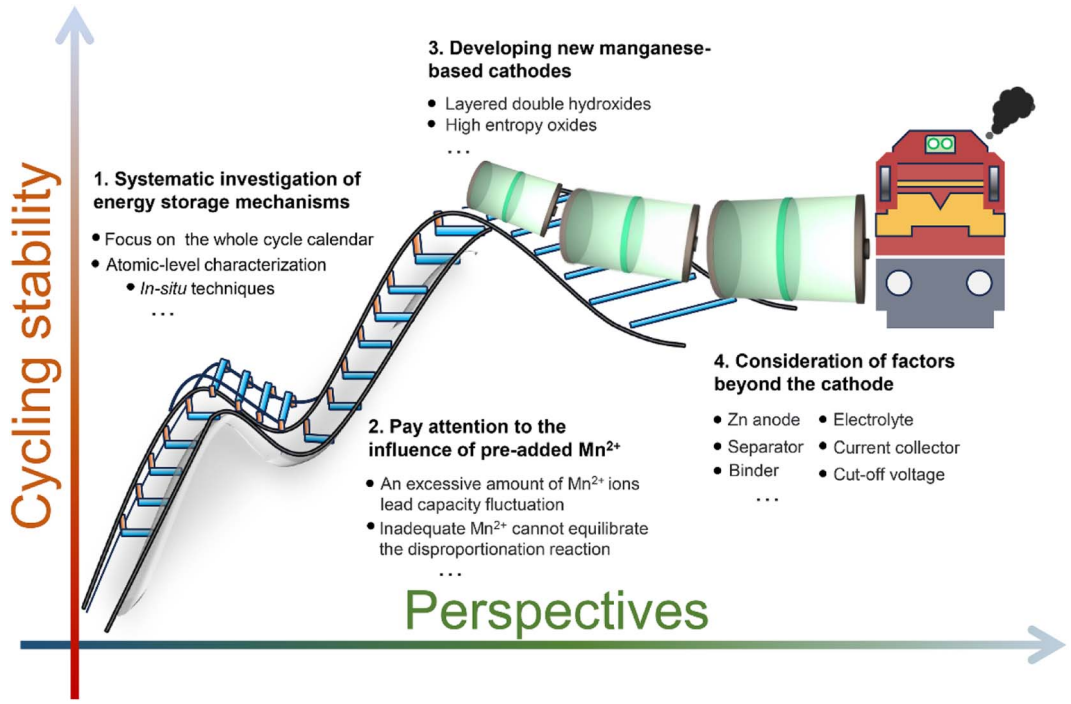

Fig. 16 Perspectives for achieving stable cycling performance in manganese-based ZIBs.

6 Summary and perspectives

Manganese-based ZIBs exhibit distinctive advantages and hold great promise for large-scale energy storage applications due to their cost-effectiveness, natural availability, low toxicity, multivalent states, high operation voltage, and satisfactory capacity. However, their unsatisfactory cycle stability coupled with intricate and contentious storage mechanisms hinder their commercial applications. In this review, the energy storage mechanisms of manganese-based ZIBs with different structures were systematically clarified and summarized. Subsequently, the capacity fluctuation of manganese-based ZIBs including capacity activation, degradation, and dynamic evolution in the whole cycle calendar were comprehensively analyzed. Lastly, the constructive optimization strategies based on the reaction chemistry of one-electron or two-electron transfer for achieving a durable cycling performance in manganese-based ZIBs were put forward, respectively. Nevertheless, challenges and disputes still persist in manganese-based ZIBs. Herein, we conclude some challenges and prospects in the reaction chemistry and optimization strategies for achieving a stable cycling performance in manganese-based ZIBs, as illustrated in Fig. 16.

(i) Systematic investigation of energy storage mechanisms. Given that the storage mechanisms have been discovered successively and the quick development of advanced characterization techniques in recent years, early reports may give incorrect and incomplete analyses. For example, there have been reports suggesting the complete transformation of the tunnel phase in α-MnO_2 during discharge, followed by subsequent recovery upon charging. However, the extent of this remarkable structural reversibility raises questions due to the high energy demand associated with charge ordering during tunnel formation.[199] Moreover, conventional characterization of the reaction mechanisms heavily relies on interpretations based on bulk-level characterizations, which may overlook the crucial local changes occurring within cells and potentially lead to misinterpretation of the reaction mechanisms due to the presence of side products or residual electrolytes.[200] For instance, routinely used XRD techniques may yield ambiguous data due to the formation of various phases of low symmetry, adding layers upon cycling. In addition, the specific roles of Zn^{2+} and H^+ during charge/discharge remain ambiguous. However, employing crucial analysis methods, such as solid-state ^{67}Zn and ^1H (^1D) NMR-mass spectroscopy with isotope labeling can potentially facilitate a more comprehensive evaluation of the contribution of Zn^{2+} and H^+, although this task remains challenging.[92] Furthermore, it is worth noting that in most reports, a single electrochemical reaction process is declared in the whole cycle calendar. However, the reaction chemistry usually consists of multiple processes that dominate at different stages with a dynamic change in the Mn valence and electrolyte pH. Therefore, investigations into energy storage mechanisms based solely on initial cycles may not fully account for the complexities of the entire cycle. Consequently, the development of more advanced characterization technologies such as atomic-level characterization and *in situ* techniques combined with the continuous monitoring of dynamic changes in the entire cycle, will facilitate a comprehensive understanding of the energy storage mechanisms inherent to manganese-based ZIBs.

(ii) Paying attention to the influence of pre-added Mn^{2+}. On the one hand, the Mn^{2+} additives would stabilize the cycling performance to some extent by compensating for the capacity

loss of Mn^{2+} electrodeposition or mitigating the Jahn–Teller effect. On the other hand, the pre-added Mn^{2+} increases the complexity of reaction chemistry in manganese-based ZIBs and may obscure the electrochemical behaviors of the original cathode due to its deposition. Although extra capacity can be obtained, the accumulation of by-products such as a ZMO phase resulting from the transformation of deposited Mn^{2+} can lead to rapid capacity degradation and even battery failure. In addition, the content of Mn^{2+} in the electrolyte not only impacts the cycle stability, but also dominates the reaction rate between insertion/extraction chemistry and dissolution/deposition chemistry. Excessive Mn^{2+} in the electrolyte may facilitate the dissolution/deposition reaction, while inadequate Mn^{2+} may compromise the cycling stability. Moreover, the presence of pre-added Mn^{2+} has an influence on pH fluctuations, thereby further impacting the energy storage mechanism. The excessive addition of Mn^{2+} can effectively suppress the formation of ZHS, but may also alter the reaction mechanism by reducing the electrolyte pH.[92] Therefore, gaining a comprehensive understanding of pre-added Mn^{2+} is important for researchers to comprehend the underlying reaction mechanisms in manganese-based ZIBs and devise effective strategies to enhance their cycle stability.

(iii) Developing new manganese-based cathodes. Developing novel manganese-based cathodes is of paramount importance for the large-scale implementation of ZIBs. Despite the fact that traditional manganese oxides have been widely investigated as cathode materials for ZIBs, ZIBs still suffer from the lack of high-performance cathode materials. Ensuring the structural stability of manganese-based materials during Zn^{2+} storage is crucial for achieving cycling stability. The search for new stable manganese-based cathodes, such as manganese-based layered double hydroxide (LDH) and high entropy oxides (HEOs), presents a promising avenue.[201] For example, HEOs ($Co_{0.6}Ni_{0.6}Fe_{0.6}Mn_{0.6}Cu_{0.6}O_4$) with long-range disorders and a fixed lattice structure can effectively alleviate the structural collapse induced by the strong electrostatic force between Zn^{2+}, thereby achieving remarkable long-term stability.[202] Additionally, a trinary LDH with hydrogen vacancies ($Ni_3Mn_{0.7}Fe_{0.3}$-LDH) has been reported as a novel cathode material for ZIBs, exhibiting a reversible high capacity of up to 328 mA h g^{-1} and demonstrating excellent cycling stability over 500 cycles with a capacity retention of 85%.[203] However, their stable cycling performance still relied on the presence of pre-added Mn^{2+}, which may lead to a misinterpretation of their inherent structural stability. Therefore, to realize the stable cycling performance of manganese-based ZIBs, it is imperative to not only optimize traditional manganese oxides but also dedicate more efforts towards developing new manganese-based cathodes with intrinsic structural stability.

(iv) Consideration of factors beyond the cathode. Besides rational modifications to manganese-based cathodes and electrolytes, attention should also be given beyond the cathode. The Zn anode faces challenges such as dendrite formation, passivation, corrosion, and hydrogen evolution, which significantly impede the cycling performance stability. Effective strategies for achieving Zn anodes with a long lifespan include the deposition of artificial interface layers, electrode design, and electrolyte modifications.[204] For example, the addition of DMSO to the electrolyte has been demonstrated to facilitate the formation of a solid electrolyte interphase on the anode, effectively preventing Zn dendrite growth and water decomposition.[205] In addition, although glass fiber separators are commonly used in ZIBs, their inherent fragility and large pores make them susceptible to penetration by Zn dendrites, leading to battery failure after repetitive plating/stripping.[206,207] Modifying traditional glass fiber separators or developing novel separators can help regulate the electric field distribution uniformly and suppress dendrite formation as well as parasitic side reactions. Besides, current collectors and binders cannot be neglected as well. Furthermore, optimizing the cut-off voltage from the perspective of electrochemical parameters is another way to enhance the cycling stability of manganese-based ZIBs, which could avoid side reactions or activate inactive materials.[117,208,209] For instance, extending the voltage cut-off to 2.2 V enables the activation of previously inactive components, facilitating a reversible MnO_2/Mn^{2+} reaction with two-electron transfer.[210] However, the investigation of cycling stability beyond the cathode remains inadequate. Therefore, to achieve the maximum cycling stability, more attention should be paid to optimizing beyond the cathode.

Author contributions

The manuscript was written through contributions of all authors. All authors have given approval to the final version of the manuscript.

Conflicts of interest

There are no conflicts to declare.

References

1 Z. Yang, J. Zhang, M. Kintner-Meyer, X. Lu, D. Choi, J. Lemmon and J. Liu, *Chem. Rev.*, 2011, **111**, 3577–3613.
2 L. Yang, K. Yang, J. Zheng, K. Xu, K. Amine and F. Pan, *Chem. Soc. Rev.*, 2020, **49**, 4667–4680.
3 B. Dunn, H. Kamath and J. Tarascon, *Science*, 2011, **334**, 928–935.
4 J. W. Choi and D. Aurbach, *Nat. Rev. Mater.*, 2016, **1**, 16013.
5 M. Li, J. Lu, Z. Chen and K. Amine, *Adv. Mater.*, 2018, **30**, 1800561.
6 B. Liu, Y. Jia, J. Li, S. Yin, C. Yuan, Z. Hu, L. Wang, Y. Li and J. Xu, *J. Mater. Chem. A*, 2018, **6**, 21475–21484.
7 S. Abada, G. Marlair, A. Lecocq, M. Petit, V. Sauvant-Moynot and F. Huet, *J. Power Sources*, 2016, **306**, 178–192.
8 L. Blanc, D. Kundu and L. Nazar, *Joule*, 2020, **4**, 771–799.
9 D. Selvakumaran, A. Pan, S. Liang and G. Cao, *J. Mater. Chem. A*, 2019, **7**, 18209–18236.
10 L. Chen, Q. An and L. Mai, *Adv. Mater. Interfaces*, 2019, **6**, 1900387.
11 J. Yan, J. Wang, H. Liu, Z. Bakenov, D. Gosselink and P. Chen, *J. Power Sources*, 2012, **216**, 222–226.

12 Y. Zong, H. Chen, J. Wang, M. Wu, Y. Chen, L. Wang, X. Huang, H. He, X. Ning, Z. Bai, W. Wen, D. Zhu, X. Ren, N. Wang and S. Dou, *Adv. Mater.*, 2023, **35**, 2306269.
13 J. Yin, Y. Wang, Y. Zhu, J. Jin, C. Chen, Y. Yuan, Z. Bayhan, N. Salah, N. Alhebshi, W. Zhang, U. Schwingenschlögl and H. Alshareef, *Nano Energy*, 2022, **99**, 107331.
14 Q. Zhang, J. Luan, Y. Tang, X. Ji and H. Wang, *Angew. Chem., Int. Ed.*, 2020, **59**, 13180–13191.
15 Y. Dai, C. Zhang, W. Zhang, L. Cui, C. Ye, X. Hong, J. Li, R. Chen, W. Zong, X. Gao, J. Zhu, P. Jiang, Q. An, D. J. L. Brett, I. P. Parkin, G. He and L. Mai, *Angew. Chem., Int. Ed.*, 2023, **62**, e202301192.
16 T. Wei, Y. Ren, Y. Wang, L. e. Mo, Z. Li, H. Zhang, L. Hu and G. Cao, *ACS Nano*, 2023, **17**, 3765–3775.
17 Y. Lin, Z. Mai, H. Liang, Y. Li, G. Yang and C. Wang, *Energy Environ. Sci.*, 2023, **16**, 687–697.
18 N. Chodankar, P. Shinde, S. Patil, G. Rama Raju, S. Hwang, S. Marje, H. Tyagaraj, E. Al Hajri, A. Al Ghaferi, Y. Huh and Y. Han, *ChemSusChem*, 2023, **16**, e202300730.
19 J. Chen, W. Xu, H. Wang, X. Ren, F. Zhan, Q. He, H. Wang and L. Chen, *J. Mater. Chem. A*, 2022, **10**, 21197–21250.
20 F. Gao, B. Mei, X. Xu, J. Ren, D. Zhao, Z. Zhang, Z. Wang, Y. Wu, X. Liu and Y. Zhang, *Chem. Eng. J.*, 2022, **448**, 137742.
21 X. Zhao, L. Mao, Q. Cheng, F. Liao, G. Yang, X. Lu and L. Chen, *Energy Storage Mater.*, 2021, **38**, 397–437.
22 M. Wu, J. Bai, M. Xue, X. Zhao, L. Mao and L. Chen, *Chem. Commun.*, 2023, **59**, 11668–11671.
23 X. Zhao, L. Mao, Q. Cheng, F. Liao, G. Yang and L. Chen, *Chem. Commun.*, 2022, **624**, 482–493.
24 G. Zampardi and F. La Mantia, *Curr. Opin. Electrochem.*, 2020, **21**, 84–92.
25 H. Wang, Q. He, S. Liang, Y. Li, X. Zhao, L. Mao, F. Zhan and L. Chen, *Energy Storage Mater.*, 2021, **43**, 531–578.
26 H. Yi, R. Qin, S. Ding, Y. Wang, S. Li, Q. Zhao and F. Pan, *Adv. Funct. Mater.*, 2021, **31**, 2006970.
27 H. Wang, X. Ren, J. Chen, W. Xu, Q. He, H. Wang, F. Zhan and L. Chen, *J. Power Sources*, 2023, **554**, 232309.
28 Q. He, J. Bai, H. Wang and Y. Liao, *Chem. Eng. J.*, 2024, **485**, 149893.
29 T. Sun, J. Xie, W. Guo, D. Li and Q. Zhang, *Adv. Energy Mater.*, 2020, **10**, 1904199.
30 Z. Tie and Z. Niu, *Angew. Chem., Int. Ed.*, 2020, **59**, 21293–21303.
31 G. Fang, J. Zhou, A. Pan and S. Liang, *ACS Energy Lett.*, 2018, **3**, 2480–2501.
32 K. Nam, H. Kim, J. Choi and J. Choi, *Energy Environ. Sci.*, 2019, **12**, 1999–2009.
33 T. Xiong, Z. Yu, H. Wu, Y. Du, Q. Xie, J. Chen, Y. Zhang, S. Pennycook, W. Lee and J. Xue, *Adv. Energy Mater.*, 2019, **9**, 1803815.
34 A. Zhang, R. Zhao, Y. Wang, J. Yang, C. Wu and Y. Bai, *Energy Environ. Sci.*, 2023, **16**, 3240–3301.
35 Q. Dai, L. Li, T. Hoang, T. Tu, B. Hu, Y. Jia, M. Zhang, L. Song and M. Trudeau, *J. Energy Storage*, 2022, **55**, 105397.
36 S. Xie, X. Li, Y. Li, Q. Liang and L. Dong, *Chem. Rec.*, 2022, **22**, e202200201.
37 N. Zhang, Y. Ji, J. Wang, P. Wang, Y. Zhu and T. Yi, *J. Energy Chem.*, 2023, **82**, 423–463.
38 X. Cui, Y. Zhang, J. Zhang, E. Xie and J. Fu, *Adv. Mater. Technol.*, 2023, **8**, 2300321.
39 T. Xiong, Y. Zhang, W. Lee and J. Xue, *Adv. Energy Mater.*, 2020, **10**, 2001769.
40 N. Zhang, J. Wang, Y. Guo, P. Wang, Y. Zhu and T. Yi, *Coord. Chem. Rev.*, 2023, **479**, 215009.
41 M. Han, L. Qin, Z. Liu, L. Zhang, X. Li, B. Lu, J. Huang, S. Liang and J. Zhou, *Mater. Today Energy*, 2021, **20**, 100626.
42 W. Shi, W. Lee and J. Xue, *ChemSusChem*, 2021, **14**, 1634–1658.
43 N. Zhang, J. Wang, X. Liu, P. Wang, Y. Liu, Y. Xie and T. Yi, *Composites, Part B*, 2023, **260**, 110770.
44 X. Jia, C. Liu, Z. G. Neale, J. Yang and G. Cao, *Chem. Rev.*, 2020, **120**, 7795–7866.
45 Z. Zhang, H. Shang, X. Zhang, C. Liu, S. Li, Z. Wen, S. Ji and J. Sun, *ACS Appl. Energy Mater.*, 2021, **4**, 5113–5122.
46 X. Du, G. Guan, X. Li, A. D. Jagadale, X. Ma, Z. Wang, X. Hao and A. Abudula, *J. Mater. Chem. A*, 2016, **4**, 13989–13996.
47 C. Yuan, Y. Zhang, Y. Pan, X. Liu, G. Wang and D. Cao, *Electrochim. Acta*, 2014, **116**, 404–412.
48 W. Chen, X. Zhan, B. Luo, Z. Ou, P. Shih, L. Yao, S. Pidaparthy, A. Patra, H. An, P. Braun, R. Stephens, H. Yang, J. Zuo and Q. Chen, *Nano Lett.*, 2019, **19**, 4712–4720.
49 M. Liu, Q. Zhao, H. Liu, J. Yang, X. Chen, L. Yang, Y. Cui, W. Huang, W. Zhao, A. Song, Y. Wang, S. Ding, Y. Song, G. Qian, H. Chen and F. Pan, *Nano Energy*, 2019, **64**, 103942.
50 W. Liu, X. Zhang, Y. Huang, B. Jiang, Z. Chang, C. Xu and F. Kang, *J. Energy Chem.*, 2021, **56**, 365–373.
51 S. Islam, M. Alfaruqi, V. Mathew, J. Song, S. Kim, S. Kim, J. Jo, J. Baboo, D. Pham, D. Putro, Y. Sun and J. Kim, *J. Mater. Chem. A*, 2017, **5**, 23299–23309.
52 M. Han, J. Huang, S. Liang, L. Shan, X. Xie, Z. Yi, Y. Wang, S. Guo and J. Zhou, *iScience*, 2020, **23**, 100797.
53 N. Zhang, F. Cheng, J. Liu, L. Wang, X. Long, X. Liu, F. Li and J. Chen, *Nat. Commun.*, 2017, **8**, 405.
54 M. Alfaruqi, V. Mathew, J. Gim, S. Kim, J. Song, J. Baboo, S. Choi and J. Kim, *Chem. Mater.*, 2015, **27**, 3609–3620.
55 C. Wang, Y. Zeng, X. Xiao, S. Wu, G. Zhong, K. Xu, Z. Wei, W. Su and X. Lu, *J. Energy Chem.*, 2020, **43**, 182–187.
56 Y. Liao, H. Chen, C. Yang, R. Liu, Z. Peng, H. Cao and K. Wang, *Energy Storage Mater.*, 2022, **44**, 508–516.
57 J. Lee, J. Ju, W. Cho, B. Cho and S. Oh, *Electrochim. Acta*, 2013, **112**, 138–143.
58 L. Chen, X. Guo, W. Lu, M. Chen, Q. Li, H. Xue and H. Pang, *Coord. Chem. Rev.*, 2018, **368**, 13–34.
59 W. Li, X. Gao, Z. Chen, R. Guo, G. Zou, H. Hou, W. Deng, X. Ji and J. Zhao, *Chem. Eng. J.*, 2020, **402**, 125509.
60 C. Zhu, G. Fang, S. Liang, Z. Chen, Z. Wang, J. Ma, H. Wang, B. Tang, X. Zheng and J. Zhou, *Energy Storage Mater.*, 2020, **24**, 394–401.
61 B. Jiang, C. Xu, C. Wu, L. Dong, J. Li and F. Kang, *Electrochim. Acta*, 2017, **229**, 422–428.

62 X. Shan, D. S. Charles, Y. Lei, R. Qiao, G. Wang, W. Yang, M. Feygenson, D. Su and X. Teng, *Nat. Commun.*, 2016, **7**, 13370.
63 J. Sun, D. Li, S. Wang, J. Xu, W. Liu, M. Ren, F. Kong, S. Wang and L. Yang, *J. Alloys Compd.*, 2021, **867**, 159034.
64 N. Zhang, F. Cheng, Y. Liu, Q. Zhao, K. Lei, C. Chen, X. Liu and J. Chen, *J. Am. Chem. Soc.*, 2016, **138**, 12894–12901.
65 V. Soundharrajan, B. Sambandam, S. Kim, V. Mathew, J. Jo, S. Kim, J. Lee, S. Islam, K. Kim, Y.-K. Sun and J. Kim, *ACS Energy Lett.*, 2018, **3**, 1998–2004.
66 Y. Gao, H. Yang, Y. Bai and C. Wu, *J. Mater. Chem. A*, 2021, **9**, 11472–11500.
67 X. Hou, X. Liu, H. Wang, X. Zhang, J. Zhou and M. Wang, *Energy Storage Mater.*, 2023, **57**, 577–606.
68 T. Zhang, Y. Tang, G. Fang, C. Zhang, H. Zhang, X. Guo, X. Cao, J. Zhou, A. Pan and S. Liang, *Adv. Funct. Mater.*, 2020, **30**, 2002711.
69 H. Guo, Z. Shao, Y. Zhang, X. Cui, L. Mao, S. Cheng, M. Ma, W. Lan, Q. Su and E. Xie, *J. Colloid Interface Sci.*, 2022, **608**, 1481–1488.
70 X. Wu, Y. Li, Y. Xiang, Z. Liu, Z. He, X. Wu, Y. Li, L. Xiong, C. Li and J. Chen, *J. Power Sources*, 2016, **336**, 35–39.
71 Y. Wu, J. Fee, Z. Tobin, A. Shirazi-Amin, P. Kerns, S. Dissanayake, A. Mirich and S. L. Suib, *ACS Appl. Energy Mater.*, 2020, **3**, 1627–1633.
72 Y. Cai, R. Chua, S. Huang, H. Ren and M. Srinivasan, *Chem. Eng. J.*, 2020, **396**, 125221.
73 X. Chen, W. Li, Y. Xu, Z. Zeng, H. Tian, M. Velayutham, W. Shi, W. Li, C. Wang, D. Reed, V. V. Khramtsov, X. Li and X. Liu, *Nano Energy*, 2020, **75**, 104869.
74 M. Wang, C. Cao, F. Su, Y. Wang, W. Wang, C. Ding, J. Bai, T. Liu, X. Sun and J. Zhang, *J. Power Sources*, 2020, **477**, 229013.
75 X. Dong, J. Sun, Y. Mu, Y. Yu, T. Hu, C. Miao, C. Huang, C. Meng and Y. Zhang, *J. Colloid Interface Sci.*, 2022, **610**, 805–817.
76 T. Zhu, K. Zheng, P. Wang, X. Cai, X. Wang, D. Gao, D. Yu, C. Chen and Y. Liu, *J. Colloid Interface Sci.*, 2022, **610**, 796–804.
77 S. Wang, G. Zeng, Q. Sun, Y. Feng, X. Wang, X. Ma, J. Li, H. Zhang, J. Wen, J. Feng, L. Ci, A. Cabot and Y. Tian, *ACS Nano*, 2023, **17**, 13256–13268.
78 H. Pan, Y. Shao, P. Yan, Y. Cheng, K. S. Han, Z. Nie, C. Wang, J. Yang, X. Li, P. Bhattacharya, K. T. Mueller and J. Liu, *Nat. Energy*, 2016, **1**, 16039.
79 Y. Jin, L. Zou, L. Liu, M. Engelhard, R. Patel, Z. Nie, K. Han, Y. Shao, C. Wang, J. Zhu, H. Pan and J. Liu, *Adv. Mater.*, 2019, **31**, 1900567.
80 Z. Tang, W. Chen, Z. Lyu and Q. Chen, *Energy Mater. Adv.*, 2022, **2022**, 9765710.
81 J. Wang, J.-G. Wang, H. Liu, Z. You, C. Wei and F. Kang, *J. Power Sources*, 2019, **438**, 226951.
82 D. Feng, T. Gao, L. Zhang, B. Guo, S. Song, Z. Qiao and S. Dai, *Nano-Micro Lett.*, 2019, **12**, 14.
83 J. Hao, J. Mou, J. Zhang, L. Dong, W. Liu, C. Xu and F. Kang, *Electrochim. Acta*, 2018, **259**, 170–178.
84 X. Wu, Y. Xiang, Q. Peng, X. Wu, Y. Li, F. Tang, R. Song, Z. Liu, Z. He and X. Wu, *J. Mater. Chem. A*, 2017, **5**, 17990–17997.
85 L. Jiang, Z. Wu, Y. Wang, W. Tian, Z. Yi, C. Cai, Y. Jiang and L. Hu, *ACS Nano*, 2019, **13**, 10376–10385.
86 N. Yadav, S. Khamsanga, S. Kheawhom, J. Qin and P. Pattananuwat, *J. Energy Storage*, 2023, **64**, 107148.
87 J. Li, L. Li, H. Shi, Z. Zhong, X. Niu, P. Zeng, Z. Long, X. Chen, J. Peng, Z. Luo, X. Wang and S. Liang, *ACS Sustainable Chem. Eng.*, 2020, **8**, 10673–10681.
88 M. R. Palacín, *Chem. Soc. Rev.*, 2009, **38**, 2565–2575.
89 C. Xu, B. Li, H. Du and F. Kang, *Angew. Chem., Int. Ed.*, 2012, **51**, 933–935.
90 B. Lee, C. S. Yoon, H. R. Lee, K. Y. Chung, B. W. Cho and S. H. Oh, *Sci. Rep.*, 2014, **4**, 6066.
91 B. Lee, H. Lee, H. Kim, K. Chung, B. Cho and S. Oh, *Chem. Commun.*, 2015, **51**, 9265–9268.
92 B. Sambandam, V. Mathew, S. Kim, S. Lee, S. Kim, J. Hwang, H. Fan and J. Kim, *Chem*, 2022, **8**, 924–946.
93 M. Alfaruqi, S. Islam, D. Putro, V. Mathew, S. Kim, J. Jo, S. Kim, Y. Sun, K. Kim and J. Kim, *Electrochim. Acta*, 2018, **276**, 1–11.
94 Y. Yuan, R. Sharpe, K. He, C. Li, M. Saray, T. Liu, W. Yao, M. Cheng, H. Jin, S. Wang, K. Amine, R. Shahbazian-Yassar, M. Islam and J. Lu, *Nat. Sustainability*, 2022, **5**, 890–898.
95 H. Chen, C. Dai, F. Xiao, Q. Yang, S. Cai, M. Xu, H. J. Fan and S.-J. Bao, *Adv. Mater.*, 2022, **34**, 2109092.
96 W. Sun, F. Wang, S. Hou, C. Yang, X. Fan, Z. Ma, T. Gao, F. Han, R. Hu, M. Zhu and C. Wang, *J. Am. Chem. Soc.*, 2017, **139**, 9775–9778.
97 W. Du, E. Ang, Y. Yang, Y. Zhang, M. Ye and C. Li, *Energy Environ. Sci.*, 2020, **13**, 3330–3360.
98 B. Lee, H. Seo, H. Lee, C. Yoon, J. Kim, K. Chung, B. Cho and S. Oh, *ChemSusChem*, 2016, **9**, 2948–2956.
99 M. Wang, X. Zheng, X. Zhang, D. Chao, S. Qiao, H. Alshareef, Y. Cui and W. Chen, *Adv. Energy Mater.*, 2021, **11**, 2002904.
100 X. Guo, J. Zhou, C. Bai, X. Li, G. Fang and S. Liang, *Mater. Today Energy*, 2020, **16**, 100396.
101 D. Wu, L. Housel, S. Kim, N. Sadique, C. Quilty, L. Wu, R. Tappero, S. L. Nicholas, S. Ehrlich, Y. Zhu, A. Marschilok, E. Takeuchi, D. Bock and K. Takeuchi, *Energy Environ. Sci.*, 2020, **13**, 4322–4333.
102 R. Liang, J. Fu, Y.-P. Deng, Y. Pei, M. Zhang, A. Yu and Z. Chen, *Energy Storage Mater.*, 2021, **36**, 478–484.
103 Y. Huang, J. Mou, W. Liu, X. Wang, L. Dong, F. Kang and C. Xu, *Nano-Micro Lett.*, 2019, **11**, 49.
104 D. Chao, W. Zhou, C. Ye, Q. Zhang, Y. Chen, L. Gu, K. Davey and S. Qiao, *Angew. Chem., Int. Ed.*, 2019, **58**, 7823–7828.
105 Y. Ma, Y. Ma, T. Diemant, K. Cao, X. Liu, U. Kaiser, R. J. Behm, A. Varzi and S. Passerini, *Adv. Energy Mater.*, 2021, **11**, 2100962.
106 W. Xie, K. Zhu, H. Yang and W. Yang, *Adv. Mater.*, 2023, **36**, 2306154.
107 R. He, F. Yu, K. Wu, H. Liu, Z. Li, H. Liu, S. Dou and C. Wu, *Nano Lett.*, 2023, **23**, 6050–6058.

108 L. Han, Q. Wang, R. Pang, D. Zhang, B. Zhao, W. Meng, M. Li, Y. Zhang, A. Cao and Y. Shang, *Adv. Energy Mater.*, 2023, **13**, 2302395.
109 J. Yue, S. Chen, J. Yang, S. Li, G. Tan, R. Zhao, C. Wu and Y. Bai, *Adv. Mater.*, 2023, **36**, 2304040.
110 X. Li, L. Wang, Y. Fu, H. Dang, D. Wang and F. Ran, *Nano Energy*, 2023, **116**, 108858.
111 M. Xue, J. Bai, M. Wu, Q. He, Q. Zhang and L. Chen, *Energy Storage Mater.*, 2023, **62**, 102940.
112 T. Wu, Y. Lin, Z. Althouse and N. Liu, *ACS Appl. Energy Mater.*, 2021, **4**, 12267–12274.
113 J. Huang, X. Tang, K. Liu, G. Fang, Z. He and Z. Li, *Mater. Today Energy*, 2020, **17**, 100475.
114 L. Wang, Z. Wu, J. Zou, P. Gao, X. Niu, H. Li and L. Chen, *Joule*, 2019, **3**, 2086–2102.
115 B. Tang, L. Shan, S. Liang and J. Zhou, *Energy Environ. Sci.*, 2019, **12**, 3288–3304.
116 J. Cao, D. Zhang, X. Zhang, S. Wang, J. Han, Y. Zhao, Y. Huang and J. Qin, *Appl. Surf. Sci.*, 2020, **534**, 147630.
117 Y. Li, S. Wang, J. R. Salvador, J. Wu, B. Liu, W. Yang, J. Yang, W. Zhang, J. Liu and J. Yang, *Chem. Mater.*, 2019, **31**, 2036–2047.
118 J. Gallaway, M. Menard, B. Hertzberg, Z. Zhong, M. Croft, L. Sviridov, D. Turney, S. Banerjee, D. Steingart and C. Erdonmez, *J. Electrochem. Soc.*, 2015, **162**, A162.
119 H. Yang, T. Zhang, D. Chen, Y. Tan, W. Zhou, L. Li, W. Li, G. Li, W. Han, H. J. Fan and D. Chao, *Adv. Mater.*, 2023, **35**, 2300053.
120 H. Yang, W. Zhou, D. Chen, J. Liu, Z. Yuan, M. Lu, L. Shen, V. Shulga, W. Han and D. Chao, *Energy Environ. Sci.*, 2022, **15**, 1106–1118.
121 L. Li, T. K. A. Hoang, J. Zhi, M. Han, S. Li and P. Chen, *ACS Appl. Mater. Interfaces*, 2020, **12**, 12834–12846.
122 S. Zhao, B. Han, D. Zhang, Q. Huang, L. Xiao, L. Chen, D. Ivey, Y. Deng and W. Wei, *J. Mater. Chem. A*, 2018, **6**, 5733–5739.
123 C. Qiu, X. Zhu, L. Xue, M. Ni, Y. Zhao, B. Liu and H. Xia, *Electrochim. Acta*, 2020, **351**, 136445.
124 S. Cui, D. Zhang and Y. Gan, *J. Power Sources*, 2023, **579**, 233293.
125 H. Ren, J. Zhao, L. Yang, Q. Liang, S. Madhavi and Q. Yan, *Nano Res.*, 2019, **12**, 1347–1353.
126 V. Soundharrajan, B. Sambandam, S. Kim, S. Islam, J. Jo, S. Kim, V. Mathew, Y. Sun and J. Kim, *Energy Storage Mater.*, 2020, **28**, 407–417.
127 Q. Wang, G. Tian, C. Huang and D. Zhang, *Small*, 2023, **19**, 2301189.
128 H. Chen, S. Cai, Y. Wu, W. Wang, M. Xu and S. J. Bao, *Mater. Today Energy*, 2021, **20**, 100646.
129 N. Qiu, H. Chen, Z. Yang, S. Sun and Y. Wang, *RSC Adv.*, 2018, **8**, 15703–15708.
130 Y. Liu, Y. Ma, W. Yang, S. Bao, H. Chen and M. Xu, *Chem. Eng. J.*, 2023, **473**, 145490.
131 B. Yang, X. Cao, S. Wang, N. Wang and C. Sun, *Electrochim. Acta*, 2021, **385**, 138447.
132 Y. Liu, Z. Qin, X. Yang and X. Sun, *Adv. Funct. Mater.*, 2022, **32**, 2106994.
133 Y. Kim, Y. Park, M. Kim, J. Lee, K. Kim and J. Choi, *Nat. Commun.*, 2022, **13**, 2371.
134 P. Oberholzer, E. Tervoort, A. Bouzid, A. Pasquarello and D. Kundu, *ACS Appl. Mater. Interfaces*, 2019, **11**, 674–682.
135 O. Fitz, C. Bischoff, M. Bauer, H. Gentischer, K. Birke, H. Henning and D. Biro, *ChemElectroChem*, 2021, **8**, 3553–3566.
136 B. Wu, G. Zhang, M. Yan, T. Xiong, P. He, L. He, X. Xu and L. Mai, *Small*, 2018, **14**, 1703850.
137 X. Xiao, L. Zhang, W. Xin, M. Yang, Y. Geng, M. Niu, H. Zhang and Z. Zhu, *Small*, 2024, 2309271.
138 X. Zhai, J. Qu, J. Wang, W. Chang, H. Liu, Y. Liu, H. Yuan, X. Li and Z. Yu, *Energy Storage Mater.*, 2021, **42**, 753–763.
139 S. Deng, Z. Tie, F. Yue, H. Cao, M. Yao and Z. Niu, *Angew. Chem., Int. Ed.*, 2022, **61**, e202115877.
140 M. Xie, R. Wang, N. Wang, Q. Zhang, X. Zhang, C. Feng, L. Huang, Y. Xu, Y. Jiao and J. Chen, *J. Mater. Chem. A*, 2023, **11**, 21927–21936.
141 M. Shi, B. Wang, C. Chen, J. Lang, C. Yan and X. Yan, *J. Mater. Chem. A*, 2020, **8**, 24635–24644.
142 X. Zhu, Z. Cao, W. Wang, H. Li, J. Dong, S. Gao, D. Xu, L. Li, J. Shen and M. Ye, *ACS Nano*, 2021, **15**, 2971–2983.
143 Y. Li, Z. Yuan, D. Li, J. Li, Y. Zhang, M. Wang, G. Li, L. Wang and W. Han, *ACS Nano*, 2024, **18**, 4733–4745.
144 Z. Yuan, Q. Lin, Y. Li, W. Han and L. Wang, *Adv. Mater.*, 2023, **35**, 2211527.
145 B. Zhong, X. Qin, H. Xu, L. Liu, L. Li, Z. Li, L. Cao, Z. Lou, J. Jackman, N. Cho and L. Wang, *Nat. Commun.*, 2024, **15**, 624.
146 Y. Zeng, Y. Wang, Q. Jin, Z. Pei, D. Luan, X. Zhang and X. Lou, *Angew. Chem., Int. Ed.*, 2021, **60**, 25793–25798.
147 L. Gou, S. Zhao, W. Wang, L. Xu, W. Wang, J. Wu, Z. Ma, X. Fan and D. Li, *ACS Appl. Energy Mater.*, 2021, **4**, 7355–7364.
148 L. Gou, J. Li, K. Liang, S. Zhao, D. Li and X. Fan, *Small*, 2023, **19**, 2208233.
149 G. Fang, C. Zhu, M. Chen, J. Zhou, B. Tang, X. Cao, X. Zheng, A. Pan and S. Liang, *Adv. Funct. Mater.*, 2019, **29**, 1808375.
150 Q. Chen, X. Lou, Y. Yuan, K. You, C. Li, C. Jiang, Y. Zeng, S. Zhou, J. Zhang, G. Hou, J. Lu and Y. Tang, *Adv. Mater.*, 2023, **35**, 2306294.
151 C. Chen, M. Shi, Y. Zhao, C. Yang, L. Zhao and C. Yan, *Chem. Eng. J.*, 2021, **422**, 130375.
152 R. Zhang, P. Liang, H. Yang, H. Min, M. Niu, S. Jin, Y. Jiang, Z. Pan, J. Yan, X. Shen and J. Wang, *Chem. Eng. J.*, 2022, **433**, 133687.
153 L. Liu, Y. Wu, L. Huang, K. Liu, B. Duployer, P. Rozier, P. Taberna and P. Simon, *Adv. Energy Mater.*, 2021, **11**, 2101287.
154 D. Wang, L. Wang, G. Liang, H. Li, Z. Liu, Z. Tang, J. Liang and C. Zhi, *ACS Nano*, 2019, **13**, 10643–10652.
155 J. Huang, Z. Wang, M. Hou, X. Dong, Y. Liu, Y. Wang and Y. Xia, *Nat. Commun.*, 2018, **9**, 2906.
156 A. Zhang, R. Zhao, Y. Wang, J. Yue, J. Yang, X. Wang, C. Wu and Y. Bai, *Angew. Chem., Int. Ed.*, 2023, **62**, e202313163.

157 K. Nam, S. Kim, E. Yang, Y. Jung, E. Levi, D. Aurbach and J. Choi, *Chem. Mater.*, 2015, **27**, 3721–3725.
158 Y. Li, X. Feng, S. Cui, Q. Shi, L. Mi and W. Chen, *CrystEngComm*, 2016, **18**, 3136–3141.
159 H. Yao, H. Yu, Y. Zheng, N. Li, S. Li, D. Luan, X. Lou and L. Yu, *Angew. Chem., Int. Ed.*, 2023, **62**, e202315257.
160 Y. Zhang, S. Deng, G. Pan, H. Zhang, B. Liu, X. Wang, X. Zheng, Q. Liu, X. Wang, X. Xia and J. Tu, *Small Methods*, 2020, **4**, 1900828.
161 H. Chen, W. Ma, J. Guo, J. Xiong, F. Hou, W. Si, Z. Sang and D. a. Yang, *J. Alloys Compd.*, 2023, **932**, 167688.
162 Y. Li, M. Chen, B. Liu, Y. Zhang, X. Liang and X. Xia, *Adv. Energy Mater.*, 2020, **10**, 2000927.
163 H. Qian, H. Ren, Y. Zhang, X. He, W. Li, J. Wang, J. Hu, H. Yang, H. Sari, Y. Chen and X. Li, *Electrochem. Energy Rev.*, 2022, **5**, 2.
164 D. Zhang, J. Cao, X. Zhang, N. Insin, S. Wang, J. Han, Y. Zhao, J. Qin and Y. Huang, *Adv. Funct. Mater.*, 2021, **31**, 2009412.
165 J. Ji, H. Wan, B. Zhang, C. Wang, Y. Gan, Q. Tan, N. Wang, J. Yao, Z. Zheng, P. Liang, J. Zhang, H. Wang, L. Tao, Y. Wang, D. Chao and H. Wang, *Adv. Energy Mater.*, 2021, **11**, 2003203.
166 G. Cui, Y. Zeng, J. Wu, Y. Guo, X. Gu and X. Lou, *Adv. Sci.*, 2022, **9**, 2106067.
167 Z. Liu, L. Qin, X. Chen, X. Xie, B. Zhu, Y. Gao, M. Zhou, G. Fang and S. Liang, *Mater. Today Energy*, 2021, **22**, 100851.
168 Y. Yang, T. Shao, Y. Zhang, Y. Lu, M. Li, H. Liu, Q. Xu and Y. Xia, *J. Power Sources*, 2023, **564**, 232863.
169 T. Shao, Y. Zhang, T. Cao, Y. Yang, Z. Li, H. Liu, Y. Wang and Y. Xia, *Chem. Eng. J.*, 2022, **431**, 133735.
170 N. Liu, X. Wu, Y. Yin, A. Chen, C. Zhao, Z. Guo, L. Fan and N. Zhang, *ACS Appl. Mater. Interfaces*, 2020, **12**, 28199–28205.
171 S. Lian, C. Sun, W. Xu, W. Huo, Y. Luo, K. Zhao, G. Yao, W. Xu, Y. Zhang, Z. Li, K. Yu, H. Zhao, H. Cheng, J. Zhang and L. Mai, *Nano Energy*, 2019, **62**, 79–84.
172 H. Wang, R. Guo, Y. Ma and F. Zhou, *Adv. Funct. Mater.*, 2023, **33**, 2301351.
173 H. Li, Z. Huang, B. Chen, Y. Jiang, C. Li, W. Xiao and X. Yan, *J. Power Sources*, 2022, **527**, 231198.
174 X. Cheng, J. Xiao, M. Ye, Y. Zhang, Y. Yang and C. Li, *ACS Appl. Mater. Interfaces*, 2022, **14**, 10489–10497.
175 Y. Zhang, Y. Liu, Z. Liu, X. Wu, Y. Wen, H. Chen, X. Ni, G. Liu, J. Huang and S. Peng, *J. Energy Chem.*, 2022, **64**, 23–32.
176 C. Huang, Q. Wang, D. Zhang and G. Shen, *Nano Res.*, 2022, **15**, 8118–8127.
177 Y. Zhao, P. Zhang, J. Liang, X. Xia, L. Ren, L. Song, W. Liu and X. Sun, *Energy Storage Mater.*, 2022, **47**, 424–433.
178 G. Nam, C. Hwang, H. Jang, N. Kane, Y. Ahn, M. Kwak, Z. Luo, T. Li, M. Kim, N. Liu and M. Liu, *Small*, 2023, 2306919.
179 Z. Li, C. Bommier, Z. Chong, Z. Jian, T. Surta, X. Wang, Z. Xing, J. Neuefeind, W. Stickle, M. Dolgos, P. Greaney and X. Ji, *Adv. Energy Mater.*, 2017, **7**, 1602894.
180 Y. Liu, K. Wang, X. Yang, J. Liu, X. Liu and X. Sun, *ACS Nano*, 2023, **17**, 14792–14799.
181 F. Ye, Q. Liu, C. Lu, F. Meng, T. Lin, H. Dong, L. Gu, Y. Wu, Z. Tang and L. Hu, *Energy Storage Mater.*, 2022, **52**, 675–684.
182 M. Mautner, *J. Am. Chem. Soc.*, 1988, **110**, 3854–3858.
183 A. Gandhe, J. Rebello, J. Figueiredo and J. Fernandes, *Appl. Catal., B*, 2007, **72**, 129–135.
184 X. Zeng, J. Liu, J. Mao, J. Hao, Z. Wang, S. Zhou, C. D. Ling and Z. Guo, *Adv. Energy Mater.*, 2020, **10**, 1904163.
185 Z. Zhong, J. Li, L. Li, X. Xi, Z. Luo, G. Fang, S. Liang and X. Wang, *Energy Storage Mater.*, 2022, **46**, 165–174.
186 Y. Liu, Z. Qin, X. Yang, J. Liu, X. Liu and X. Sun, *ACS Energy Lett.*, 2022, **7**, 1814–1819.
187 M. Mateos, N. Makivic, Y. Kim, B. Limoges and V. Balland, *Adv. Energy Mater.*, 2020, **10**, 2000332.
188 Y. Hu, Z. Liu, L. Li, S. Guo, X. Xie, Z. Luo, G. Fang and S. Liang, *Nat. Sci. Rev.*, 2023, **10**, nwad220.
189 M. Chuai, J. Yang, R. Tan, Z. Liu, Y. Yuan, Y. Xu, J. Sun, M. Wang, X. Zheng, N. Chen and W. Chen, *Adv. Mater.*, 2022, **34**, 2203249.
190 X. Shen, X. Wang, Y. Zhou, Y. Shi, L. Zhao, H. Jin, J. Di and Q. Li, *Adv. Funct. Mater.*, 2021, **31**, 2101579.
191 X. Xu, Y. Chen, W. Li, R. Yin, D. Zheng, X. Niu, X. Dai, W. Shi, W. Liu, F. Wu, M. Wu, S. Lu and X. Cao, *Small*, 2023, **19**, 2207517.
192 X. Zhao, L. Mao, Q. Cheng, F. Liao, G. Yang and L. Chen, *Carbon*, 2022, **186**, 160–170.
193 T. Li, R. Guo, L. Meng, X. Sun, Y. Li, F. Li, X. Zhao, L. An, J. Peng and W. Wang, *Chem. Eng. J.*, 2022, **446**, 137290.
194 Y. Xu, J. Zhu, J. Feng, Y. Wang, X. Wu, P. Ma, X. Zhang, G. Wang and X. Yan, *Energy Storage Mater.*, 2021, **38**, 299–308.
195 H. Peng, H. Fan, C. Yang, Y. Tian, C. Wang and J. Sui, *RSC Adv.*, 2020, **10**, 17702–17712.
196 K. Wang, J. Wang, P. Chen, M. Qin, C. Yang, W. Zhang, Z. Zhang, Y. Zhen, F. Fu and B. Xu, *Small*, 2023, **19**, 2300585.
197 Y. Ma, M. Xu, R. Liu, H. Xiao, Y. Liu, X. Wang, Y. Huang and G. Yuan, *Energy Storage Mater.*, 2022, **48**, 212–222.
198 Y. Chen, X. Hu, X. Chen, J. Liu, Y. Huang and D. Cao, *Chem. Eng. J.*, 2023, **478**, 147411.
199 Y. Yuan, K. He, B. W. Byles, C. Liu, K. Amine, J. Lu, E. Pomerantseva and R. Shahbazian-Yassar, *Chem*, 2019, **5**, 1793–1805.
200 S. Kim, D. Wu, N. Sadique, C. Quilty, L. Wu, A. Marschilok, K. Takeuchi, E. Takeuchi and Y. Zhu, *Small*, 2020, **16**, 2005406.
201 Q. Lin and L. Wang, *J. Semicond.*, 2023, **44**, 041601.
202 K. Du, Y. Liu, Y. Yang, F. Cui, J. Wang, M. Han, J. Su, J. Wang, X. Han and Y. Hu, *Adv. Mater.*, 2023, **35**, 2301538.
203 Y. Zhao, P. Zhang, J. Liang, X. Xia, L. Ren, L. Song, W. Liu and X. Sun, *Adv. Mater.*, 2022, **34**, 2204320.
204 S. Yang, H. Du, Y. Li, X. Wu, B. Xiao, Z. He, Q. Zhang and X. Wu, *Green Energy Environ.*, 2023, **8**, 1531–1552.
205 L. Cao, D. Li, E. Hu, J. Xu, T. Deng, L. Ma, Y. Wang, X. Yang and C. Wang, *J. Am. Chem. Soc.*, 2020, **142**, 21404–21409.

206 Y. Zhang, X. Li, L. Fan, Y. Shuai and N. Zhang, *Cell Rep. Phys. Sci.*, 2022, **3**, 100824.
207 S. Xu, W. Nie, P. Sun, J. Sun, Z. Xu, C. Chu and L. Liu, *Mater. Lett.*, 2023, **331**, 133546.
208 H. Wang, T. Wang, G. Stevenson, M. Chamoun and R. W. Lindström, *Energy Storage Mater.*, 2023, **63**, 103008.
209 P. Ruan, X. Xu, D. Zheng, X. Chen, X. Yin, S. Liang, X. Wu, W. Shi, X. Cao and J. Zhou, *ChemSusChem*, 2022, **15**, e202201118.
210 Y. Liu, Z. Qin, X. Yang, J. Liu, X. Liu and X. Sun, *Energy Storage Mater.*, 2023, **56**, 524–531.